UNIVERSITY OF QUEBEC AT CHICOUTIMI

A DISSERTATION PRESENTED TO THE UNIVERSITY OF

QUEBEC AT CHICOUTIMI IN PARTIAL FULFILLMENT

OF THE REQUIREMENT FOR THE DOCTOR

OF PHILOSOPHY IN ENGINEERING

BY

LANFENG JIN

DEVELOPMENT OF AL–SI CAST ALLOYS FOR ELEVATED-TEMPERATURE APPLICATIONS

MAY 2019

UNIVERSITÉ DU QUÉBEC À CHICOUTIMI

THESE PRÉSENTE À

L'UNIVERSITÉ DE QUÉBEC À CHICOUTIMI

COMME EXIGENCE PARTIELLE

DU DOCTORAT EN INGÉNIERIE

PAR

LANFENG JIN

DÉVELOPPEMENT D'ALLIAGES FONDERIE D'AL-SI

POUR LES APPLICATIONS ÀTEMPÉRATURE ÉLEVÉE

MAI 2019

Abstract

Aluminum Silicon (Al–Si) alloys are considered as the most important alloys among aluminum cast alloys and have been widely used in many industries, especially the aerospace and automotive industries. In order to further reduce the vehicle weight and therefore reduce the greenhouse gas emission, the growing demand for lighter and stronger Al–Si alloys for elevated-temperature applications has been one of many important scientific focuses in advances of conventional Al alloys. The general objective of the present study is to develop new Al–Si cast alloys that can be fabricated by conventional metallurgy route, through appropriate heat treatment to enhance their elevated-temperature (250 °C-350 °C) properties. This often necessitates the introduction of new alloy elements and subsequent optimization of alloy compositions. Hence, the influence of Mo and Mn elements on the microstructure and mechanical properties at both ambient and elevated temperatures in Al-6 wt.%Si-3.5 wt.% Cu 319 and Al-13 wt.% Si piston alloys were investigated in the present work.

For microstructure study, transmission electron microscope, scanning electron microscope and optical microscope equipped with an image analysis system were used. The mechanical properties at ambient temperature were evaluated by Vickers microhardness measurements and compression yield strength tests. The elevated-temperature mechanical properties and creep properties were assessed by compression yield strength tests and creep tests at 300^{o}C. The results obtained were divided into following three parts.

In the first part, the precipitation and preferential selection of Fe-rich intermetallics in Al–Si–Cu 319 cast alloys with two Fe contents (0.3 and 0.7 wt.%) and various Mo contents (0-0.4 wt.%) were investigated. The results showed that two types of platelet β-Fe (defined as eutectic β-Fe and pre-eutectic β-Fe) and α-Fe can

precipitate depending on the alloy compositions, such as the Fe and Mo contents. Generally, the addition of Mo promotes the formation of α-Fe instead of β-Fe. However, its effect on the phase competition between β-Fe and α-Fe is greatly related to the Fe content. In alloys with low Fe content (0.3 wt.%), an addition of 0.37 wt.% Mo can promote the complete precipitation of α-Fe and suppress the formation of eutectic β-Fe. However, in alloys with high Fe content (0.7 wt.%), only the pre-eutectic β-Fe amount decreases with increasing Mo addition, leaving the eutectic β-Fe almost unchanged. On the other hand, both pre-eutectic β-Fe and eutectic β-Fe can be fully suppressed with a combined addition of Mn (0.24 wt.%) and Mo (0.4 wt.%). Compared with Mn, Mo exhibits a stronger effect on the promotion of α-Fe. The combined addition of Mn and Mo can achieve better modifications of both pre-eutectic and eutectic β-Fe in 319 alloys with high Fe content.

In the second part, the effects of Mo and Mn additions on the evolution of dispersoids during various heat treatment conditions were investigated in 319 cast alloys. Furthermore, their effects on yield strength and creep resistance at elevated temperature (300 ^{o}C) were studied. The results showed that the additions of Mo or/and Mn can greatly improve the precipitation the dispersoids during heat treatment, while 500 ^{o}C /8h was found to be the optimal heat treatment condition characterized with the largest quantity and the smallest size of α-dispersoids. This was also confirmed by the improved yield strength at both room temperature and 300 ^{o}C. Meanwhile, the creep resistance at 300 ^{o}C was greatly improved due to the Mn and Mo additions, with doubled threshold stress (from 10.6 to 22.8 MPa) and 50 times lower minimum creep rate (from 5.5E-7 s^{-1} to 1.1E-8 s^{-1}). During the long-time exposure at 300 ^{o}C service temperature up to 1000 h, the decrease rate of elevated-temperature properties is much slower due to the presence of dispersoids from the Mn or/and Mo additions, which is 10% decrease in yield strength and 5% increase in the maximum creep strain in alloys with combined additions of Mn and Mo compared with 47% and 30% in base alloy free of Mn and Mo, respectively,

showing the superior thermal stability of Al–Si–Cu 319 alloys with Mn and Mo additions and then widening their applications at elevated temperature.

In the third part, the precipitation of dispersoids by Mo additions in a Mn-containing Al-13 wt.% Si piston alloy was studied by characterization of the dispersoid zone and dispersoid free zone during heat treatment using optical, scanning electron and transmission electron microscopes. The influence of the Mo addition and its dispersoids on the yield strength and creep resistance at 300 ^{o}C was investigated. The evolution of microstructure, yield strength and creep resistance during prolonged thermal exposure at 300 ^{o}C up to 1000 h were also studied. Results showed that compared with the individual Mn-containing base alloy, Mo can further enhance the precipitation of α-dispersoids by expanding dispersoid zone and restricting the dispersoid free zone after the precipitation treatment at 520 ^{o}C for 12 h, resulting in a remarkable improvement of yield strength at both room temperature and 300 ^{o}C as well as the creep resistance at 300 ^{o}C. The beneficial effect of the Mo addition on the improved yield strength and creep resistance is especially prominent during the long-term thermal exposure at 300 ^{o}C due to the presence of thermally stable dispersoids and the retardation of the fragmentation and spheroidization of Si particles.

Résumé

Les alliages aluminium-silicium (Al-Si) sont considérés comme les alliages les plus importants parmi les alliages d'aluminium moulés. A ce propos, ces alliages sont largement utilisés dans de nombreux secteurs, notamment les industries de l'aérospatiale et de l'automobile. A ce sujet, l'utilisation de cet alliage permet de réduire d'avantage le poids du véhicule, ce qui a la réduction des émissions de gaz à effet de serre. La demande croissante d'alliages Al-Si plus légers et plus résistants pour les applications à température élevée a été l'un des nombreux objectifs scientifiques importants dans les progrès des alliages d'aluminium conventionnels. L'objectif général de la présente étude est de développer de nouveaux alliages de fonderie Al-Si pouvant être fabriqués par la métallurgie conventionnelle tout en appliquant un traitement thermique approprié, afin d'améliorer leurs propriétés de température élevée (250 °C-350 °C). Cela nécessite souvent l'introduction de nouveaux éléments d'alliage et l'optimisation ultérieure des compositions d'alliage. Ainsi, l'influence des éléments Mo et Mn sur la microstructure et les propriétés mécaniques à la fois à température ambiante et à température élevée dans les alliages de piston à 319 et Al-13% Si ont été étudiés.

Pour l'étude de la microstructure, un microscope électronique à transmission, un microscope électronique à balayage et un microscope optique équipés d'un système d'analyse d'image ont été utilisés. Les propriétés mécaniques à la température ambiante ont été évaluées par des mesures de microdureté Vickers et des tests de résistance à la compression. Les propriétés mécaniques et les propriétés de fluage à température élevée ont été évaluées par des tests de résistance à la compression et des tests de fluage à température élevée. Les résultats obtenus ont été divisés en trois parties.

Dans la première partie, la précipitation et la sélection préférentielle des composés intermétalliques riches en Fe dans les alliages Al–Si–Cu 319 avec deux

teneurs en Fe (0,3 et 0,7% en poids) et diverses teneurs en Mo (0-0,4% en poids) ont été étudiées. Les résultats ont montré que deux types de plaquettes β-Fe (définis comme eutectiques β-Fe et pré-eutectiques β-Fe) et α-Fe peuvent précipiter en fonction des compositions d'alliage, telles que les teneurs en Fe et Mo. En général, l'ajout de Mo favorise la formation de α-Fe au lieu de β-Fe. Cependant, son effet sur la compétition de phase entre β-Fe et α-Fe est fortement lié à la teneur en Fe. Dans les alliages à faible teneur en Fe (0,3%), une addition de 0,37% de Mo peut favoriser la précipitation complète de l'α-Fe et supprimer la formation de β-Fe eutectique. Pourtant, dans les alliages à teneur élevée en Fe (0,7%), seule la quantité de β-Fe pré-eutectique diminue avec l'augmentation de l'ajout de Mo, laissant le β-Fe eutectique presque inchangé. La β-Fe pré-eutectique et la β-Fe eutectique peuvent être complètement supprimées avec une addition combinée de Mn (0,24%) et de Mo (0,4%). Comparé au Mn, le Mo exerce un effet plus marqué sur la précipitation de l'α-Fe. L'addition combinée de Mn et de Mo peut permettre d'avoir de meilleures modifications des β-Fe pré-eutectiques et eutectiques dans les alliages 319 à haute teneur en Fe.

Dans la deuxième partie, les effets d'alliages d'additions de Mo et de Mn sur l'évolution des dispersoïdes au cours de diverses conditions de traitement thermique ont été étudiés dans 319 alliages moulés. De plus, leurs effets sur la YS (limite d'élasticité) et la résistance au fluage à température élevée (300 °C) ont été étudiés. Les résultats ont montré que Mo et la combinaison de Mo et de Mn peuvent grandement améliorer la précipitation des dispersoïdes lors du traitement thermique. Le traitement thermique 500 ^{o}C/8h était la condition optimale caractérisée par la plus grande quantité et la plus petite taille de α-dispersoïdes. Cela était confirmée par la limite d'élasticité améliorée à la température ambiante et également pour la température de 300 °C. En parallèle, la résistance au fluage à 300 °C a été grandement améliorée grâce aux ajouts de Mn et de Mo, avec une contrainte de seuil doublée (de 10,6 à 22,8 MPa) et un taux de fluage minimum 50 fois plus bas (de 5,5 E-7 s^{-1} à

1,1 E-8 s^{-1}). Lors d'une exposition prolongée à une température de 300 °C jusqu'à 1 000 h, le taux de diminution des propriétés à température élevée est beaucoup plus lent en raison de la présence de dispersoïdes provenant des ajouts de Mn ou/et de Mo. A ce sujet, la présence de dispersoïdes a causé une diminution de 10% de la limite d'élasticité et une augmentation de 5% de la déformation maximale au fluage dans les alliages avec des ajouts combinés de Mn et Mo comparés à 47% et 30% dans un alliage de base dépourvu de Mn et de Mo respectivement. Cela montrait une stabilité thermique supérieure des alliages Al–Si–Cu 319 avec des additions de Mn et de Mo, puis en élargissant leurs applications à température élevée.

Dans la troisième partie, la précipitation de dispersoïdes par addition de Mo dans un alliage piston à 13% de Si contenant Mn a été étudiée par caractérisation de la zone dispersoïde et de la zone exempte de dispersoïde lors du traitement thermique à l'aide de microscopes optiques, à balayage et à transmission. L'influence de l'addition de Mo et de ses dispersoïdes sur la limite d'élasticité et la résistance au fluage à 300 °C a été étudiée. L'évolution de la microstructure, de la limite d'élasticité et de la résistance au fluage au cours d'une exposition thermique prolongée de 300 °C à 1000 h ont également été étudiés. Les résultats ont montré que, comparé à l'alliage basique ne contenant que du Mn, le Mo peut encore améliorer la précipitation des α-dispersoïdes en agrandissant la zone dispersoïde et en limitant la zone exempte de dispersoïde après le traitement par précipitation à 520 ^{o}C pendant 12 h, entraînant une amélioration remarquable du rendement de la résistance à la température ambiante et à 300 °C ainsi que la résistance au fluage à 300 °C. L'effet bénéfique de l'addition de Mo sur l'amélioration de la limite d'élasticité et de la résistance au fluage est particulièrement important pendant l'exposition thermique à long terme à 300 °C, en raison de la présence de dispersoïdes thermiquement stables et du retard de la fragmentation et de la sphéroïdisation des particules de Si.

Acknowledgements

First, I would like to express my sincere gratitude to my supervisor Prof. X.-Grant Chen for offering me the opportunity to conduct the PhD research, for his continuous support, his patience, motivation, immense knowledge, stimulating ideas and enlightening discussions. I am also thankful to my co-supervisor Prof. Kun Liu for his encouragement, whole-hearted support and his valuable suggestions during the research. This dissertation would not be possible without his assistance. Special thanks to Prof. Zhan Zhang for helping me conducting SEM and TEM observation. Besides, I would also like to thank Prof. Dilip Sarkar for the course studies.

Secondly, I would also like to thank all the staff of Applied Science Department of University of Quebec at Chicoutimi for their help and support. Special thanks go to Dany Racine for his technical assistance in DSC, image analysis and mechanical tests. I would also like to thank Samuel Dessureault, Dave Girard, Pier-Luc Privé, Émélie Brideau for all the availability in the laboratory. I am also grateful to Dr. Jian Qin, Dr. Lei Pan, Dr. Zhen Li, Dr. Emad Elgallad, Belkacem Amara, Xiaoming Qian, Zhixing Chen for the fruitful discussions. Many thanks to all my colleagues and friends in the department for their kind support, help, suggestions, and making my life much more delightful in Chicoutimi.

In addition, I would like to thank my beloved mother and brothers for the unconditional love and support throughout my PhD research.

Finally, this dissertation is dedicated to my late father who had been the whole world to me, a role model in my entire life, his legacy will be forever remembered and cherished.

Publications

Journal papers:

Lanfeng Jin, Kun Liu, X.-Grant Chen, Evolution of Fe-rich intermetallics in Al–Si–Cu 319 cast alloy with various Fe, Mo and Mn contents. Accepted by Metallurgical and Materials Transactions B.

Lanfeng Jin, Kun Liu, X.-Grant Chen, Evolution of dispersoids and their effect on elevated-temperature properties and creep resistance in Al–Si–Cu 319 cast alloys with Mo and Mn additions. Ready to submit in 2019.

Lanfeng Jin, Kun Liu, X.-Grant Chen, Improved elevated-temperature properties in Al–13%Si piston alloy by Mo addition. To be submitted in 2019.

Posters:

Lanfeng Jin, Kun Liu, X.-Grant Chen, Effect of Mo on the microstructure and microhardness of 319 foundry alloy. REGAL Students' Day, Chicoutimi, Canada, November. 2015 (Regal Prize).

Lanfeng Jin, Kun Liu, X.-Grant Chen, Formation of β-Al_5FeSi with various Fe, Mo addition in Al–Si–Cu–Mg foundry alloy. REGAL Students' Day, Quebec, Canada, October. 2016.

Lanfeng Jin, Kun Liu, X.-Grant Chen, Enhanced properties via Mo addition in Al–Si–Cu–Mg cast alloy. 2017 REGAL Students' Day, Montreal, Canada, September. 2017.

Lanfeng Jin, Kun Liu, X.-Grant Chen, Formation of dispersoids and their effect on creep property of Al–Si–Cu–Mg foundry alloy with additions of Mn and Mo. 2018 REGAL Students' Day, Montreal, Canada, June. 2018.

Table of Contents

List of Tables

List of figures

Chapter 1 Introduction

1.1 Background

Al–Si alloys have attracted increasing attentions for the combination of excellent castability and modest strength [1]. Besides, their good machinability makes them perfect candidates in various areas of manufacturing and technology fields especially in auto industry [1]. However, the growing demand for higher fuel efficiency and light weight structure components at elevated temperatures remains a big challenge for weight-sensitive automobile industries [2]. Some traditional Al-Si cast alloys can meet the requirement of room temperature applications by precipitation of various Cu and Mg containing precipitates [3]. Yet, due to the rapid coarsening of these nano-scale precipitates at elevated temperature (overageing effect), their applications at elevated temperature are greatly restricted [4]. In recent years, the dispersoid strengthening in AA3xxx alloys has been discovered and investigated [5-7], and the mechanical properties at both room and elevated temperature could be improved significantly [8, 9]. Moreover, dispersoids as the main strengthening phase have been proved to be thermally stable at elevated temperature [8]. Hence, introduction of dispersoids into Al-Si cast alloy to obtain the improved strength at both room and elevated temperature is highly feasible.

Mn can form thermally stable nano-scale α-Al(Fe, Mn)Si dispersoids and has been reported to be able to improve mechanical properties at elevated temperature [10]. More recently, Mo is also investigated to be able to precipitate α-Al(Fe, Mo)Si dispersoids and improved yield strength was achieved at both room and elevated temperature [10]. Besides, combined addition of Mo and Mn can also form large volume of thermally stable dispersoids, resulting in significant enhancement in strength [10-12].

However, open literatures about the effect of Mo and Mn, on the properties of Al–Si cast alloys, especially the creep resistance at elevated temperature are still limited. Besides, heat treatment parameters still need to be established in order to optimize the precipitation of dispersoids.

Therefore, in the present work, the influences of Mo and Mn on the microstructure and properties, especially at elevated temperature of Al-Si cast alloy will be systematically investigated.

1.2 Objectives

The main objective of this project is to explore the application of Al-Si cast alloy for elevated temperature applications (250-300 ^{o}C). To achieve the objective, the research will be performed in several parts listed as follows:

1. Study the solidification of Al-Si cast alloy and formation of different types of Fe-rich intermetallics. Investigate the effect of Mo or and Mn additions on the evolution of Fe-rich intermetallics.

2. Determine the optimal heat treatment parameters for maximizing dispersoid formation via studying a series of different heat treatment conditions.

3. Study the effect of α-dispersoids on the yield strength of Al–Si cast alloys at both ambient and elevated temperature.

4. Investigate the effect of dispersoids on creep resistance at 300 ^{o}C in Al-Si cast alloys.

5. Analyze the effect of dispersoids on thermal stability of Al-Si cast alloys by thermal exposure at 300 ^{o}C.

References

[1] F.C.R. Hernandez, J.M.H. Ramírez, R. Mackay, Al-Si Alloys: Automotive, Aeronautical, and Aerospace Applications, Springer International Publishing2017.

[2] M. Javidani, D. Larouche, Application of cast Al-Si alloys in internal combustion engine components, International Materials Reviews 59(3) (2014) 132-158.

[3] J.W. Martin, Precipitation hardening, Butterworth-Heinemann1998.

[4] C. Booth-Morrison, D.C. Dunand, D.N. Seidman, Coarsening resistance at 400 °C of precipitation-strengthened Al–Zr–Sc–Er alloys, Acta Materialia 59(18) (2011) 7029-7042.

[5] Y.J. Li, L. Arnberg, Quantitative study on the precipitation behavior of dispersoids in DC-cast AA3003 alloy during heating and homogenization, Acta Materialia 51(12) (2003) 3415-3428.

[6] L. Lodgaard, N. Ryum, Precipitation of dispersoids containing Mn and/or Cr in Al–Mg–Si alloys, Materials Science and Engineering: A 283(1–2) (2000) 144-152.

[7] Y.J. Li, A.M.F. Muggerud, A. Olsen, T. Furu, Precipitation of partially coherent α-Al(Mn,Fe)Si dispersoids and their strengthening effect in AA 3003 alloy, Acta Materialia 60(3) (2012) 1004-1014.

[8] K. Liu, X.G. Chen, Development of Al-Mn-Mg 3004 alloy for applications at elevated temperature via dispersoid strengthening, Materials & Design 84 (2015) 340-350.

[9] A.M.F. Muggerud, E.A. Mørtsell, Y. Li, R. Holmestad, Dispersoid strengthening in AA3xxx alloys with varying Mn and Si content during annealing at low temperatures, Materials Science and Engineering: A 567 (2013) 21-28.

[10] A.R. Farkoosh, X.G. Chen, M. Pekguleryuz, Dispersoid strengthening of a high temperature Al-Si-Cu-Mg alloy via Mo addition, Materials Science and Engineering: A 620 (2015) 181-189.

[11] A.R. Farkoosh, M. Pekguleryuz, Enhanced mechanical properties of an

Al-Si-Cu-Mg alloy at 300°C: Effects of Mg and the Q-precipitate phase, Materials Science and Engineering: A 621 (2015) 277-286.

[12] A.R. Farkoosh, X. Grant Chen, M. Pekguleryuz, Interaction between molybdenum and manganese to form effective dispersoids in an Al-Si-Cu-Mg alloy and their influence on creep resistance, Materials Science and Engineering: A 627 (2015) 127-138.

Chapter 2 Literature Review

2.1 Introduction of Al-Si alloys

In 21th Century the auto industry has paid increasing attention to the elevated-temperature applications of materials [1]. The relatively high service temperature requires engineering materials to possess high strength, high modulus of elasticity, abrasion resistance, corrosion resistance etc. Ideally, the material should also have a low density to increase fuel efficiency. Besides, low thermal expansion, and high thermal conductivity are also desirable for elevated-temperature application materials. In addition, good machinability and castability are also important factors in selecting the proper material, as the harder it is to machine the product, the higher the costs of manufacturing. Last but not the least, the alloys must possess good vibration damping to absorb the shuddering of the moving parts.

Among numerous engineering materials to meet above mentioned requirements, Al-Si alloys have been widely used in the automotive industry as a suitable alternative of cast iron in fabrication of engine components. Commonly used Al-Si cast alloys contain Si between 5-25 wt.% [1]. The Al-Si alloys generally have good castability due to its relatively high Si concentration, which increases alloy fluidity, making these alloys ideal for casting components with complex geometries without considerably raising the cost. Besides their high strength to weight ratio, their excellent thermal conductivity also allows the combustion heat to be extracted more rapidly and efficiently [1, 2]. In addition, by alloying other elements, such as Cu and Mg, Al-Si alloys can be further strengthened by forming a variety of precipitates.

Al-Si alloys are usually applied artificial ageing after solution treatment to obtain the optimum properties, and they are generally gravity casted to fabricate engine blocks. Fig. 2.1 shows the common applications of Al-Si alloys as engine block and

cylinder head. They are two major components of an engine and had been historically fabricated from cast iron. Nowadays, most of the engine blocks and cylinder heads are manufactured by Al–Si alloys, leading to significant weight reduction of 100 Kg to 200 Kg, consequently, reduce carbon dioxide emission and significant improved fuel economy [1].

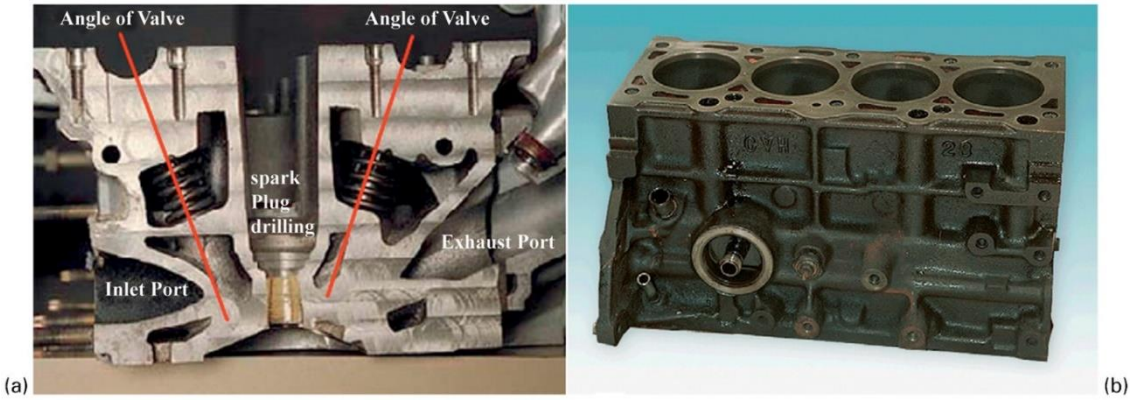

Fig. 2.1 (a) Cross-section of a cylinder head and (b) engine block [2].

2.2 Microstructure of Al-Si cast alloys

Despite the wide varieties of Al-Si cast alloys, they can generally be divided into three types based on their Si content, namely hypoeutectic, eutectic and hypereutectic alloys [1]. This section will mainly deal with the microstructure of hypoeutectic Al-Si cast alloys, especially various intermetallics in the alloys.

The typical microstructure of three type of Al–Si alloys are shown in Fig. 2.2. Hypereutectic Al-Si alloys usually contain coarse, angular primary Si particles as well as a eutectic Si phase; whereas, hypoeutectic alloys consist of a soft and ductile primary Al phase and a hard but brittle eutectic Si phase, which is usually lamellar in morphology. The different morphology of Si particles could be ascribed to the low interfacial energy between Al and Si and the strong growth anisotropy of Si [3]. The coarse lamellar Si particles may act as stress concentration sites and crack propagation

paths [4-7]. However, the deleterious effect can be alleviated by modifying them into fine and fibrous Si particles through higher solidification rates [8, 9], solution heat treatment [10-12] or alloying with certain elements [13-18].

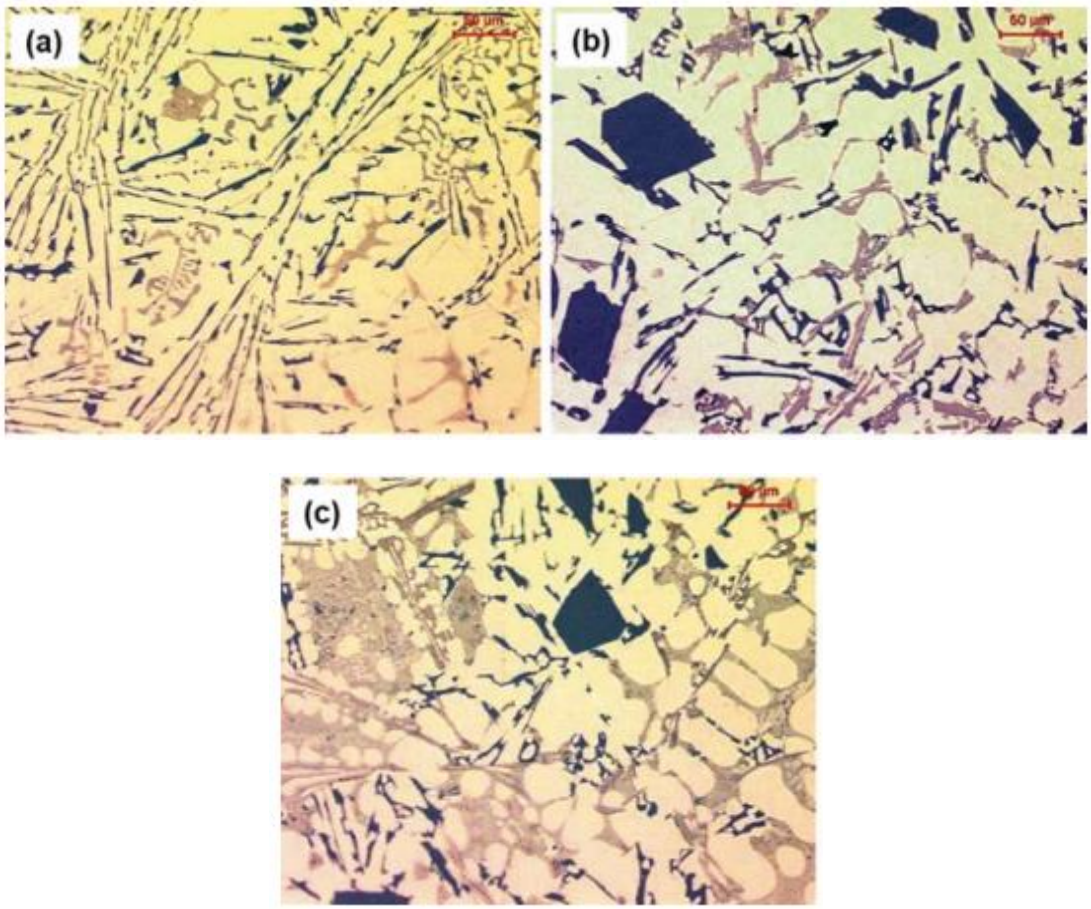

Fig. 2.2 Optical microscopy of Al–Si alloys for (a) Al–Si hypoeutectic/ eutectic, (b) Al–Si hypereutectic, (c) Al–Si hypereutectic showing the dendritic structure [19].

2.2.1 Main intermetallics in Al-Si alloys

Due to the different alloy compositions, such as Si, Cu and Mg, various intermetallics can form in Al-Si alloys. The formation of intermetallics in Al-Si 319 cast alloy is discussed in this part since they are used in present work and its typical microstructure is shown in Fig. 2.3. It is composed of primary Al dendrites, Al–Si eutectic and multiple intermetallics. Since Cu is almost always added in Al–Si 319

alloys, eutectic and blocky Al_2Cu also appear in the microstructure. Mg bearing phases, such as Mg_2Si and $Al_5Mg_8Cu_2Si_6$ may present depending on the Mg concentration in Al–Si alloys. Besides, the presence of Fe in Al–Si alloys will inevitably precipitate Fe bearing intermetallics such as β-Al_5FeSi and/or α-$Al_{15}(Mn, Fe)_3Si_2$.

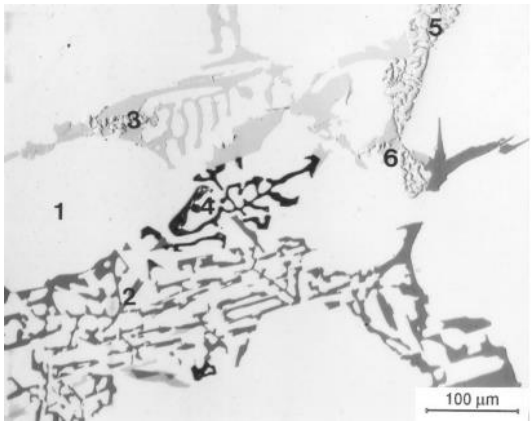

Fig. 2.3 Microstructure of as-solidified Al–319 alloy(A319.2+1.2 wt.% Mg) showing (1) α-Al dendrite, (2) eutectic Si, (3)$Al_8Mg_3Si_6Fe$, (4) Mg_2Si, (5) Al_2Cu, (6)$Al_5Mg_8Cu_2Si_6$ [19].

It should also be noted that the eutectic Si could form Si network for eutectic Al-Si alloys [20] and makes it the most striking characteristics for eutectic Al-Si alloys. Nevertheless, these intermetallics precipitate at different stages during solidification. And the complexity of precipitation sequences will largely depend on the alloy composition: the more elements contained in the alloy, the more complicated the precipitation sequence will be.

Fig. 2.4 shows the cooling curve and its first derivative obtained from the A319 alloy while Table 2.1 presents its typical solidification sequence. As listed in Table 2.1, when the Al–Si alloy solidifies, the primary aluminum forms and grows in dendrites (hypoeutectic) or silicon phase forms and grows in angular primary particles (hypereutectic). When the eutectic point is reached, the eutectic Al–Si phases nucleate

and grow until the end of solidification. The formation temperature of α-Al dendrite, eutectic Si and eutectic Al_2Cu are relatively fixed and independent with alloy composition. For various other intermetallics in alloys with complex compositions, whether these phases form and their corresponding formation temperatures are dependent on many parameters such as alloy composition, cooling rate during solidification [21].

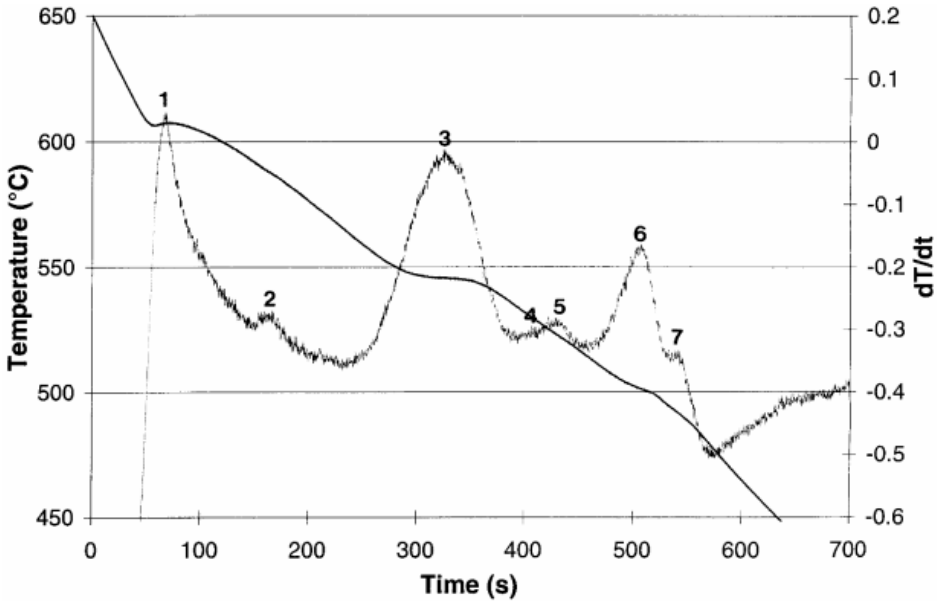

Fig. 2.4 Temperature-time cooling curve and its first derivative obtained from A319.2 alloy＋0.6 wt. % Mg [21].

Table 2.1 List of reactions during solidification of A319 Al alloy containing 0.08 wt.% Mg [21].

Reaction No.	Temperature	Reaction
1	611.8	Formation of α-Al dendrite
2	600-572.7	precipitation of pre-eutectic Fe phases
3	561.8	precipitation of eutectic Si phase
4	550-541	precipitation of post eutectic β-Al_5FeSi
5	510	precipitation of Mg_2Si
6	510	precipitation of Al_2Cu
7	502.7	precipitation of $Al_5Mg_8Cu_2Si_6$

Among all the intermetallics in Al-Si alloys, Al_2Cu is probably one of the most important to potentially strengthen the alloys after proper heat treatment. However, the melting point for eutectic Al_2Cu is relatively lower in Al–Si alloy (~510^{o}C), thus it is very important to take it into account when selecting optimal solution heat treatment temperature without causing incipient melting. There are two types of Al_2Cu intermetallics, namely fine eutectic Al_2Cu and blocky Al_2Cu. The presence of nucleation sites or high cooling rates during solidification can result in fine Al_2Cu particles, which can dissolve within 8 hrs of solid solution at 490°C [22]. Whereas, the blocky Al_2Cu phases are difficult to dissolve during solid solution heat treatment [23].

In Al–Si cast alloy containing Mg, large amount of Mg_2Si intermetallics can be precipitated during solidification. In addition, formation of Q-$Al_5Cu_2Mg_8Si_6$ phase in

Al–Si–Cu–Mg alloys with high content of Mg is also reported in reference [24]. With the presence of Fe and Si, it can form π-$Al_8Mg_3FeSi_6$ phase through L + β-Al_5FeSi→Al + Si + $Al_8Mg_3FeSi_6$ [25]. The morphologies of Mg_2Si, π-$Al_8Mg_3Si_6Fe$ and Q-$Al_5Cu_2Mg_8Si_6$ are also shown in Fig. 2.3.

2.2.2 Fe-rich intermetallics

Fe is the most common impurity in Al–Si cast alloys. Common sources of Fe in cast alloys are from (i) casting processes, (ii) primary metal and master alloys, (iii) iron tools and equipment used during melting, transferring and casting, and (iv) recycled materials melting equipment and from re-melted scrap castings [26]. Fe level is usually restricted to below 0.15 wt.% in commercial Al–Si cast alloys [27]. However, if Fe presents in the alloy, many different Fe intermetallics can precipitated in the alloys. This section deals with the Fe intermetallics and the modification of β-Al_5FeSi intermetallics.

Fe-rich intermetallics

The solubility of Fe is approximately 1.8 wt. % at 655°C in liquid pure Al but only 0.0052 wt. % at 450°C in solid pure Al [28]. Therefore, almost all Fe element precipitate from liquid Al in the form of various Fe-rich intermetallics during solidification. Many Fe-rich intermetallics have been reported for different Al alloys, e.g., Al_3Fe, Al_6Fe, Al_mFe, and Al_7Cu_2Fe [29-34]. In Al-Si cast alloys, α-AlSiFe, β-Al_5FeSi, and π-$Al_8FeMg_3Si_6$ (with the presence of Mg in the alloy) are the most commonly reported Fe intermetallics [2]. With the presence of Mn and Cr, the α-AlSiFe phases can also appear as $Al_{15}(Mn,Fe)_3Si_2$ or $Al_{15}(Mn,Cr,Fe)_3Si_2$ [27]. In addition to their different constituents between α-AlSiFe and β-Al_5FeSi, their morphologies also have their unique characteristics: α-AlSiFe appears in the form of Chinese script under microscopy, as is seen in Fig.2.5(a). Whereas, β-Al_5FeSi has platelet morphology (in three dimensions) and appears as a needle in micrograph [35], as is seen in Fig.2.5(b).

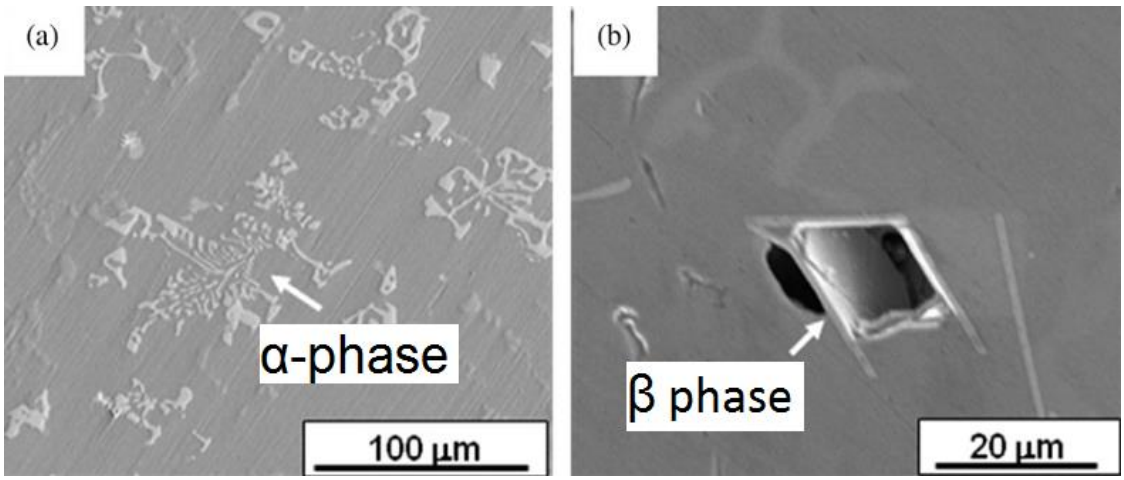

Fig.2.5 Microstructures of the two different types of Fe intermetallic phases in the Type 319 aluminum alloy: (a) Chinese script α-phase and (b) needle β-Al_5FeSi phase [36].

According to Table 2.1, the Fe- and Mn- containing phases, e.g., the α-$Al_{15}Mn_3Si_2$ and β-Al_5FeSi intermetallics precipitate during different stages of solidification. α-$Al_{15}Mn_3Si_2$ intermetallics normally precipitate after the formation of initial α-Al dendrites but before the appearance of the Al–Si eutectic. If high Fe and Mn levels are present in the alloy and the cooling rate is low, the α-$Al_{15}(Mn,Fe)_3Si_2$ phase will precipitate as a primary phase, in the form of coarse particles termed "sludge," having polygonal or star-like morphologies [37]. On the other hand, the β-Al_5FeSi phase usually precipitates as a co-eutectic phase before the precipitation of Al_2Cu and other more complex phases [35].

The effect of Fe on mechanical properties has been one of many hot research fields in Al metallurgy. At present, it is generally agreed that Fe increases hardness and greatly reduces the fracture toughness, ductility, fatigue resistance and impact energy [26]. According to Bonsack [38], any amount of Fe over 0.5 wt.% will be present as Al–Fe silicide in large needles, which increases strength and hardness but slightly reduces ductility. Above 0.8 wt.% Fe, both strength and elongation deteriorate rapidly. In addition, excessive Fe content also imposes deleterious influence on the

machinability. However, Fe up to 1.3 wt.% is reported to be beneficial to die cast parts in terms of improved strength, hardness and low tendency toward hot cracking [39]. Courture *et al.* [40] stated that the addition of Fe to Al–Si alloys is detrimental to the mechanical properties due to the formation of the brittle β-Al_5FeSi intermetallics, which are very hard, brittle and have relatively low bond strength with the matrix. The β-Al_5FeSi of platelet morphology can block metal feeding and consequently generate many porosities during solidification [41], therefore make alloys more easily fractured under tensile loads [2, 42, 43], leading to the decreased ductility and strength [44]. Generally, the detrimental effect of β-Al_5FeSi is largely correlated with the morphology, size and volume fraction. Hence, the necessity to modify the morphology and limit its diameter is vital for industrial practice of Al-Si alloys.

Modification of β-Al_5FeSi

The detrimental effect of Fe can be minimized by various techniques: (1) rapid solidification silicon [45, 46], (2) Chemical modification [47], and (3) melt superheating [2]. All above-mentioned methods basically convert the crystallization of the needle-like β-Al_5FeSi to the less deleterious Chinese script α-Fe phases [2]. Though each of these approaches has its own advantages and limitations, chemical modification, especially via additions of alloying elements, such as Mn, remains the most common practice in Al metallurgy. Elsebaie *et al.* [48] reported that the addition of Mn can improves the impact energy values appreciably and decrease in the impact energy values. The addition of specific controlled amounts of Mn can decrease the detrimental effects of β-Al_5FeSi platelets through the favourable precipitation of Fe in the form of the more compact Chinese script α-$Al_{15}(Mn,Fe)_3Si_2$ phases. But the amount of Mn to eliminate the detrimental effect of β-Fe phase is still under debate. Reference [49] reported that an Mn/Fe ratio of 0.5 seems to be sufficient for substitution of β-Al_5FeSi by a-$Al_{15}(Mn,Fe)_3Si_2$ phases, but other researchers [50] stated that some β-phases could remain even at higher Mn/Fe ration than 0.5. Recently, Farkoosh *et al.* [51] stated that Mo can suppress the formation of the brittle β-Al_5FeSi

intermetallic phase, which results in higher mechanical properties. Albeit, open literatures about the modification effect of Mo on β-Al_5FeSi are still quite limited.

2.3 Strengthening mechanisms at elevated temperature

Like the strengthening effect at room temperature, solid solution strengthening, precipitation strengthening and dispersoid strengthening are three of most applied strengthening effects at elevated temperature. This section deals with the mechanisms of three strengthening methods and their applications in Al-Si alloys.

2.3.1 Solid solution strengthening

Solid solution strengthening is an increase in strength by means of solute alloying elements in the matrix. By alloying elements into the Al matrix, depending on their size of the alloying elements, they can form either substitution or interstitial solid solution, as illustrated in Fig. 2.6. In both cases, the overall crystal structure is essentially unchanged. However, these alloying elements in the solution create lattice distortion. The greater the difference in lattice parameter, the higher the local stress fields introduced by alloying. These local stress fields act as a barrier to dislocation movement; hence the solid solution strengthening can be achieved.

The strengthening contribution of the solid solution from solute elements could be calculated according to the equation below:

$$\sigma_{ss} = HC^{\alpha} \qquad \text{Eq. 2.1}$$

Where C is the concentration of solute atoms, H and α are constant.

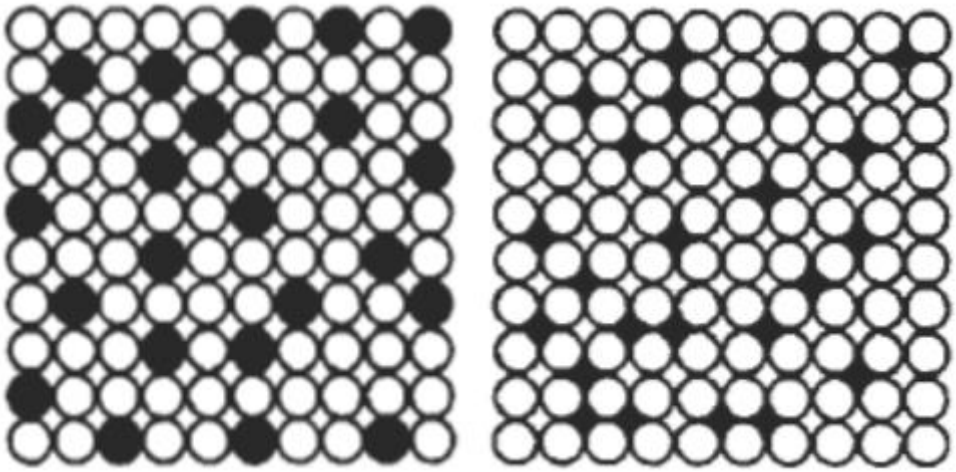

Fig. 2.6 Schematic models of solid solutions: substitutional solid solution and interstitial solid solution [52].

The strengthening degree is generally proportionally to solute concentration. However, the amount of alloying elements is strictly restricted by the phase diagram so as not to precipitate a new phase [53]. It should also be noted that although nearly every element can solute into Al alloy, only a small fraction of them can exert substantial strengthening effect. In Al alloys, Cu and Mg are the two prominent solutes for solid solution strengthening. Cu and Mg in solid solution of Al–Si–Cu–Mg alloys increase yield strength and ultimate tensile strength. However, the elongation of alloys drops with the addition of Cu and Mg [54].

2.3.2 Precipitation strengthening

The precipitation strengthening is another important hardening mechanism in Al-Si alloys. The precipitation strengthening is achieved by precipitation of fine and large quantity of precipitates, thus hindering the motion of dislocation. For heat treatable Al-Si alloys, the precipitation heat treatment usually involves three consecutive stages: solution treatment, quenching and ageing, as shown in Fig. 2.7. The purpose of solution heat treatment in Al–Si alloy is to: (a) Dissolve Cu and Mg containing intermetallic phases formed during solidification; (b) Homogenize the

alloying elements; (c) Spheroidize eutectic Si particles [23].

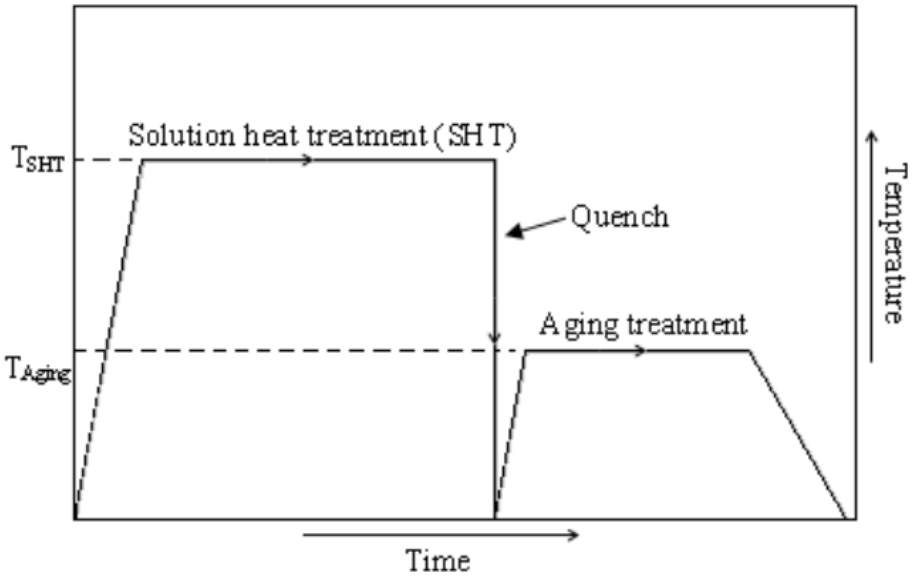

Fig. 2.7 Diagram showing the three steps for precipitation hardening [55].

The strengthening effect is closely related with the ability to hinder the motion of dislocations [56]. In precipitation strengthening, it is strongly dependent on the size and distribution of small precipitates. The strength of the precipitates increases with their size as long as they are sheared by dislocations. Further increase of precipitate size makes the shearing processes rather difficult; thus, it is more favourable for the dislocations to pass the precipitates via the Orowan mechanism. As indicated in Fig. 2.8 and Fig. 2.9, small precipitates are normally sheared by moving dislocations (Fig. 2.8). When the precipitates are larger, the moving of dislocation is harder through bypassing the precipitates than by bowing (Orowan mechanism) [23].

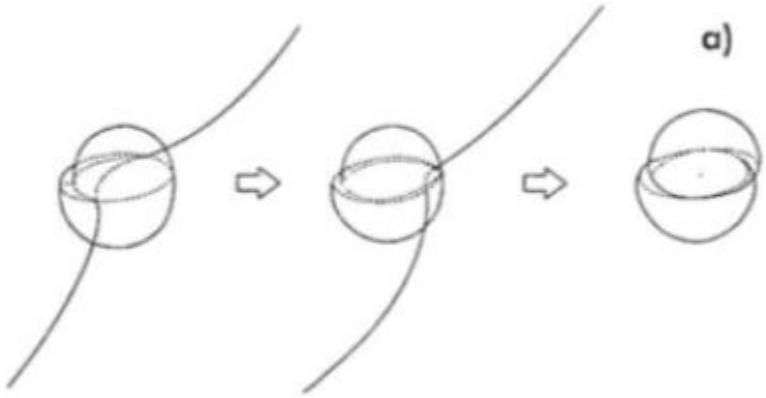

Fig. 2.8 Dislocations passing a precipitate by a) shearing and b) looping [57].

The relationship between the applied stress and the dislocation bowing is illustrated in Fig. 2.9, and summed up with the Orowan equation [58]:

$$\Delta\tau_y = {Gb}/{L} \qquad \text{Eq. 2.2}$$

where $\Delta\tau_y$ is the increase in yield stress due to the particles, G is the shear modulus of the matrix, b is the Burgers vector of the dislocation, and L is the particle spacing, which is usually considered to be the distance between particles arranged on a square grid in the slip plane.

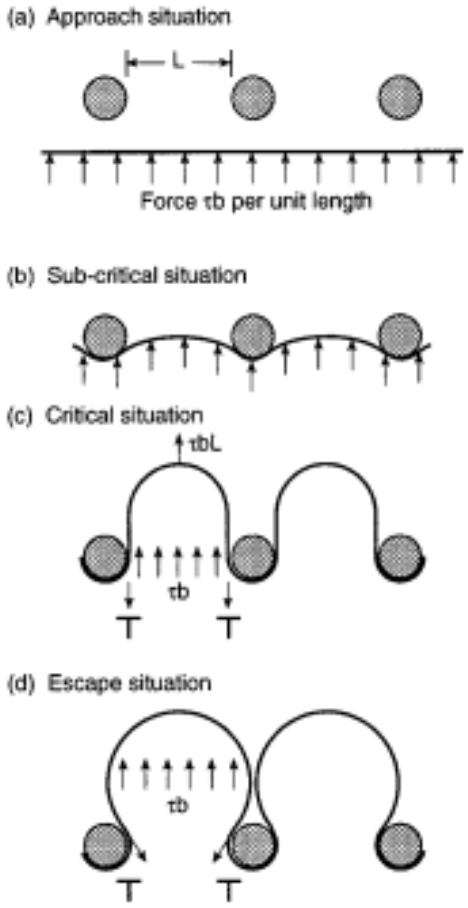

Fig. 2.9 Dislocation meets undeformable second phase particles: dislocation release at higher stresses may occur by Orowan looping or by cross-slip [58].

Ashby further developed this equation to consider the inter-particle spacing, and the effects of statistically distributed particles. The Ashby–Orowan relationship [59, 60] is given as:

$$\Delta\tau_y = 0.84\left({}^{1.2Gb}/_{2\pi L}\right)\ln({}^{X}/_{2b}) \qquad \text{Eq. 2.3}$$

Application of the Taylor factor for polycrystalline materials, expressing the microstructural parameters in terms of the volume fraction and real diameter and converting shear stress to tensile stress, yields:

$$\Delta\sigma_y = ({}^{0.538Gbf^{1/2}}/_{X})\ln({}^{X}/_{2b}) \qquad \text{Eq. 2.4}$$

where $\Delta\sigma_y$ y is the increase in yield strength, G is the shear modulus, b is the Burgers vector, f is the volume fraction of particles, and X is the real (spatial) diameter of the particles.

Kinetics of precipitates

Usually, the decomposition of precipitates or dispersoids from matrix may be divided into three stages: (i) the formation of nuclei; (ii) the growth of these nuclei.

Stage (i) may occur in one of two ways: homogeneous nucleation through spinodal decomposition, in which small concentration fluctuations lead to a decrease in free energy, the reaction may proceed spontaneously and there is no barrier to nucleation; heterogeneous nucleation in regions of high free energy per atom such as point defects, dislocations, grain boundaries.

J. Robertson *et al.* [61] presented a kinetic model for Al_3Zr dispersoids based on several assumptions as follows [62]: Al_3Zr is the only precipitate; Nucleation occurs homogeneously within the matrix; growth of Al_3Zr particles is controlled by diffusion of Zr to the particle/matrix interface.

The classical steady state nucleation equation has been used to describe the nucleation rate. The nucleation rate is then given by:

$$J = N_0 \frac{KT}{h} \exp\left(-\frac{G^* + Q}{kT}\right) \qquad \text{Eq. 2.5}$$

where J is the nucleation rate per unit volume. N_0 is the number density of nucleation sites which for homogeneous nucleation is equal to the number of Zr atoms per unit volume. G^* is the activation energy barrier for formation of a critically sized cluster. Q is the activation energy for diffusion of zirconium in aluminium. K and h are the Boltzmann and Planck constants respectively. T is the thermodynamic temperature. G^* is related to the critical radius and the interfacial energy, σ, according to:

$$G = \frac{4}{3}\pi r^{*2}\sigma \qquad \text{Eq.2.6}$$

The critical radius size r^* is calculated using the Gibbs Thomson equation and approach which is valid for dilute solutions. The critical radius corresponds to a special case of the equation, since when $r = r^*$, the solute concentration at the interface is the same as the mean concentration of the matrix and there is no concentration gradient at the interface, $r^*$is thus given by

$$r^* = \frac{2\sigma V_a}{KT \ln\frac{c}{c_\infty^\alpha}} \qquad \text{Eq. 2.7}$$

Where V_a is the atomic volume, c is the instantaneous concentration of zirconium in the matrix and c_∞^α is the concentration of Zr in the matrix in equilibrium with Al_3Zr assuming a planar interface. Values of c_∞^α can be obtained from the solvus line calculated for the metastable Al_3Zr phase in the binary Al–Zr system.

For spherical particles, the growth rate is given by:

$$\frac{dr}{dt} = \frac{D}{r}\frac{c - c_r^\alpha}{c^{\alpha'} - c_\infty^{\alpha'}} \qquad \text{Eq.2.8}$$

Where D is the diffusion coefficient, r the particle radius, c_r^α is the concentration of Zr in the matrix at the interface and $c^{\alpha'}$ the concentration of zirconium in the particles. $c^{\alpha'}$ is calculated from $c_\infty^{\alpha'}$ using the Gibbs–Thompson equation, which for the general case may be expressed as

$$C_r^\alpha = C_\infty^\alpha \exp\left(\frac{2\sigma V_a}{kT}\frac{1}{r}\right) \qquad \text{Eq.2.9}$$

The diffusion coefficient of zirconium in aluminum was calculated at a given temperature from:

$$D = D_0 \exp \frac{-Q}{RT} \quad \text{Eq. 2.10}$$

Where R is the gas constant. The values for D_0 and Q used were 0.0728 m^2s^{-1} and 242 KJ mol^{-1}, respectively.

Precipitates in Al-Si cast alloys

Due to the complexity of elements in Al-Si alloy, different precipitates can form, and the section describes several common precipitates in Al-Si cast alloys, and their strengthening effect of Al-Si alloys.

Mg_2Si precipitates

Mg_2Si precipitate is one of the very common precipitates in Al-Si alloys if Mg is also present in the alloy. The supersaturated solid solution decomposes to form the metastable precipitates designated GP zone, β", β' until equilibrium β. The precipitation sequence is generally described as follows [63], solute clusters → GP zones (spherical)→β"(needle)→β'(rod)→β. The typical size of needle β" is around 4 * 4 *50 nm^3 [64]. Further overageing transforms the needle β" into thick rods β'. The β' phase forms as rods of approximately 10 * 10 *500 nm^3 [65]. The β equilibrium phase is found to be plates with dimensions of several micrometers with composition Mg_2Si [66].

The typical TEM micrograph of β" and β' precipitates and their corresponding Selected area diffraction pattern (SADP) are shown in Fig. 2.10 and Fig. 2.11 respectively [67]. As is seen, they are coherent or semicoherent with Al matrix, thus the strenghening effect can be obtained. In Al-Si alloys with Cu, Mg additions, the optimal strength is often achieved through strengthening of various types of precipitates. Ouellet *et al.* [68] reported a hardening peak caused by the cooperative precipitation of Al_2Cu and Mg_2Si phases in Al–Si–Cu–Mg alloys. It has been found that the type of precipitation in the Al–Cu–Mg–Si alloys depends on Mg contents as well as on the Cu:Mg ratio in solid solution. For a Cu:Mg ratio of 2.0 (at. %),

preferential precipitation of Mg_2Si occurs, while a ratio close to 8.0, promotes the formation of the Al_2Cu compound [69]. The increase of Mg content in solid solution contributes to the precipitation phenomenon since clusters of magnesium are the precursors in the formation of Mg_2Si in Al–Mg–Si alloys [70].

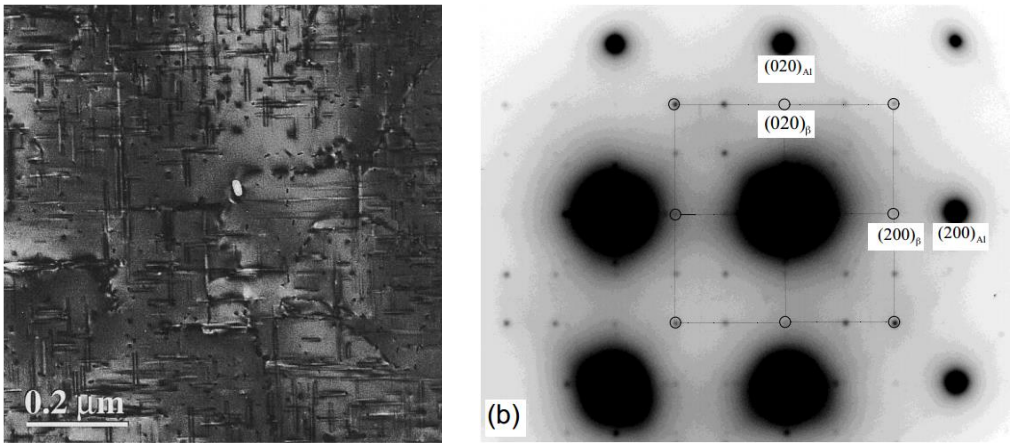

Fig. 2.10 Typical β''precipitates and its corresponding SADP [67].

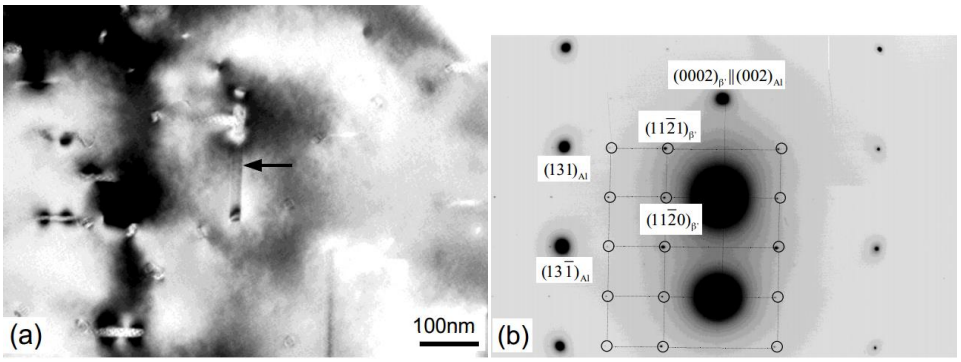

Fig. 2.11 Typical β'precipitates and its corresponding SADP [67].

Besides, metastable Mg_2Si precipitates have positive effect on the nucleation of dispersoids. It was reported that α-Al(Mn,Cr,Fe)-Si dispersoids heterogeneously nuclear on β'-Mg_2Si in 6xxx alloys [71]. As shown in Fig. 2.12, an intermediate phase u-phase nucleated on the β'-Mg_2Si. With continued annealing, α-Al(Mn,Cr,Fe)-Si dispersoids nucleated heterogeneously on the ‘u-phase’ precipitates before these precipitates dissolved [24, 71, 72].

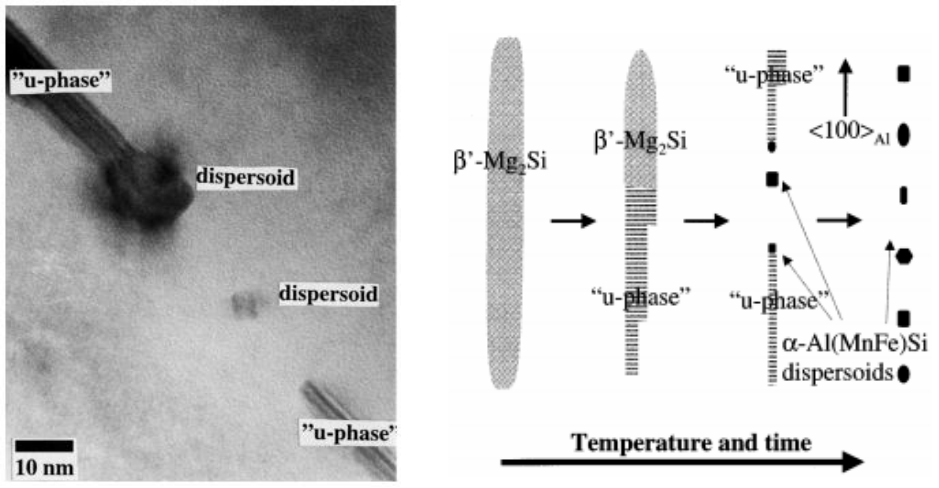

(a) (b)

Fig. 2.12 (a) TEM image of dispersoid nucleated on the surface of u-phase (b) a model of the precipitation of the dispersoids [71].

Al_2Cu precipitates

Cu is one of the most common alloying elements to improve mechanical properties in Al-Si alloys. Cu addition improves strength and hardness of Al–Si alloys in both as-cast and heat-treated conditions [73]. Al-Si alloys containing 4 to 6 wt.% Cu respond most strongly to heat treatment and can reach high strength and ductility [54]. The strengthening effect comes from the decomposition of supersaturated Cu solid solution to form various metastable precipitates. The Al_2Cu precipitation sequence is generally described as follows [63], $\alpha_{ss} \rightarrow GPZones \rightarrow \theta'' \rightarrow \theta' \rightarrow \theta\left(Al_2Cu\right)$ and their unit cells are shown in Fig. 2.13.

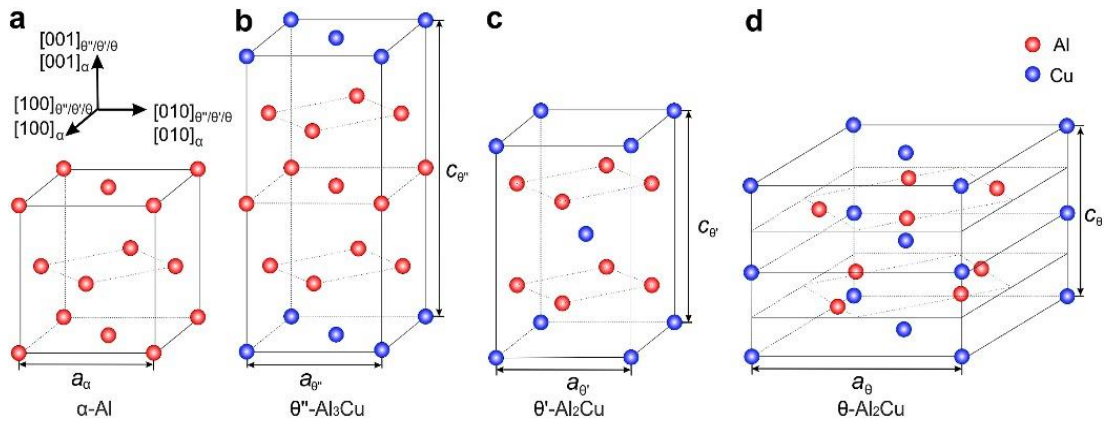

Fig. 2.13 Unit cells of α–Al matrix and θ'', θ' and θ intermetallic phases [74].

The precipitation sequence starts with the decomposition of the supersaturate solid solution and the clustering of Cu atoms; the clustering then leads to formation of coherent, disk-shaped GP zones. These zones manifest as two-dimensional Cu-rich disks with diameters of approximately 3-5 nm. With prolonged time, the GP zones increase in number while remain relatively constant in size. If the ageing temperature increase, the GP zones dissolve and are replaced by metastable precipitates θ". This precipitate is a three-dimensional disk-shaped plate having an ordered tetragonal arrangement of Al and Cu atoms; θ" also appears to nucleate uniformly in the matrix and is coherent with matrix. As ageing proceeds, the θ" starts to dissolve, and θ' commences to form by nucleating on heterogeneously on dislocations or other defects [75] (Fig. 2.14b). θ' also has a plate-like shape and is composed of Al and Cu atoms in an ordered tetragonal structure [23, 57]. However, θ' precipitates grow on further ageing by diffusion of atoms from the supersaturated solid solution to the precipitates [76]. The precipitates continue to grow in accordance with Ostwald ripening [77]. The larger precipitates coarsen as the smaller ones dissolve. As the precipitates grow, the coherency strain increases until interfacial bond strength is exceeded, and the precipitates become non-coherent. So last to form is the non-coherent equilibrium phases (θ), which is completely incoherent with the matrix. In fact, combined with its relatively large size and coarse distribution, the formation of θ reduces the strength

significantly [57]. It should be noted that the best strengthening is obtained when θ" is the main strengthening phase [57].

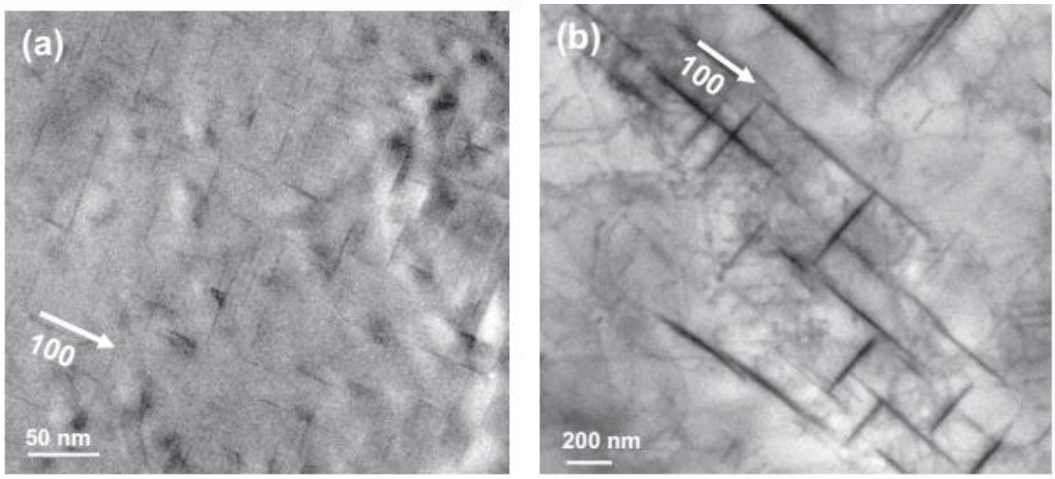

Fig. 2.14 (a) Bright-field transmission electron microscope micrograph depicting GPII in the ＜100＞Al zone obtained after aging at 438 K for 8 h; (b) the θ' precipitates in the＜100＞Al zone observed after aging at 463 K for 8 h [75].

When alloy is solution treated and aged at lower temperature, the uniformly distributed θ" precipitates present. Typical bright field image and its corresponding SADP are presented in Fig. 2.15.

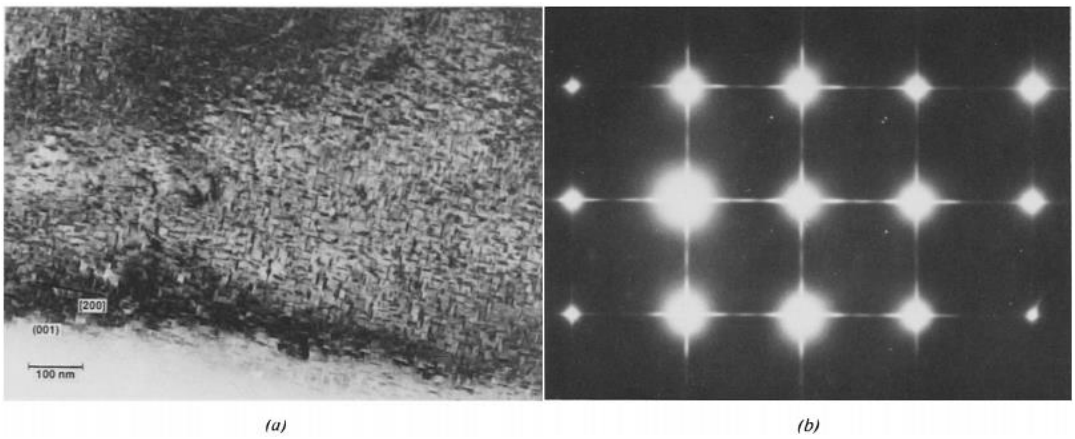

Fig. 2.15 a) Bright field electron micrograph of 2219 after 4.7 d aging at 130ºC. (b) Corresponding selected area diffraction pattern [78].

When solution treated alloys were aged at higher temperature, θ' precipitates present. Fig. 2.16 shows the typical θ' morphology and its corresponding selected area diffraction pattern.

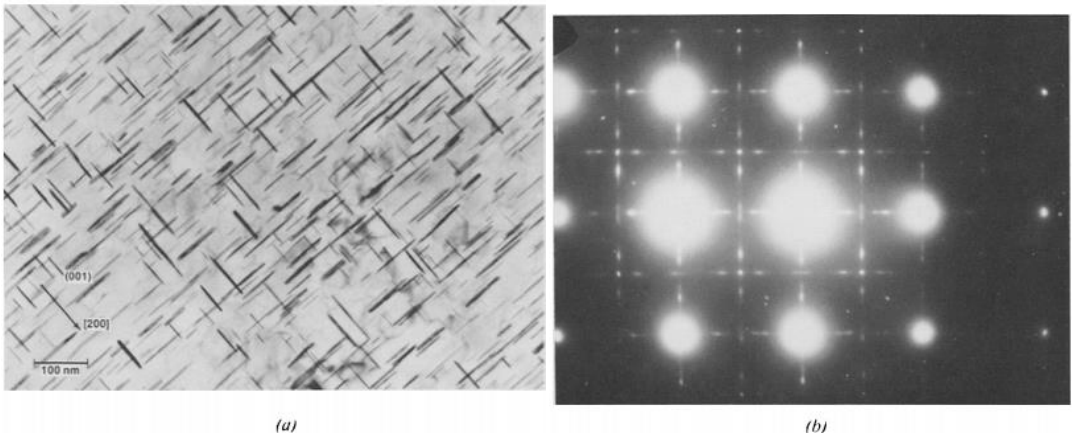

Fig. 2.16 (a) Bright field electron micrograph of θ', (b) Corresponding selected area diffraction pattern [78].

2.3.3 Dispersoid strengthening

Dispersoid strengthening is a very important strengthening method in Al-Si alloys especially at elevated-temperature. Since dispersoids are usually large in size and hard thus the mechanism for dispersoid strengthening can be explained by the

Orowan mechanism discussed in previous section.

Dispersoid strengthening is often desired for elevated-temperature application, as fine precipitates that formed during solution treatment and ageing can be coarsened, resulting in poor elevated-temperature properties [72]. However, dispersoids are usually precipitated during annealing process in which temperature is significantly higher than ageing temperature, thus their thermal stability is better than precipitates which formed during relatively lower temperature (~200^{o}C) [79].

Alloying elements to form dispersoids is increasingly becoming a common practice. However, elements that can be potentially applied to produce castable and dispersoid-strengthening aluminum alloys with high-temperature stability and strength must [80, 81]:

1) Be capable of forming a suitable strengthening dispersoids, and contain a large volume fraction, which must be thermodynamically stable and difficult to shear by dislocations at the intended service temperature. These precipitated phases should also exhibit a similar crystal structure, and a low lattice parameter mismatch with the Al solid solution.

2) Show low solid solubility in Al matrix: A low equilibrium solid solubility at the intended service temperature is necessary to retard volume diffusion-controlled coarsening and prevent dissolution of the precipitated phases. By the lever rule, limited solid solubility also maximizes the equilibrium volume fraction of the dispersoids.

3) Low diffusivity in Al matrix. Limited diffusivity of the solutes in Al should also limits volume diffusion-controlled coarsening, allowing the dispersoids to remain effective barriers to dislocation motion at elevated temperatures.

4) Retain the ability for the alloy to be conventionally solidified.

α- dispersoids in Al-Si alloys

The dispersoids formed in Al-Si alloys vary with many factors, including alloy composition, thermal treatment etc. The α-dispersoids are the most common dispersoids formed in Al-Si alloys. This section deals with the α-dispersoids that formed in Al-Si alloys with Mn and/or Mo addition.

α-Al(Mn,Fe)Si dispersoids can precipitate when Mn is also present. Mn atoms can dissolve in the Al matrix during the solidification, forming a supersaturated solid solution. During homogenization, α-Al(Mn,Fe)Si dispersoids precipitate from the Al matrix. Study [82] investigated the precipitation behaviour of α-Al(Mn,Fe)Si dispersoids and their effect on mechanical properties during precipitation treatment. Fig. 2.17 shows the precipitation of dispersoids in 3xxx alloy treated at 375 °C for 24 h and their corresponding SADP, and a significant dispersion strengthening effect caused by the precipitation of fine uniformly distributed α-Al(Mn,Fe)Si dispersoids during precipitation treatment is achieved [82].

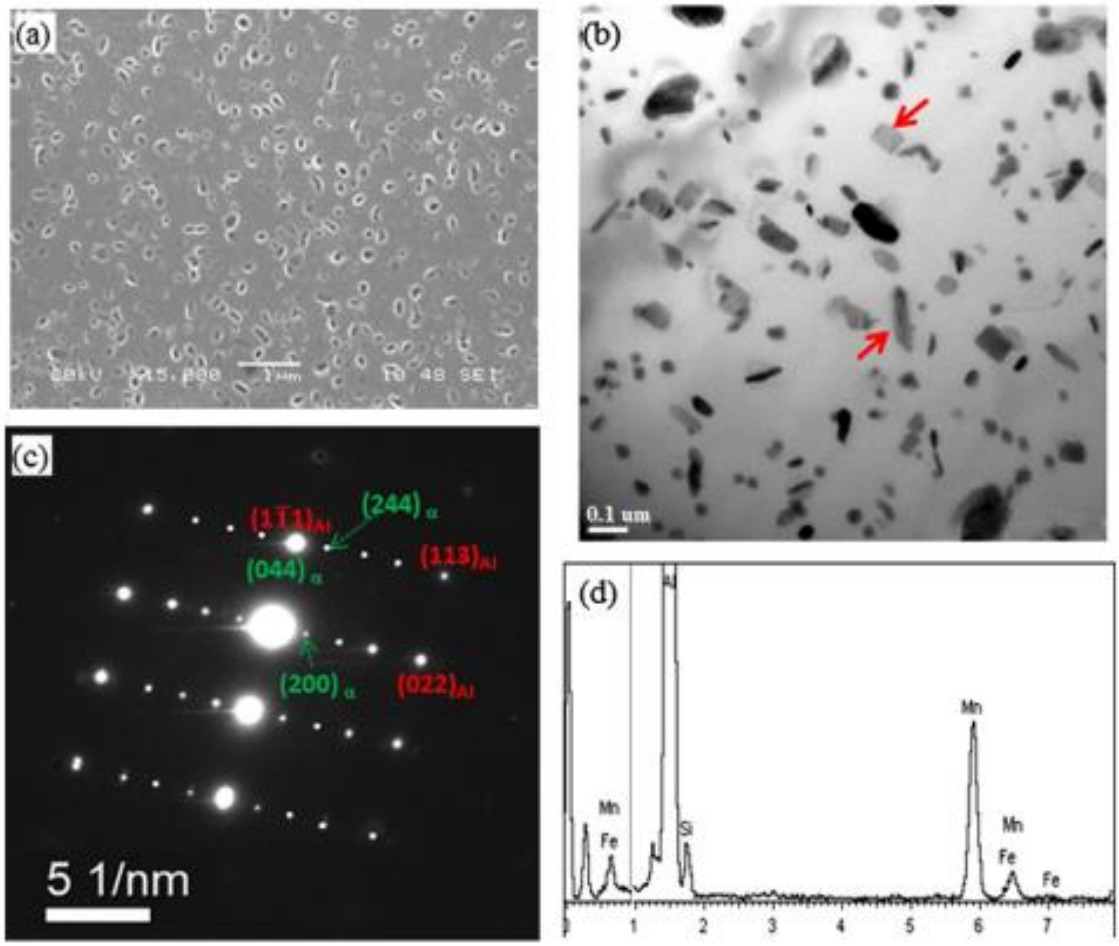

Fig. 2.17 Type of morphology of dispersoids: (a) SEM and (b) TEM image and SADP along [211]Al (c) as well as the TEM-EDS results of dispersoids (d) in the sample treated at 375 °C for 48 h [82].

In addition, α-Al(Mn,Fe)Si are confirmed to heterogeneously nucleated on the pre-precipitated Mg_2Si needles [24, 71, 72], leading to the large number density in the matrix. The diffraction pattern of α-Al(Mn,Fe)Si dispersoids are also shown in Fig. 2.18 which is confirmed to be coherent with the matrix [83]. The size of the α-Al(Mn,Fe)Si is reported to be in the range of 60-100nm [24, 71, 72]. Thus, pronounced strengthening can be achieved via formation of fine and large number density of α-Al(Mn,Fe)Si dispersoids [84].

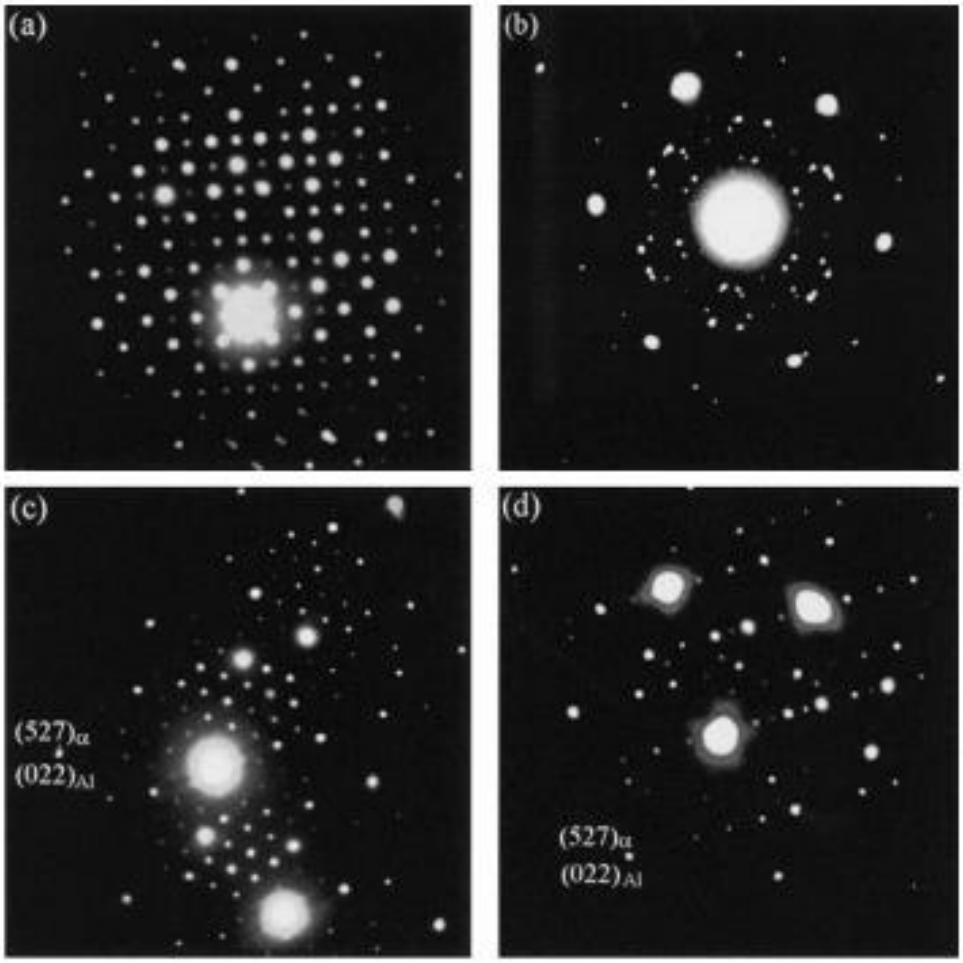

Fig. 2.18 Diffraction patterns of α-dispersoids in 3003 alloy after heating to 500 °C [83].

Mo is a transition metal of the sixth group in the periodic table, which is traditionally used as an alloying element for high-strength stainless steels [85]. However, it has not received much attention regarding Al alloys, except few applications in the rapid-solidification powder metallurgy for elevated temperature properties [85-88]. Al–Mo binary phase diagram (Fig. 2.19) shows Mo can promote many Al_xMo phases during solidification [89-92]. Mo is also reported to possess low diffusivity in Al [51], making it a potential dispersoid former.

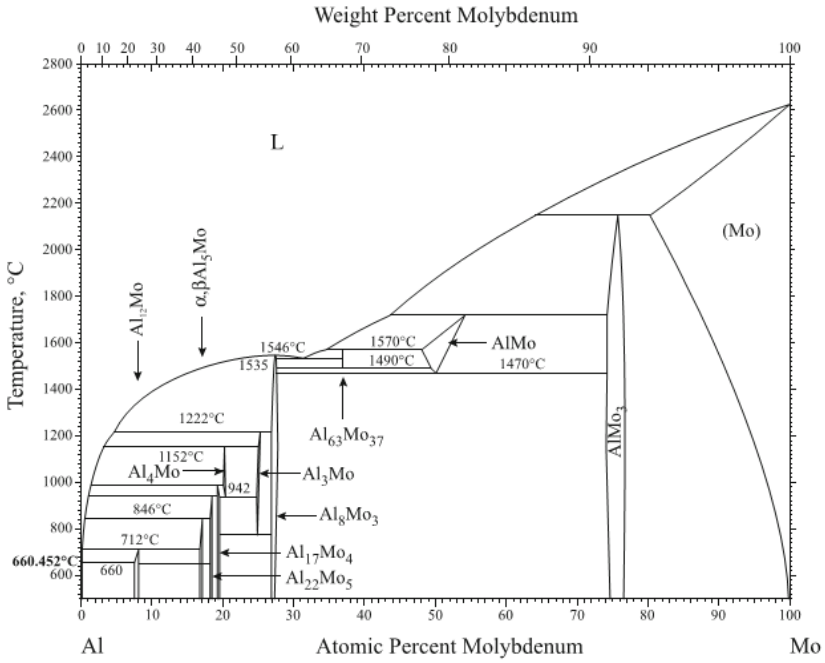

Fig. 2.19 Al–Mo phase diagram [91].

Mo has been applied in Al–Si 356 cast alloy to promote Mo-containing dispersoids [51, 93]. Mo addition helps to form thermally stable nano-scale α-Al(Mo,Fe)Si dispersoids (Fig 2.20), which leads to higher mechanical properties at elevated temperature [51]. Farkoosh *et al.* also employed combined addition of Mo and Mn in one Al–Si–Cu–Mg cast alloy to form large volume of thermally stable α-Al(Mn,Mo,Fe)Si dispersoids, resulting in more uniform distribution of α-Al(Mn,Mo,Fe)Si dispersoids and elimination of dispersoid free zone (DFZ), due to the opposite partitioning of the Mo and Mn solute atoms during solidification (shown in Fig. 2.21) [93]. In summary, Mo can form a large amount of metallurgical stable dispersoids in Al–Si cast alloys even when added at low levels [51, 92, 94, 95], make it a promising element as α-Al(Mn,Mo,Fe)Si dispersoid former. These dispersoids are thermally stable, hence, significant enhancement in mechanical properties at elevated temperature including the strength and creep resistance was achieved [51, 72, 93].

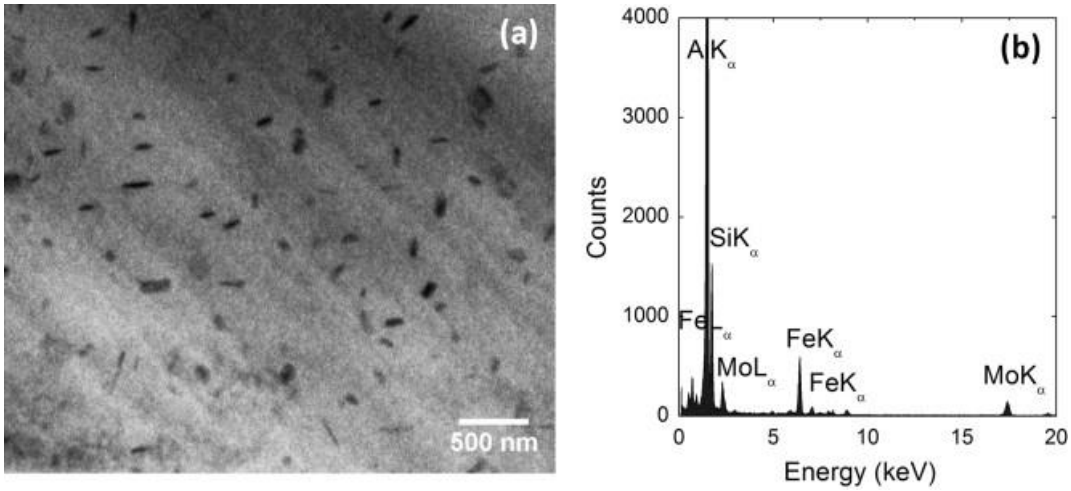

Fig 2.20 (a) Bright field TEM micrograph showing the Al(Mo,Fe)Si dispersoids in the interdendrite regions of the MG3R3M alloy formed after 10 h of solution treatment at 540 °C. (b) EDS spectrum of the Al(Mo,Fe)Si dispersoids [51].

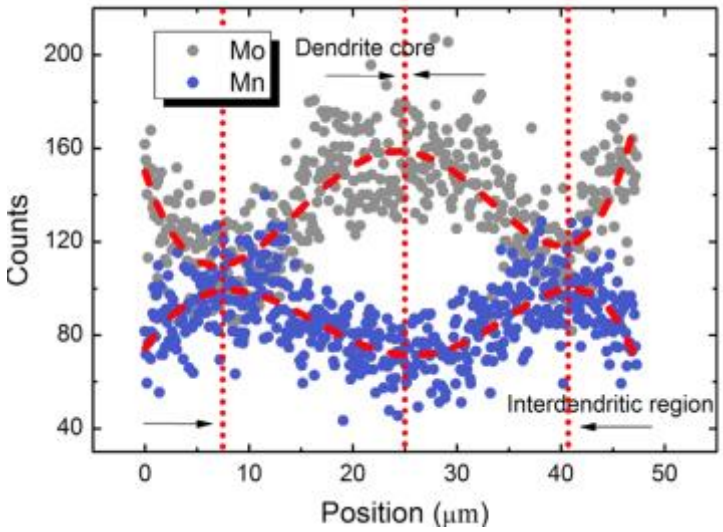

5)

Fig. 2.21 EDS elemental line scanning across a dendrite cell showing the concentration gradients of Mo and Mn (microsegregation) in the as-cast Al–7Si–0.5Cu–0.3Mg–0.1Fe–0.3Mo–1.5Mn alloy [93].

2.4 Creep behaviour and its mechanism

Creep is a permanent deformation of materials under constant load and at constant temperature. It can occur as a result of long-term exposure to high levels of stress that are still well below the yield strength of the material.

2.4.1 Creep stages

Generally, for tensile creep test, there are three different stages as shown in Fig. 2.22. The primary creep stage is characterized with very high strain rate due to the material elastically and plastically responds to the applied load. As the deformation continues, the material is continually strengthened by work hardening, which leads to the gradual decrease of the creep rate. As the deformation continues, primary creep stage gradually transits into the secondary creep stage. This stage is also called the steady-state creep. The creep rate remains nearly unchanged for a prolonged period under a constant load. This is an interplayed result between recovery and hardening. The secondary creep region usually dominates most of the time of creep deformation. As creep proceeds, the secondary creep changes into the third stage (tertiary creep). Tertiary creep only occurs in tensile creep test. As continuous deformation produces voids or internal cracks which decrease the cross-section hence increase the stress. As a result, a necking occurs at tertiary stage of the creep, which ends up the fracture of the materials (Fig. 2.22). The tertiary stage creep possesses a much higher creep rate.

For compression creep curves, there is no such necking as occurred in tensile creep tests, due to the geometric effect that the sample cross-section swelled as the deformation continues. Thus, the steady-state creep stage dominated during compression creep. As shown in Fig. 2.22 (dotted lines), no tertiary creep can be observed during compression creep test.

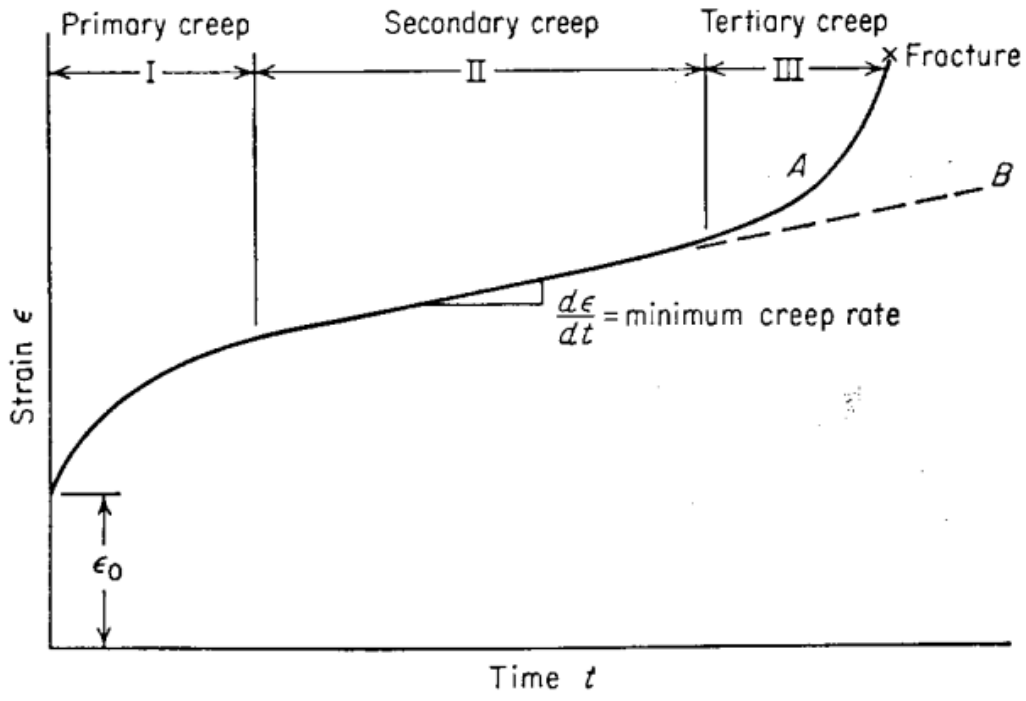

Fig. 2.22 Typical creep curve showing the three steps of creep (The dotted line shown in the figure is for the compression creep curves) [70].

2.4.2 Parameters of creep properties

Many researchers [96, 97] proposed many equations to evaluate creep properties of metals and alloys. These equations summarized the total strain and time dependent creep rates. When the creep strain and temperature are lower, the creep strain [98] can be expressed as:

$$\varepsilon(t) = \left({}^{KT}/_{\lambda}\right) \ln\left(1 + {}^{t}/_{\tau}\right) \qquad \text{Eq. 2.11}$$

where λ and τ are constant, T is the experimental temperature. ${}^{KT}/_{\lambda}$ and τ are determined by experimental condition. When creep is controlled by dislocation motion, the minimum strain rate ε_m of dispersoid-strengthened Al alloys can be described by a power-law equation [99]:

$$\varepsilon_m = A_a\left(\sigma/_G\right)^{\dot{n_a}}\exp\left(-Q_a/_{RT}\right) \qquad \text{Eq. 2.12}$$

where A_a is a constant for all stresses and temperatures, σ is the applied stress, G is the shear modulus, n_a is the apparent stress exponent, Q_a is the apparent activation energy for creep, R is the gas constant and T is absolute temperature. The shear modulus is temperature dependent and calculated from the equation (given as $G = 25.4\left[1 - 0.5\,(t - 300)/_{933}\right]$ with GPa unites) [99]. Under the fixed constant in temperature, the stress exponent n_a can be calculated according to the following equation:

$$n_a = \partial \ln \dot{\varepsilon_m}/_{\partial \ln \sigma} \qquad \text{Eq. 2.13}$$

When specimen was subjected to several temperatures while under constant stress the activation energy Q_a can be measured through the temperature-cycling method [100]. The apparent activation energy was then determined after each temperature changes for the relation as follows:

$$Q_a = \frac{R\ln\left(\dot{\varepsilon_1}/_{\dot{\varepsilon_2}}\right)}{(T_1 - T_2)/_{T_1 T_2}} \qquad \text{Eq. 2.14}$$

where $\dot{\varepsilon_1}$ and $\dot{\varepsilon_2}$ are the instantaneous creep rates immediately before and after the change in temperature from T1 to T2. The activation energy is designated as the apparent energy for creep because it is empirically determined.

The values of n_a can be used to estimate the creep mechanism in unreinforced Al alloys. However, in dispersoid strengthened Al alloys, the apparent stress exponent n_a is higher and variable [101-103]. This behaviour can be modeled by introducing in a threshold stress, σ_{th}, below which creep is not measurable experimentally [101]. After incorporating σ_{th}, $\varepsilon_m = A_a\left(\sigma/_G\right)^{\dot{n_a}}\exp\left(-Q_a/_{RT}\right)$ Eq. 2.12 can be modified as follows [101, 103]:

$$\dot{\varepsilon}_m = A_a\left(\frac{\sigma-\sigma_{th}}{G}\right)^{n_t}\exp\left(-\frac{Q}{RT}\right) \qquad \text{Eq.2.15}$$

The incorporation of a threshold stress into the analysis is usually effective in giving values of n_t which is similar to those obtained in the unreinforced matrix materials. According to the different n_a values, the creep mechanisms can be estimated [102, 104, 105].

2.4.3 Creep mechanism

Creep mechanism is highly dependent on the applied temperature and stress. Ashby [106] plots creep deformation mechanism map according to the temperature and stress as shown in Fig. 2.23. The creep mechanism subdivided into four categories: dislocation glide creep, dislocation creep, Coble creep, Nabarro-Herring creep.

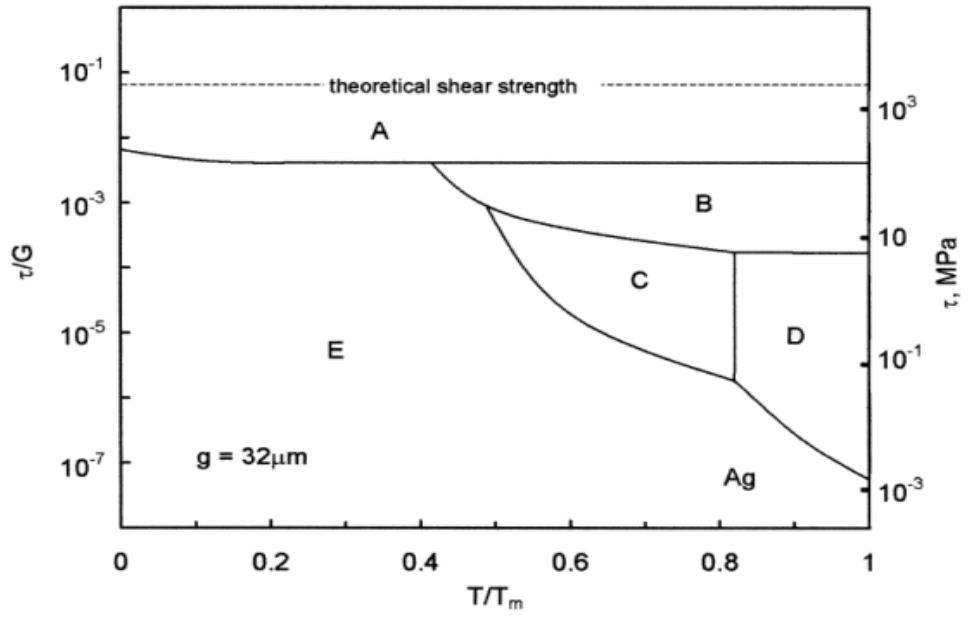

Fig. 2.23 Ashby deformation map of silver. A – Dislocation glide creep, B –Dislocation creep, C – Coble creep, D – Nabarro-Herring creep, E – Elastic deformation [106].

L. Shi *et al.* [105] summarized stress exponent, activation energies and the

corresponding mechanisms, which are listed in Table 2.2.

Table 2.2 Stress exponent and activation energy values for creep mechanisms [105].

Mechanism	Stress Exponent
Dislocation glide and climb, controlled by climb.	4.5
Dislocation glide and climb, controlled by glide.	3
Dissolution of dislocation loops	4
Dislocation climb from Bardeen-Herring sources	3 to 5
Non-conservative motion of jogged screw dislocations	3
Nabarro-Herring creep at subgrain boundaries	3
Climb of dislocations in 2-dimensional subgrain boundaries	3
Climb of dislocations in subgrain boundaries of finite width	4
Recovery creep, slip distance is independent of mesh size	4
Recovery creep, including distribution of dislocations link lengths	3 to 5
Network coarsening by jog-controlled climb	3
Climb of dislocation links with a 3D network, average slip distance equals mesh spacing of network	3
Climb of dislocation links with a 3D network, average slip distance is independent of mesh size	4

Dislocation link collisions with a 3D dislocation network,	3
Dislocation climb of extended dislocations	3 to 5
Dislocation link length statistics for a 3D dislocation network	3

This table can be of great importance in determining the creep mechanisms based on stress exponent. However, it should be noted that due to the complexity of creep, the mechanism is often the result of interrelations of several mechanisms.

2.4.4 Strategies to improve creep resistance

The creep resistance of materials could be improved by the following methods [107]:

1. Dispersoids are effective for improving the creep resistance as well because they are usually thermally stable at elevated temperature. Besides, their coarsening rate is lower than precipitates particles.

2. Solid solution hardening is also beneficial to creep resistance. This is best achieved by use of solutes differing markedly in atom size and valence from the parent metal. Long range order in solid solutions provides a further contribution to the creep strength of solid solutions, because the super-lattice dislocations are paired to preserve order across the slip plane and are thus similar to extend dislocations.

3. Precipitates can also increase the creep strength, and a theory provides an estimate of the critical spacing if dispersion for optimum strength in terms of that just small enough to prevent dislocations bowing around the particles. Some precipitates form more readily than others on dislocations, and thus are important source of strengthening, both at low and elevated temperatures. Precipitates which form during creep are particularly useful if they nucleate on dislocations.

4. Creep resistance is greater in a matrix of low stacking fault energy, because the dislocations are dissociated, and thus more difficult to cross-slip and to climb, in order to avoid obstacles. The stacking fault energy of a pure metal can be lowered by solute additions. For this purpose, solutes of high valence are best because they more readily increase the electron/atom ration, and thus decrease stacking fault energy.

2.5 Thermal exposure behaviour of Al–Si alloys

Piston operation induces a complex combination of thermal stresses and high cycle, high temperature mechanical cycles in the material. The typical working temperature of these parts can reach up to 250^{o}C-300^{o}C, as is shown in Fig. 2.24.

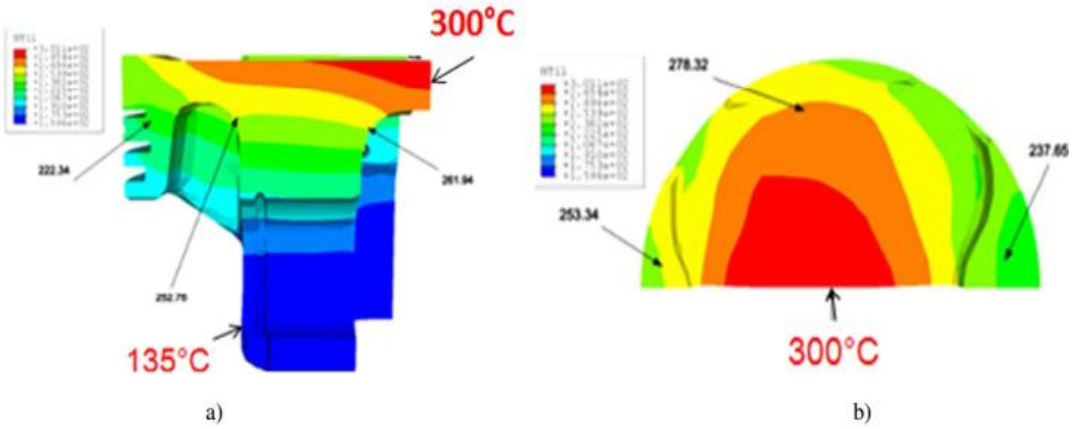

Fig. 2.24 The steady-state temperature distribution within a high-performance piston obtained by FE simulation [108].

For Al-Si alloys, the mechanical properties often deteriorate with increasing thermal exposure at 200 ^{o}C-300 ^{o}C. Hardness-time-temperature (HTT) curves can be applied to evaluate their thermal stability, as they offer an immediate overview of the mechanical response after thermal exposure [109], as such experimental data are useful for validating the simulations of piston temperature distribution. Fig. 2.25 presents the HTT curve of Al-Si 4032 alloy after forging and T6 heat treatment. The

microhardness decreases with increasing temperature and increasing time. Moreover, the degree of degradation is greatly related to the thermal exposure temperature. When temperature is lower than 200^{o}C, the hardness remains relatively stable even with prolonged exposure. However, when temperature exceeds 200^{o}C, the higher the temperature, the faster the decreasing of mechanical properties.

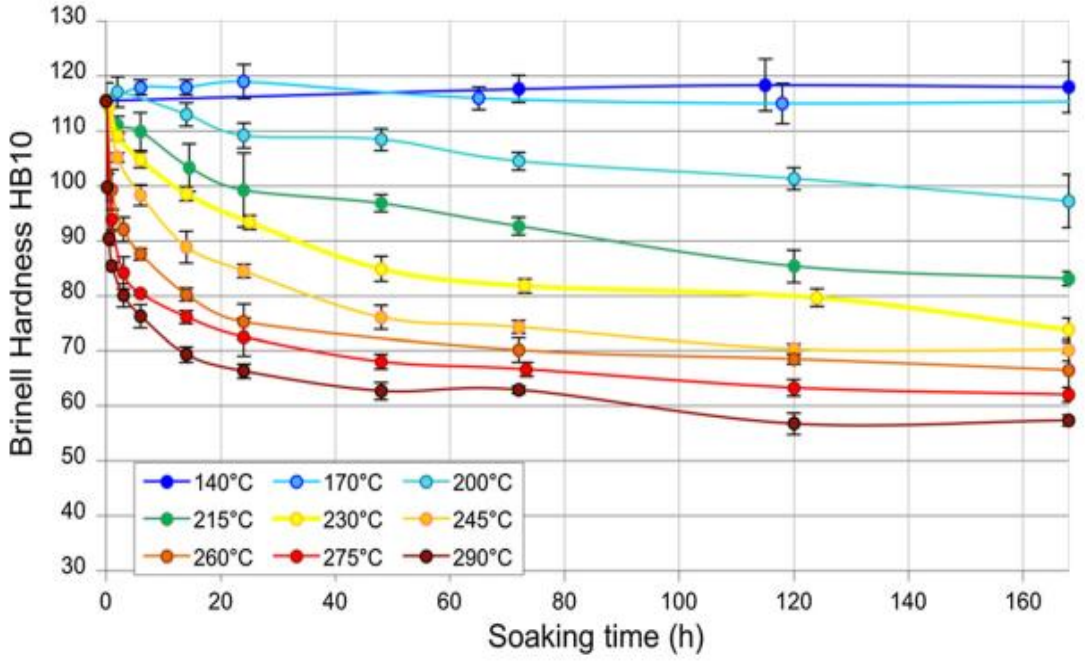

Fig. 2.25 Hardness-time-temperature (HTT) curves of the EN AW-4032 alloy, after forging and T6 heat treatment [109, 110].

As discussed in previous sections, the precipitates and dispersoids are crucial to the mechanical properties of Al–Si alloys. They can precipitate during a variety of thermal treatments, such as ageing or annealing process thus strengthening Al-Si alloys. During prolonged thermal exposure, the precipitates will experience certain degree of coarsening, leading to the deterioration of mechanical properties. Thus, it is important to study the kinetics of precipitates/dispersoids under thermal exposure. This has special practical importance for Al–Si alloys designed for prolonged thermal

exposure.

2.5.1 Coarsening of precipitates

When precipitation from supersaturated solid solution is completed, prolonged treatment leads to precipitate coarsening driven by the interfacial free energy between the precipitate and the matrix (Ostwald ripening). The physical process by which the microstructure coarsens and releases its excess surface energy is due to the higher solubility of small particles, since these have a larger ratio of surface area to volume. The larger particles thus grow at the expense of the smaller ones, and the growth kinetics depend upon the rate-controlling step in the process. Those particles which have a radius $< r^*$ (critical particle radius) will have a negative growth rate according to equation and will thus shrink. When the size of a group of particles reaches zero, they are removed from the size distribution [56].

The LSW theory showed that the average precipitate size r increases with time t according to:

$$r^3 - r_0^3 = Kt \qquad \text{Eq. 2.16}$$

Where r is the average precipitate radius at time t, r_0 is the average initial precipitate radius at the onset of coarsening, and K is the coarsening rate constant given by:

$$K = \frac{8D_\gamma V_m}{9RT}\frac{C_e(1-C_e)}{(C_p-C_e)^2} \qquad \text{Eq. 2.17}$$

Here, D_γ is the diffusivity of elements in Al matrix, V_m is the precipitate-matrix interfacial free energy, and C_e is the equilibrium solubility (assuming a planar interface) of the solute species in the precipitate and matrix phases, respectively.

For any thermal resistant alloy, it is essential that the dispersoids/precipitates resist coarsening during prolonged exposure at elevated service temperatures. This is especially imperative for Al–Si alloys because of the generally limited solubility of most solutes in Al and the concomitant limited volume fractions of dispersoid phases [81].

For Al-Si alloys, the precipitates experience coarsening during prolonged thermal exposures. As mentioned in previous sections, in Al–Si alloys with Cu addition, Al_2Cu is the main strengthening phases. During ageing, GP zone, θ", θ' and θ can precipitate. The GP zones and the matrix have the same crystal structure. The transition metastable phases θ" and θ' are less stable than the equilibrium θ phase. Fig. 2.26 listed the solvus temperature of all Cu metastable and stable phases.

As is indicated, if the supersaturated solid solution is aged at temperatures below the solvus temperature of all metastable phases, the experimentally observed ageing sequence is supersaturated solid solution →GP zones →θ" → θ' → θ [56].

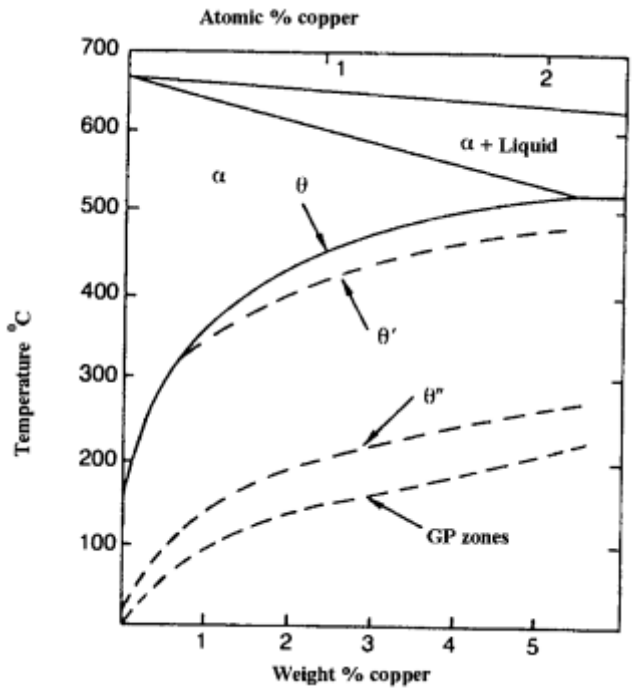

Fig. 2.26 The Al–rich end of the Al-Cu phase diagram showing the metastable GP zone, θ" and θ' solvus temperature [111].

However, when Al–Cu alloys are further annealed at higher temperature (250^{o}C), a part of θ" precipitates dissolve to provide extra Cu atoms because θ' has a higher Cu concentration than θ" (Al_3Cu). The transformation of θ" → θ' takes place simultaneously at different sites. With proceeding transformation, the θ' grows and form a perfect θ' precipitate via the coalescence of the adjacent sections [112]. Fig. 2.27 shows the continuous coarsening of θ' to θ during the thermal exposure at 250^{o}C from 5h, 30h up to 600h, it is evident that the volume of equilibrium θ phases increases with prolonged thermal exposure.

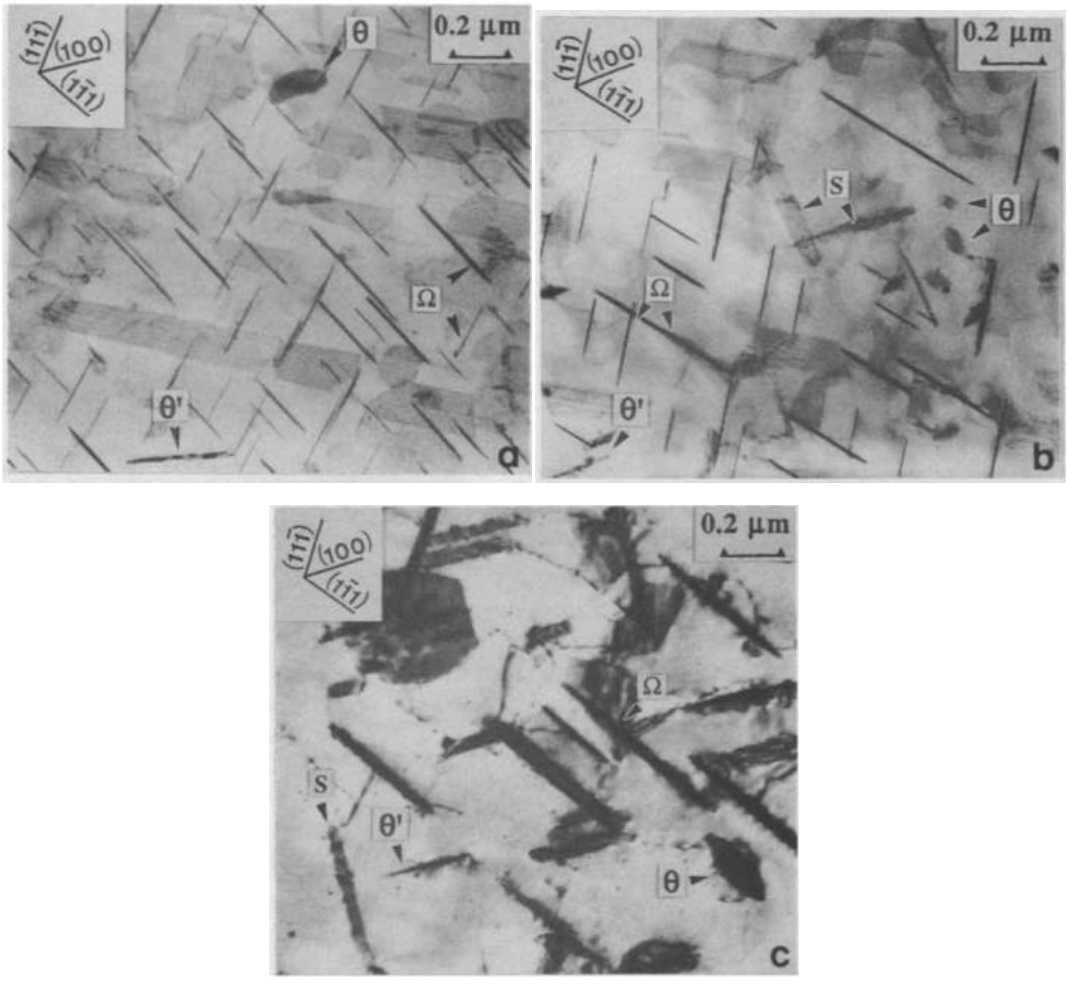

Fig. 2.27 Transmission electron micrographs of Al–Cu–Mg–Ag alloy, showing

changes in microstructure with ageing at 250 ºC. (a) 5 h at 250 ºC; θ' and θ phase. (b) 30 h at 250 ºC; coarser θ' and θ particles. (c) 600 h at 250 ºC; very coarse Ω precipitates, large θ' and θ particles [113].

When thermal exposure was prolonged to 2400h at 250ºC, equilibrium θ-Al_2Cu phases was the only phases without any trace of any metastable precipitates left in the matrix, as is presented in Fig. 2.28.

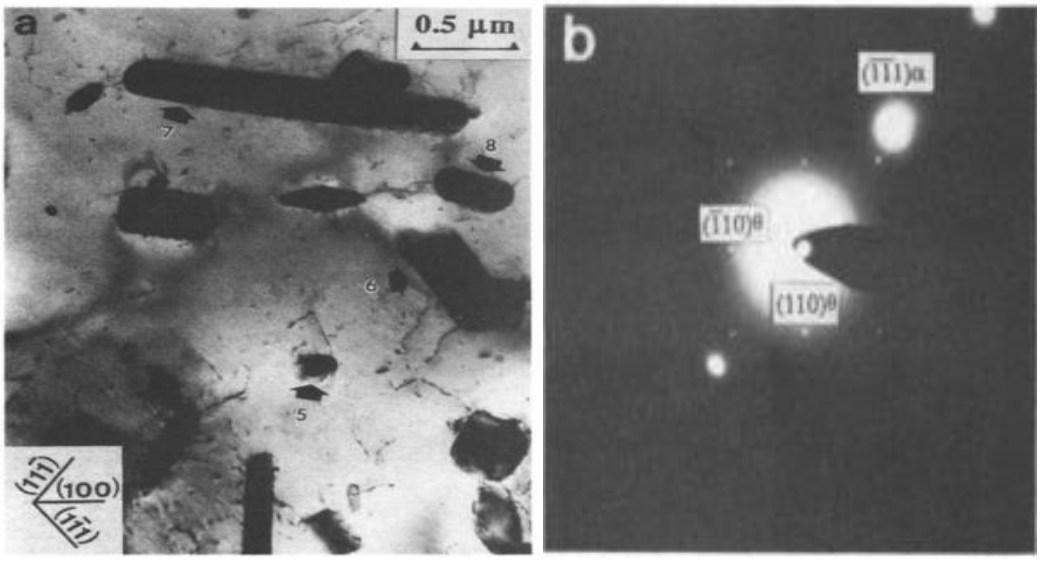

Fig. 2.28 Transmission electron micrograph from alloy after 2400 h at 250ºC. The electron beam is parallel to [001] α and several large blocky and rod-like precipitates are observed. (b) Micro-beam electron diffraction pattern from precipitate 7 indexed as θ($A1_2Cu$) phase in the [001]θ // [001]α [113].

The evolution of Mg_2Si precipitates during prolonged thermal exposure has not been investigated as thoroughly as Al_2Cu precipitates. However, the coarsening of Mg_2Si is also inevitable especially at prolonged exposure at elevated temperature (250ºC-350ºC). Fig. 2.29 presents the TEM bright field micrograph of rod-like equilibrium phase Mg_2Si after treated at 635K, and its corresponding SADP shows

that its crystal structure is not coherent with the Al matrix, thus the strengthening effect is much poorer than β" precipitates.

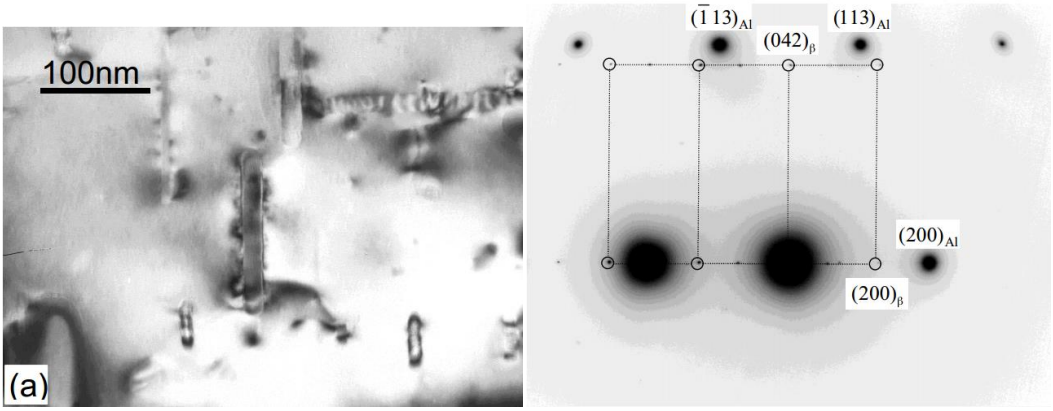

Fig. 2.29 Bright field TEM image of rod-like equilibrium β-Mg_2Si precipitates and its corresponding SADP [67].

2.5.2 Coarsening of dispersoids

Coarsening of dispersoids is also very common in alloys with dispersoids as the main strengthening phase under thermal exposure. The mechanism of coarsening of dispersoids can also be accounted by Ostwald ripening. However, the dispersoids can retain better stability at prolonged thermal exposure due to their relatively higher precipitation temperature than precipitates. Fig. 2.30 shows the evolution of α-dispersoids during long thermal exposure at two different temperatures, 350 ^{o}C and 400^{o}C respectively. It is evident that the α-dispersoids generally exhibit good thermal stability compared with precipitates discussed in section 2.5.1. The α-Al(Mn,Mo,Fe)Si dispersoids (Fig. 2.30b and Fig. 2.30d) shows improved thermal stability than α-Al(Mn,Fe)Si (Fig. 2.30a and Fig. 2.30c) at identical thermal exposure condition characterized with less diameter increase. The improved thermal stability of

α-Al(Mn,Mo,Fe)Si is related to its lower coarsening rate than α-Al(Mn,Fe)Si, and this can be ascribed to the Mo's four order's magnitude less of diffusion rate than Mn [81, 114].

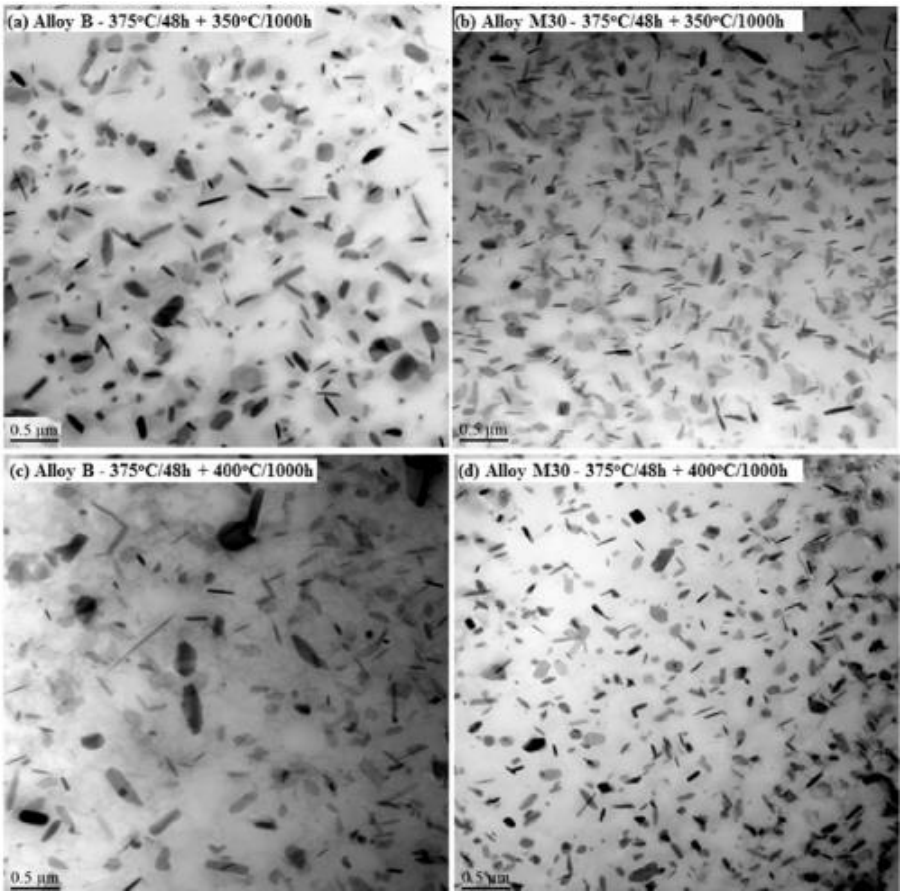

Fig. 2.30 Behaviours of α-dispersoids during long thermal holding [115].

2.5.3 Intermetallics changes during thermal exposure

In addition to the coarsening of precipitation and dispersoids, factors that should be considered for Al-Si alloys with thermal exposure at elevated-temperature include: intermetallics changes and synergistic effects of above-mentioned mechanisms [116]. One good example is the coarsening of eutectic Si particles in Al-13%Si piston alloys. The eutectic Si particles experience continuous fragmentation and spheroidization during prolonged thermal exposure at elevated-temperatures, consequently, leading to the deterioration of mechanical properties [117-119].

As a matter of fact, the deterioration of mechanical properties under prolonged thermal exposure often involves with the synergistic influence of various factors, hence measures to improve thermal stability in Al-Si cast alloys depend on what properties are important in a particular application [116]. When strength is critical which is often the case in Al-Si alloys, coarsening of the matrix precipitates during elevated-temperature service will be important, thus providing extra strengthening phases or retardation of coarsening process would be reasonable methods to improve its thermal stability. In conclusion, the deterioration of mechanical properties might be universal during prolonged thermal exposure, but the exact mechanisms and measures to improve the thermal stability should be dealt with extra prudence in certain circumstances.

References

[1] F.C.R. Hernandez, J.M.H. Ramírez, R. Mackay, Al-Si Alloys: Automotive, Aeronautical, and Aerospace Applications, Springer International Publishing 2017.

[2] M. Javidani, D. Larouche, Application of cast Al-Si alloys in internal combustion engine components, International Materials Reviews 59(3) (2014) 132-158.

[3] S. Shankar, Y. Riddle, M. Makhlouf, Eutectic solidification of aluminum-silicon alloys, Metallurgical and Materials Transactions A 35(9) (2004) 3038-3043.

[4] M. Tash, F.H. Samuel, F. Mucciardi, H.W. Doty, Effect of metallurgical parameters on the hardness and microstructural characterization of as-cast and heat-treated 356 and 319 aluminum alloys, Materials Science and Engineering: A(1-2) (2007) 185-201.

[5] K. Gall, N. Yang, M. Horstemeyer, D.L. McDowell, J. Fan, The debonding and fracture of Si particles during the fatigue of a cast Al-Si alloy, Metallurgical and Materials Transactions A 30(12) (1999) 3079-3088.

[6] K.S. Chan, P. Jones, Q. Wang, Fatigue crack growth and fracture paths in sand cast B319 and A356 aluminum alloys, Materials Science and Engineering: A 341(1) (2003) 18-34.

[7] D.A. Lados, D. Apelian, Fatigue crack growth characteristics in cast Al–Si–Mg alloys: Part I. Effect of processing conditions and microstructure, Materials Science and Engineering: A 385(1) (2004) 200-211.

[8] S. Khan, R. Elliott, Quench modification of aluminium-silicon eutectic alloys, Journal of Materials Science 31(14) (1996) 3731-3737.

[9] E.-B. Talaat, F. Hasse, Solidification mechanism of unmodified and Strontium modified Al–Si alloys, Materials Transactions, JIM 41(4) (2000) 507-515.

[10] M. Moustafa, F. Samuel, H. Doty, Effect of solution heat treatment and additives on the microstructure of Al-Si (A413. 1) automotive alloys, Journal of Materials Science 38(22) (2003) 4507-4522.

[11] O. El Sebaie, A. Samuel, F. Samuel, H. Doty, The effects of mischmetal, cooling

rate and heat treatment on the eutectic Si particle characteristics of A319. 1, A356. 2 and A413. 1 Al–Si casting alloys, Materials Science and Engineering: A 480(1) (2008) 342-355.

[12] N. Haghdadi, A. Zarei-Hanzaki, H. Abedi, O. Sabokpa, The effect of thermomechanical parameters on the eutectic silicon characteristics in a non-modified cast A356 aluminum alloy, Materials Science and Engineering: A 549 (2012) 93-99.

[13] R. Plumb, J. Lewis, The modification of Aluminum-Silicon alloys by Sodium, Journal of the Institute of Metals 86 (1958).

[14] D. Jenkinson, L. Hogan, The modification of aluminium-silicon alloys with strontium, Journal of Crystal Growth 28(2) (1975) 171-187.

[15] S. Kori, B. Murty, M. Chakraborty, Development of an efficient grain refiner for Al–7Si alloy and its modification with strontium, Materials Science and Engineering: A 283(1) (2000) 94-104.

[16] A. Knuutinen, K. Nogita, S. McDonald, A. Dahle, Modification of Al–Si alloys with Ba, Ca, Y and Yb, Journal of Light Metals 1(4) (2001) 229-240.

[17] B. Xiufang, W. Weimin, Q. Jingyu, Liquid structure of Al–12.5% Si alloy modified by antimony, Materials Characterization 46(1) (2001) 25-29.

[18] K. Nogita, A.K. Dahle, Eutectic growth mode in strontium, antimony and phosphorus modified hypoeutectic Al-Si foundry alloys, Materials Transactions 42(3) (2001) 393-396.

[19] F.H. Samuel, P. Ouellet, A.M. Samuel, H.W. Doty, Effect of Mg and Sr additions on the formation of intermetallics in Al-6 wt.% Si-3.5 wt.%Cu-(0.45) to (0.8) wt.% Fe 319-type alloys, Metallurgical and Materials Transactions A 29(12) (1998) 2871-2884.

[20] G. Requena, G. Garcés, M. Rodríguez, T. Pirling, P. Cloetens, 3D architecture and load partition in eutectic Al-Si alloys, Advanced Engineering Materials 11(12) (2009) 1007-1014.

[21] M. Mahta, M. Emamy, A. Daman, A. Keyvani, J. Campbell, Precipitation of Fe rich intermetallics in Cr-and Co-modified A413 alloy, International Journal of Cast

Metals Research 18(2) (2005) 73-79.

[22] Y.M. Han, A.M. Samuel, F.H. Samuel, H.W. Doty, Dissolution of Al_2Cu phase in non-modified and Sr modified 319 type alloys, International Journal of Cast Metals Research 21(5) (2008) 387-393.

[23] E. Sjolander, S. Seifeddine, The heat treatment of Al-Si-Cu-Mg casting alloys, Journal of Materials Processing Technology 210(10) (2010) 1249-1259.

[24] I. Alfonso, C. Maldonado, G. Gonzalez, A. Bedolla, Effect of Mg content and solution treatment on the microstructure of Al-Si-Cu-Mg alloys, Journal of Materials Science 41(7) (2006) 1945-1952.

[25] E.A. Elsharkawi, E. Samuel, A.M. Samuel, F.H. Samuel, Effects of Mg, Fe, Be additions and solution heat treatment on the π-AlMgFeSi iron intermetallic phase in Al-7Si-Mg alloys, Journal of Materials Science 45(6) (2010) 1528-1539.

[26] K. Liu, Solidification of iron-rich intermetallic phases and their effects on tensile properties in Al-Cu 206 cast alloys, Université du Québec à Chicoutimi, 2012.

[27] N.A. Belov, A.A. Aksenov, D.G. Eskin, Iron in Aluminium alloys: impurity and alloying element, Taylor & Francis2002.

[28] V.S. Zolotorevsky, N.A. Belov, M.V. Glazoff, Casting aluminum alloys, Elsevier Science2010.

[29] V. Rivlin, G. Raynor, 4: Critical evaluation of constitution of Al-Fe-Si system, International Metals Reviews 26(1) (1981) 133-152.

[30] S.P. Gupta, Intermetallic compound formation in Fe–Al–Si ternary system: Part I, Materials Characterization 49(4) (2002) 269-291.

[31] T. Maitra, S.P. Gupta, Intermetallic compound formation in Fe–Al–Si ternary system: Part II, Materials Characterization 49(4) (2002) 293-311.

[32] N. Krendelsberger, F. Weitzer, J.C. Schuster, On the reaction scheme and liquidus surface in the ternary system Al-Fe-Si, Metallurgical and Materials Transactions A 38(8) (2007) 1681-1691.

[33] K. Liu, X. Cao, X.-G. Chen, Formation and phase selection of Iron-rich

intermetallics in Al-4.6Cu-0.5Fe Cast Alloys, Metallurgical and Materials Transactions A 44(2) (2013) 682-695.

[34] K. Liu, X. Cao, X.-G. Chen, Solidification of Fe-rich intermetallic phases in Al-4.5Cu-0.3Fe Cast Alloy, Metallurgical and Materials Transactions A 42(7) (2011) 2004-2016.

[35] L. Liu, A.M.A. Mohamed, A.M. Samuel, F.H. Samuel, H.W. Doty, S. Valtierra, Precipitation of β-Al_5FeSi phase platelets in Al-Si based casting alloys, Metallurgical and Materials Transactions A 40(10) (2009) 2457-2469.

[36] J. Hwang, H. Doty, M. Kaufman, Crystallographic studies on the iron-containing intermetallic phases in the 319-type aluminium casting alloys, Philosophical Magazine 88(4) (2008) 607-619.

[37] A. Fabrizi, S. Ferraro, G. Timelli, The influence of Fe, Mn and Cr addtions on the formation of Iron-rich intermetallic phases in an Al-Si die-casting alloys, Shape Casting (2014) 277-284.

[38] W. Bonsack, Discussion on the effect of minor alloying elements on aluminum casting alloys, ASTM Bulletin (1942) 11745-59.

[39] S. Gowri, F.H. Samuel, Effect of Alloying Elements on the Solidification Characteristics and Microstructure of Al-Si-Cu-Mg-Fe-380 Alloy, Metallurgical and Materials Transactions A 25(2) (1994) 437-448.

[40] A. Couture, Iron in aluminum casting alloys - a Literature Survey, International Cast Metals Journal 6(4) (1981) 9-17.

[41] J.Y. Hwang, H.W. Doty, M.J. Kaufman, The effects of Mn additions on the microstructure and mechanical properties of Al–Si–Cu casting alloys, Materials Science and Engineering: A 488(1–2) (2008) 496-504.

[42] J.A. Taylor, G.B. Schaffer, D.H. StJohn, The role of iron in the formation of porosity in Al-Si-Cu-based casting alloys: Part III. A microstructural model, Metallurgical and Materials Transactions A 30(6) (1999) 1657-1662.

[43] P. Crepeau, Effect of iron in Al-Si casting alloys: a critical review (95-110),

Transactions of the American Foundrymen's Society 103 (1995) 361-366.

[44] J.A. Taylor, The effect of iron in Al-Si casting alloys, 35th Australian Foundry Institute National Conference, Australian Foundry Institute (AFI), 2004, pp. 148-157.

[45] L.A. Narayanan, F.H. Samuel, J.E. Gruzleski, Crystallization behavior of Iron-containing intermetallic compounds in 319 Aluminum-Alloy, Metallurgical and Materials Transactions A 25(8) (1994) 1761-1773.

[46] J. Iglessis, C. Frantz, M. Gantois, Conditions de formation des phases de fer dans les alliages Al-Si de pureté commerciale, Mémoires scientifiques de la revue de métallurgie 73(4) (1977) 237-242.

[47] L. Arnberg, L. Backerud, G. Chai, Solidification characteristics of aluminium alloys, American Foundrymen's Society (1996) 137-147.

[48] O. Elsebaie, A.M.A. Mohamed, A.M. Samuel, F.H. Samuel, A.M.A. Al-Ahmari, The role of alloying additives and aging treatment on the impact behavior of 319 cast alloy, Materials & Design 32(6) (2011) 3205-3220.

[49] F. Samuel, A. Samuel, H. Doty, Factors Controlling the type and morphology of Cu-containing phases in 319 Al Alloy (96-30), Transactions of the American Foundrymen's Society 104 (1996) 893-902.

[50] S. Seifeddine, S. Johansson, I.L. Svensson, The influence of cooling rate and manganese content on the β-Al_5FeSi phase formation and mechanical properties of Al–Si-based alloys, Materials Science and Engineering: A 490(1–2) (2008) 385-390.

[51] A.R. Farkoosh, X.G. Chen, M. Pekguleryuz, Dispersoid strengthening of a high temperature Al-Si-Cu-Mg alloy via Mo addition, Materials Science and Engineering: A 620 (2015) 181-189.

[52] T.B. Massalski, Chapter 3 – Structure and stability of alloys, in: R.W. Cahn, P. Haasen (Eds.), Physical Metallurgy (Fourth Edition), North-Holland, Oxford, 1996.

[53] D.G. Eskin, Decomposition of supersaturated solid solutions in Al-Cu-Mg-Si alloys, Journal of Materials Science 38(2) (2003) 279-290.

[54] G.E. Totten, D.S. MacKenzie, Handbook of Aluminum: Vol. 1: Physical

Metallurgy and Processes, Taylor & Francis2003.

[55] F.J. Tavitas-Medrano, A.M.A. Mohamed, J.E. Gruzleski, F.H. Samuel, H.W. Doty, Precipitation-hardening in cast Al-Si-Cu-Mg alloys, Journal of Materials Science 45(3) (2010) 641-651.

[56] J.W. Martin, Precipitation Hardening, Butterworth-Heinemann1998.

[57] A. Mohamed, F. Samuel, A Review on the heat treatment of Al-Si-Cu/Mg casting alloys, Conventional and Novel Applications (2012) 229.

[58] T. Gladman, Precipitation hardening in metals, Materials Science and Technology 15(1) (1999) 30-36.

[59] A.M.F. Muggerud, E.A. Mørtsell, Y. Li, R. Holmestad, Dispersoid strengthening in AA3xxx alloys with varying Mn and Si content during annealing at low temperatures, Materials Science and Engineering: A 567 (2013) 21-28.

[60] Y.J. Li, A.M.F. Muggerud, A. Olsen, T. Furu, Precipitation of partially coherent α-Al(Mn,Fe)Si dispersoids and their strengthening effect in AA 3003 alloy, Acta Materialia 60(3) (2012) 1004-1014.

[61] J.D. Robson, P.B. Prangnell, Dispersoid precipitation and process modelling in zirconium containing commercial aluminium alloys, Acta Materialia 49(4) (2001) 599-613.

[62] R. Kampmann, R. Wagner, Homogeneous second phase precipitation, Materials Science and Technology: A Comprehensive Treatment, Wiley-VCH, Weinheim 5 (1991) 213-303.

[63] D.A. Porter, K.E. Easterling, M. Sherif, Phase transformations in metals and alloys, Third Edition (Revised Reprint), CRC Press2009.

[64] G.A. Edwards, K. Stiller, G.L. Dunlop, M.J. Couper, The precipitation sequence in Al–Mg–Si alloys, Acta Materialia 46(11) (1998) 3893-3904.

[65] S.J. Andersen, H.W. Zandbergen, J. Jansen, C. TrÆholt, U. Tundal, O. Reiso, The crystal structure of the β″ phase in Al–Mg–Si alloys, Acta Materialia 46(9) (1998) 3283-3298.

[66] X. Wang, S. Esmaeili, D.J. Lloyd, The sequence of precipitation in the Al-Mg-Si-Cu alloy AA6111, Metallurgical and Materials Transactions A 37(9) (2006) 2691-2699.

[67] Y. Ohmori, L.C. Doan, K. Nakai, Ageing processes in Al-Mg-Si alloys during continuous heating, Materials Transactions 43(2) (2002) 246-255.

[68] P. Ouellet, F.H. Samuel, Effect of Mg on the ageing behaviour of Al-Si-Cu 319 type aluminium casting alloys, Journal of Materials Science 34(19) (1999) 4671-4697.

[69] R.M. Gomes, T. Sato, H. Tezuka, A. Kamio, Precipitation strengthening and mechanical properties of hypereutectic P/M Al-Si-Cu-Mg alloys containing Fe and Ni, Materials Science Forum, Trans Tech Publishing, 1996, pp. 789-794.

[70] M. Murayama, K. Hono, Pre-precipitate clusters and precipitation processes in Al–Mg–Si alloys, Acta Materialia 47(5) (1999) 1537-1548.

[71] L. Lodgaard, N. Ryum, Precipitation of dispersoids containing Mn and/or Cr in Al–Mg–Si alloys, Materials Science and Engineering: A 283(1–2) (2000) 144-152.

[72] A.R. Farkoosh, M. Pekguleryuz, Enhanced mechanical properties of an Al-Si-Cu-Mg alloy at 300°C: Effects of Mg and the Q-precipitate phase, Materials Science and Engineering: A 621 (2015) 277-286.

[73] J. Gauthier, P. Louchez, F. Samuel, Heat treatment of 319.2 aluminium automotive alloy Part 1, Solution heat treatment, Cast Metals 8 (1995) 91-91.

[74] H. Liu, I. Papadimitriou, F.X. Lin, J. Llorca, Precipitation during high temperature aging of Al−Cu alloys: A multiscale analysis based on first principles calculations, Acta Materialia 167 (2019) 121-135.

[75] A. Biswas, D.J. Siegel, C. Wolverton, D.N. Seidman, Precipitates in Al–Cu alloys revisited: Atom-probe tomographic experiments and first-principles calculations of compositional evolution and interfacial segregation, Acta Materialia 59(15) (2011) 6187-6204.

[76] K. Kim, A. Roy, M.P. Gururajan, C. Wolverton, P.W. Voorhees, First-principles/Phase-field modeling of θ′ precipitation in Al-Cu alloys, Acta

Materialia 140 (2017) 344-354.

[77] S.C. Weakley-Bollin, W. Donlon, W. Donlon, C. Wolverton, J.E. Allison, J.W. Jones, Modeling the age-hardening behavior of Al-Si-Cu alloys, Metallurgical and Materials Transactions A 35(8) (2004) 2407-2418.

[78] J.M. Papazian, A calorimetric study of precipitation in aluminum alloy 2219, Metallurgical Transactions A 12(2) (1981) 269-280.

[79] K.E. Knipling, D.C. Dunand, D.N. Seidman, Criteria for developing castable, creep-resistant aluminum-based alloys - A review, Zeitschrift Fur Metallkunde 97(3) (2006) 246-265.

[80] D. Askeland, P. Fulay, The Science & Engineering of Materials, Cengage Learning2005.

[81] S. Roy, L.F. Allard, A. Rodriguez, T.R. Watkins, A. Shyam, Comparative Evaluation of Cast Aluminum Alloys for Automotive Cylinder Heads: Part I—Microstructure Evolution, Metallurgical and Materials Transactions A 48(5) (2017) 2529-2542.

[82] K. Liu, X.G. Chen, Development of Al–Mn–Mg 3004 alloy for applications at elevated temperature via dispersoid strengthening, Materials & Design 84 (2015) 340-350.

[83] Y.J. Li, L. Arnberg, Quantitative study on the precipitation behavior of dispersoids in DC-cast AA3003 alloy during heating and homogenization, Acta Materialia 51(12) (2003) 3415-3428.

[84] A.R. Farkoosh, M. Pekguleryuz, The effects of manganese on the T-phase and creep resistance in Al–Si–Cu–Mg–Ni alloys, Materials Science and Engineering: A 582(0) (2013) 248-256.

[85] F. Carreño, M. Torralba, M. Eddahbi, O.A. Ruano, Elevated temperature creep behavior of three rapidly solidified Al-Fe-Si materials containing Cr, Mn, or Mo, Materials Science and Engineering: A 230(1–2) (1997) 116-123.

[86] P.Y. Li, H.J. Yu, S.C. Chai, Y.R. Li, Microstructure and properties of rapidly

solidified powder metallurgy Al–Fe–Mo–Si alloys, Scripta Materialia 49(9) (2003) 819-824.

[87] D. Shenglong, L. Dabo, W. Tianzhen, L. Chunyu, Damping behaviour and mechanical properties of rapidly solidified Al–Fe–Mo–Si/Al alloys, Journal of Materials Science 33(8) (1998) 2227-2231.

[88] C.G. McKamey, J.A. Horton, The effect of molybdenum addition on properties of iron aluminides, Metallurgical Transactions A 20(4) (1989) 751-757.

[89] N. Saunders, The Al-Mo system (aluminum-molybdenum), Journal of Phase Equilibria 18(4) (1997) 370-378.

[90] N. Ponweiser, W. Paschinger, A. Ritscher, J.C. Schuster, K.W. Richter, Phase equilibria in the Al–Mo–Si system, Intermetallics 19(3) (2011) 409-418.

[91] H. Okamoto, Al-Mo (Aluminum-Molybdenum), Journal of Phase Equilibria and Diffusion 31(5) (2010) 492-493.

[92] B. Grushko, S.B. Mi, A study of the Al-rich region of the Al-Cu-Mo alloy system, Journal of Alloys and Compounds 509(4) (2011) L30-L33.

[93] A.R. Farkoosh, X. Grant Chen, M. Pekguleryuz, Interaction between molybdenum and manganese to form effective dispersoids in an Al-Si-Cu-Mg alloy and their influence on creep resistance, Materials Science and Engineering: A 627 (2015) 127-138.

[94] M. Eumann, G. Sauthoff, M. Palm, Re-evaluation of phase equilibria in the Al-Mo system, International Journal of Materials Research 97(11) (2006) 1502-1511.

[95] Z. Du, C. Guo, C. Li, W. Zhang, Thermodynamic description of the Al-Mo and Al-Fe-Mo systems, Journal of Phase Equilibria and Diffusion 30(5) (2009) 487-501.

[96] X.W. Wei, X.T. Zu, W.L. Zhou, Compressive creep behaviour of Mg–Li–Al alloy, Materials Science and Technology 22(6) (2006) 730-733.

[97] F. Garofalo, Fundamentals of creep and creep-rupture in metals, Macmillan1965.

[98] F.R.N. Nabarro, The time constant of logarithmic creep and relaxation, Materials Science and Engineering: A 309-310 (2001) 227-228.

[99] R.A. Karnesky, L. Meng, D.C. Dunand, Strengthening mechanisms in aluminum containing coherent Al3Sc precipitates and incoherent Al_2O_3 dispersoids, Acta Materialia 55(4) (2007) 1299-1308.

[100] R. Lund, W. Nlx, On high creep activation energies for dispersion strengthened metals, Metallurgical Transactions A 6(7) (1975) 1329.

[101] Y. Li, T.G. Langdon, A simple procedure for estimating threshold stresses in the creep of metal matrix composites, Scripta Materialia 36(12) (1997) 1457-1460.

[102] M.E. Kassner, K.K. Smith, Fundamentals of Creep in Aluminum Over a Very Wide Temperature Range, in: I. Charit, Y.T. Zhu, S.A. Maloy, P.K. Liaw (Eds.), Mechanical and Creep Behavior of Advanced Materials: A SMD Symposium, Springer International Publishing, Cham, 2017, pp. 57-64.

[103] H.R. Erfanian-Naziftoosi, E.J. Rincón, H.F. López, Creep Properties of the As-Cast Al-A319 Alloy: T4 and T7 Heat Treatment Effects, Metallurgical and Materials Transactions A 47(8) (2016) 4258-4267.

[104] J.S. Robinson, R.L. Cudd, J.T. Evans, Creep resistant aluminium alloys and their applications, Materials Science and Technology 19(2) (2003) 143-155.

[105] L. Shi, D.O. Northwood, Recent progress in the modeling of high-temperature creep and its application to alloy development, Journal of Materials Engineering and Performance 4(2) (1995) 196-211.

[106] M.F. Ashby, A first report on deformation-mechanism maps, Acta Metallurgica 20(7) (1972) 887-897.

[107] R.W.K. Honeycombe, The plastic deformation of metals, Edward Arnold1984.

[108] G. Nicoletto, E. Riva, A. Di Filippo, High temperature fatigue behavior of eutectic Al-Si alloys used for piston production, Procedia Engineering 74 (2014) 157-160.

[109] E. Balducci, L. Ceschini, A. Morri, EN AW-4032 T6 Piston alloy after high-temperature exposure: residual strength and microstructural features, Journal of Materials Engineering and Performance 26(8) (2017) 3802-3812.

[110] L. Ceschini, A. Morri, A. Morri, M. Di Sabatino, Effect of thermal exposure on the residual hardness and tensile properties of the EN AW-2618A piston alloy, Materials Science and Engineering: A 639 (2015) 288-297.

[111] J.L. Murray, The aluminium-copper system AU, International Metals Reviews 30(1) (1985) 211-234.

[112] Z. Shen, Q. Ding, C. Liu, J. Wang, H. Tian, J. Li, Z. Zhang, Atomic-scale mechanism of the θ″→θ′ phase transformation in Al-Cu alloys, Journal of Materials Science & Technology 33(10) (2017) 1159-1164.

[113] S.P. Ringer, W. Yeung, B.C. Muddle, I.J. Polmear, Precipitate stability in Al-Cu-Mg-Ag alloys aged at high temperatures, Acta Metallurgica 42(5) (1994) 1715-1725.

[114] A.R. Farkoosh, X. Grant Chen, M. Pekguleryuz, Interaction between molybdenum and manganese to form effective dispersoids in an Al–Si–Cu–Mg alloy and their influence on creep resistance, Materials Science and Engineering: A 627 (2015) 127-138.

[115] K. Liu, H. Ma, X.G. Chen, Enhanced elevated-temperature properties via Mo addition in Al-Mn-Mg 3004 alloy, Journal of Alloys and Compounds 694 (2017) 354-365.

[116] Accelerated Aging of Materials and Structures: The Effects of Long-Term Elevated-Temperature Exposure, The National Academies Press, Washington, DC, 1996.

[117] R. Fernandez-Gutierrez, G.C. Requena, The effect of spheroidisation heat treatment on the creep resistance of a cast AlSi12CuMgNi piston alloy, Materials Science and Engineering: A (2014) 147-153.

[118] Z. Asghar, G. Requena, E. Boller, Three-dimensional rigid multiphase networks providing high-temperature strength to cast AlSi10Cu5Ni1-2 piston alloys, Acta Materialia 59(16) (2011) 6420-6432.

[119] Z. Asghar, G. Requena, F. Kubel, The role of Ni and Fe aluminides on the

elevated temperature strength of an AlSi12 alloy, Materials Science and Engineering: A 527(21) (2010) 5691-5698.

Chapter 3 Experimental

3.1 Alloy design and sample preparation

Two typical Al-Si cast alloys, including hypoeutectic (Al-6%Si-3.5%Cu 319) and eutectic (Al-13%Si) Al-Si cast alloys were designed with various compositions in the present work. The nominal chemical composition for 319 alloy is Al-6%Si-3.5Cu-0.1Mg-0.1Ti, and the nominal chemical composition for Al-13%Si alloy is Al-13%Si-%1Cu-1%Mg-1%Ni-0.45%Fe-0.3%Mn, the actual chemical composition is shown in Table 1 and Table 2, respectively. Pure Al (99.7 wt.%), pure Mg (99.9 wt.%), Al-25 wt.% Mn, Al-25 wt.% Fe, Al-50 wt.% Si, Al-50 wt.% Cu, and Al-20%Ni master alloys are used for the preparation of various alloys (all the composition in the present work is in wt.% unless otherwise indicated). For each batch, about 3 kg materials were melted by electrical resistance furnace. The melt was kept at 750 ^{o}C for 30 minutes, gently stirred to homogenize the molten metal and avoid entrainment of any surface oxide films, then degassed for 15 minutes and poured into a preheated (250 ^{o}C) permanent steel mould. The dimensions of the cast ingots were 30mm*40mm*80 mm.

Table 3.1 Chemical compositions of the designed alloys

Alloy	Si	Cu	Mg	Ti	Fe	Mo	Mn	Al
L0	5.35	3.19	0.08	0.10	0.28	0	0	Bal
LM1	6.00	3.36	0.09	0.16	0.32	0.19	0	Bal
LM2	6.02	3.42	0.09	0.14	0.31	0.32	0	Bal
LM3	5.92	3.44	0.09	0.13	0.31	0.37	0	Bal
H0	5.81	3.28	0.10	0.11	0.64	0	0	Bal
HM1	6.00	3.35	0.09	0.12	0.67	0.18	0	Bal
HM2	5.94	3.32	0.07	0.10	0.65	0.30	0	Bal
HM3	5.89	3.41	0.11	0.10	0.70	0.41	0	Bal
Mn1	6.18	3.4	0.09	0.12	0.66	0	0.25	Bal
Mn2	6.04	3.39	0.10	0.11	0.68	0.15	0.25	Bal
Mn3	6.18	3.46	0.09	0.14	0.69	0.30	0.26	Bal
Mn4	6.02	3.52	0.09	0.17	0.66	0.41	0.24	Bal

As shown in Table 3.1, the 319 type Al-Si cast alloys were designed with various Fe, Mn and Mo contents in order to study the formation of iron-rich intermetallics with different Fe contents as well as the influence of additions of Mn/Mo on the

transformation of Fe-rich intermetallics. Furthermore, the elevated-temperature properties in alloys with lower Fe content (0.3%) was also studied, by investigation of formation and evolution of dispersoids due to the Mn or/and Mo additions. More Details can be found in Chapter 4 and 5.

In eutectic Al-13%Si piston alloys, whose compositions as shown in Table 3.2, four different Mo content alloys were obtained by adjusting Mo in Mn-containing alloy (B0), aiming to study the combined addition of Mn and Mo on the evolution of dispersoids and then further on the elevated-temperature properties of piston alloys. More details are listed in Chapter 6.

Table 3.2 Chemical compositions of experimental alloys

Alloy	Si	Cu	Mg	Ni	Fe	Mn	P	Mo	Al
B0	12.72	1.06	1.05	1.09	0.41	0.35	0.001	0	Bal.
B1	13.27	1.07	1.01	1.11	0.40	0.3	0.001	0.18	Bal.
B2	13.65	1.04	1.07	1.06	0.49	0.32	0.001	0.25	Bal.
B3	13.13	1.06	1.01	1.11	0.50	0.32	0.001	0.40	Bal.

3.2 Heat treatment design

According to the literature [1-3], different heat treatments were confirmed to promote the precipitation behaviours of dispersoids. In present work, various solution and ageing treatments were also applied to simulate the industrial application of applied alloys and further to study the effect of Mo and Mn on the dispersoids formation and mechanical properties.

For Al-Si 319 cast alloy, the solution treatment temperature was designed from

400-500°C with holding time up to 72 hours (Table 3.3). The samples were heated from room temperature to target temperature with a heating rate 5 °C/s and hold for various times, followed by water quench. Then they were also artificially aged at 155°C /5h.

Table 3.3 Solution treatment conditions

Alloy series	Temperature(°C)	Holding time (h)					
Al-Si-Cu 319 alloy	400	2	6	12	24	48	72
	450	2	6	12	24	48	72
	500	2	4	6	8	12	24
Al-13%Si alloy	520	2	4	6	8	12	24

For Al-13%Si alloy, the heat treatment was conducted at 520 °C with a heating rate 5°C /min. The holding time was ranged from 2h to 24h, followed by quenching into water at room temperature and ageing at 200 ^{o}C/5h. The solution treatment conditions were also shown in Table 3.3.

In order to investigate the thermal stability of properties during the thermal exposure, the alloys were hold at 300 °C for up to 1000 hours (Table 3.4) to simulate the prolonged service time at elevated temperature.

Table 3.4 Thermal exposure conditions

Temperature(°C)	Holding time (h)			
300	100	400	700	1000

3.3 Property measurements

3.3.1 Microhardness

Microhardness was measured on polished sample by Vickers hardness tester at room temperature to evaluate the room-temperature properties. The tests were conducted by NG-1000 CCD microhardness test machine with a load of 10 g and a dwelling time of 20 s. A total of 15 measurements were performed for each sample, and the average was considered to be the hardness of each sample. During the hardness tests, the indentations were guaranteed inside the dendrites without touching the intermetallics formed during the solidification in order to show the evolution of hardness from the Al matrix.

3.3.2 Yield Strength

The compression yield strength test was performed by Gleeble 3800 thermo mechanical testing unit. They were tested at both room temperature (25 ^{o}C) and elevated-temperature (300 ^{o}C) with the fixed strain rate of 0.001 s^{-1}. The samples were machined into cylinder with a 15mm length and 10mm diameter before compression tests. They were heat treated at different temperatures for different periods of time before testing. Conditions selected for the tests can be found in Chapters 4, 5 and 6. The average value obtained from three samples was calculated to be the yield strength of each sample.

3.3.3 Creep resistance

The compressive creep tests were performed at 300 ^{o}C for 96 hours. The samples were machined into cylinder with a 15mm length and 10mm diameter. The data was recorded and further analyzed. For each test, total creep strain and minimum creep rate were calculated to evaluate their creep resistance. Creep load should be carefully selected depending on the sample's elevated-temperature yield strength,

which is fixed to 60-70% of its yield strength.

3.4 Microstructure characterization

3.4.1 Optical microscopy (OM)

Optical microscope (Nikon Eclipse ME600) was used to examine the microstructures of experimental samples in as cast and thermal treated conditions. The samples were sectioned, mounted and metallographically polished. In addition, the image analyzer (CLEMEX JS-200, PE4.0) was used to characterize the Fe-rich intermetallics, dispersoids as well as Si particles, such as the size and aspect ratio. In order to show the distribution of dispersoids and the dispersoid free zone, some selected sample were etched in 0.25 vol. % HF solution.

3.4.2 Scanning electron microscopy (SEM)

A scanning electron microscope (SEM, JSM-6480LV) equipped with energy-dispersive X-ray spectroscopic (EDS) facilities was used to identify the Fe-rich intermetallics in the as-cast samples and quantify the alloying elements in the intermetallics. In addition, SEM was also used to observe the Si particles in both as cast and thermal treated samples, after specimens were deep etched in 20 vol.% NaOH solution for 20 min.

3.4.3 Electron backscatter diffraction (EBSD)

For more accurate phase identification, EBSD was applied to identify the Fe-rich intermetallics by comparing simulated EBSD pattern with standard EBSD patterns of corresponding phases and their mean angular deviation (MAD) value. The maximum value of MAD value 0.7 is accepted for the accurate phase identification [4].

3.4.4 Transmission electron microscopy (TEM)

Specimens for TEM observation were prepared in order to investigate the evolution of precipitates and dispersoids after various thermal treatments. To prepare the TEM specimens, some foils were cut from the thermal treated samples into thin discs (350nm). They were mechanically ground to a thickness of 50 μm and followed by electro-polishing in a twin-jet polishing unit, which was operated at 15 V and −20 °C using a 30% nitric acid and 70% methanol solution. The samples were observed under a TEM (JEM-2100) operated at 200 kV. In addition, X-ray energy-dispersive spectroscopy (EDS) attached to TEM was used to analyze the chemical composition of various precipitates and dispersoids.

References

[1] K. Liu, H. Ma, X.G. Chen, Improving the Elevated-Temperature Properties by Two-Step Heat Treatments in Al-Mn-Mg 3004 Alloys, Metallurgical and Materials Transactions B-Process Metallurgy and Materials Processing Science 49(4) (2018) 1588-1596.

[2] S.K. Shaha, F. Czerwinski, W. Kasprzak, J. Friedman, D.L. Chen, Ageing characteristics and high-temperature tensile properties of Al–Si–Cu–Mg alloys with micro-additions of Mo and Mn, Materials Science and Engineering: A 684 (2017) 726-736.

[3] A.R. Farkoosh, X.G. Chen, M. Pekguleryuz, Dispersoid strengthening of a high temperature Al-Si-Cu-Mg alloy via Mo addition, Materials Science and Engineering: A 620 (2015) 181-189.

[4] M.V. Kral, H.R. McIntyre, M.J. Smillie, Identification of intermetallic phases in a eutectic Al–Si casting alloy using electron backscatter diffraction pattern analysis, Scripta Materialia 51(3) (2004) 215-219.

Chapter 4 Evolution of Fe-rich intermetallics in Al–Si–Cu 319 cast alloy with various Fe, Mo, and Mn contents

Abstract:

In the present work, the precipitation and preferential selection of Fe-rich intermetallics in Al–Si–Cu 319 cast alloys with two Fe contents (0.3 and 0.7 wt.%) and various Mo contents (0-0.4 wt.%) were investigated. The results showed that two types of platelet β-Fe (defined as eutectic β-Fe and pre-eutectic β-Fe) and α-Fe can precipitate depending on the alloy compositions, such as the Fe and Mo contents. Generally, the addition of Mo promotes the formation of α-Fe instead of β-Fe. However, its effect on the phase competition between β-Fe and α-Fe is greatly related to the Fe content. In alloys with low Fe content (0.3%), an addition of 0.37% Mo can promote the complete precipitation of α-Fe and suppress the formation of eutectic β-Fe. However, in alloys with high Fe content (0.7%), only the pre-eutectic β-Fe amount decreases with increasing Mo addition, leaving the eutectic β-Fe almost unchanged. While both pre-eutectic β-Fe and eutectic β-Fe can be fully suppressed with a combined addition of Mn (0.24%) and Mo (0.4%). Compared with Mn, Mo exhibits a stronger effect on the promotion of α-Fe. The combined addition of Mn and Mo can achieve better modifications of both pre-eutectic and eutectic β-Fe in 319 alloys with high Fe content.

4.1 Introduction

Al–Si cast alloys have attracted much attention in the automotive industry owing to their excellent castability and combination of strength and ductility. Further, their high strength-to-weight ratio, high thermal conductivity, and good machinability make them perfect candidates for various manufacturing areas and technology fields [1-3]. In aluminum cast alloys, Fe is often regarded as the most common but inevitable impurity because it can be easily introduced but difficult and expensive to be removed in the commercial practice [4,

5]. Various Fe-rich intermetallics can precipitate during solidification owing to the extremely low solubility of Fe in Al at room temperature compared with its highly solubility in liquid Al. Numbers of Fe-rich intermetallics have been reported for different Al alloys, e.g., Al_3Fe, Al_6Fe and Al_mFe [6-12]. Regarding Al-Si cast alloys, the two most commonly encountered Fe-rich intermetallics are generally Chinese script Al_8Fe_2Si (α-Fe) and platelet Al_5FeSi (β-Fe) [13].

Owing to the platelet morphology of β-Fe, they can block metal feeding and thus generate many porosities during solidification [14], therefore make alloys more easily fractured under tensile loads [2, 4, 15] and then lead to the decreased ductility and strength [16]. Chinese script Fe-rich intermetallics are less detrimental to mechanical properties [2, 17]. Therefore, the modification of Fe-rich intermetallics from platelet into Chinese script has attracted much attention in Al–Si cast alloys. Rapid solidification [18, 19] and melt superheating [20] can promote the formation of Chinese-script Fe-rich intermetallics instead of platelet ones during solidification. However, these methods are limited in the practical application as they can promote hydrogen absorption and increase manufacturing costs. Up to date, chemical modifications of Fe-rich intermetallics are more promising and popular. Some alloying elements such as Cr [21], Co [22] have been reported to be effective either in hindering the platelet β-Fe growth or transferring the morphology of Fe-rich intermetallics from platelet into Chinese script. In the foundry practice, Mn is one of the most economical and effective elements to neutralize the detrimental effects of Fe [2]. However, there are still controversies on the influence of Mn on Fe-rich intermetallics. For instance, some researchers [23, 24] have stated that an Mn/Fe ratio of 0.5 is sufficient to fully modify the β-Al_5FeSi phase, whereas Seifeddine and Johansson *et al.* [25] reported that even for an Mn: Fe ratio of 2:1, the β-Al_5FeSi phase cannot be completely replaced by the α-$Al_{15}(Mn,Fe)_3Si_2$ Chinese script phase. One of the likely reasons can be the different variants of Fe-rich intermetallics, in particular, the platelet β-Al_5FeSi with its various chemical compositions and morphology formed at different temperatures depending on Fe contents. However, the research works on the evolution of Fe-rich intermetallics with Fe contents in Al–Si–Cu cast alloys in terms of

formation temperature, phase type and morphology during solidification are quite limited, and sometimes even contradicting opinions in the literature exists [26, 27].

Molybdenum (Mo) is a transition metal of the sixth group in the periodic table, which is widely used as an alloying element for high-strength steels and stainless steels. However, it has not received much attention regarding Al alloys, and only few applications in the rapid-solidification powder metallurgy for elevated temperature uses have occurred [28]. Recently, it has been applied in Al–Si 356 cast alloys to promote Mo-containing dispersoids [29, 30], in which Mo was reported to suppress the formation of β-Fe intermetallics. However, systematically research on the phase selection and precipitation behaviour of Fe-rich intermetallics with various Mo additions in Al–Si cast alloys is scarce.

In the present study, the precipitation behaviour of Fe-rich intermetallics in Al–Si 319 alloys with two Fe contents (0.3% and 0.7%) was thoroughly studied. The influence of the Mo content on the phase competition of Fe-rich intermetallics was systematically investigated. Furthermore, the effect of the combined addition of Mn and Mo on the different Fe-rich intermetallics was studied and discussed.

4.2 Materials and Methods

The experimental Al–Si–Cu 319 cast alloys were produced with commercially pure Al (99.7%), pure Mg (99.9%), Al–50%Cu, Al–50%Si, Al–25%Fe, Al–25%Mn, and Al–10%Mo master alloys. The chemical composition of experimental alloys analyzed by optical emission spectrometry is listed in Table 1. All alloy compositions in this study are in wt.%, unless otherwise indicated.

In order to investigate the formation and evolution of iron-rich intermetallics in Al-Si-Cu 319 cast alloys at various Fe contents, cast samples with two different Fe contents (0.3 and 0.7%) were designed to cover the typical Fe content variation of the alloy in industrial products (0.15 to 1.0%). The standard Mn content in 319 cast alloys (0.25 %) was used in the present work, while the maximum Mo content of 0.4 % close to the liquid solubility of Mo

in aluminum with reasonable interval (0, 0.15% and 0.3%) was added to investigate the influence of individual Mo addition and combined additions of Mn and Mo on the phase precipitation of Fe-rich intermetallics.

For the casting, the materials were melted at 760 °C in a graphite crucible using an electrical resistance furnace. High-purity argon gas was used to minimize the hydrogen content in the melt for 15 min. Afterward, the liquid metal was poured into a permanent mould preheated at 250 °C to cast ingots. Thermal analysis (TA) was conducted with a small crucible filled with liquid metal to record the temperature changes during solidification. In some cases, the small crucible was quenched in water at a selected temperature to verify the formation of various Fe-rich intermetallics.

The specimens for the microstructural characterization were cut from the cast ingots and prepared with the traditional metallographic procedure. The evolution of the microstructures was examined and quantified using an optical microscope equipped with a Clemex image analyzer. For each sample, 50 fields were measured over the entire sample surface, and the area percentages of various Fe-rich intermetallics were obtained from the average measurement values. A scanning electron microscope (SEM; JEOL JSM-6480LV) equipped with an energy-dispersive X-ray spectroscope (EDS) and electron backscatter diffraction (EBSD) system was used to characterize the various Fe-rich intermetallics in the experimental alloys. Moreover, a differential scanning calorimetry (DSC; Perkin Elmer DSC 8000) was employed to identify and confirm the precipitation as well as the evolution of the Fe-rich intermetallics during the solidification with a heating rate of 10 °C /min.

Table 4.1 Chemical composition of the experimental alloys

Alloy	Si	Cu	Mg	Ti	Fe	Mo	Mn	Al
L0	5.35	3.19	0.08	0.10	0.28	0	0	Bal.
LM1	6.00	3.36	0.09	0.16	0.32	0.19	0	Bal.
LM2	6.02	3.42	0.09	0.14	0.31	0.32	0	Bal.
LM3	5.92	3.44	0.09	0.13	0.31	0.37	0	Bal.
H0	5.81	3.28	0.10	0.11	0.64	0	0	Bal.
HM1	6.00	3.35	0.09	0.12	0.67	0.18	0	Bal.
HM2	5.94	3.32	0.07	0.10	0.65	0.30	0	Bal.
HM3	5.89	3.41	0.11	0.10	0.70	0.41	0	Bal.
Mn1	6.18	3.4	0.09	0.12	0.66	0	0.25	Bal.
Mn2	6.04	3.39	0.10	0.11	0.68	0.15	0.25	Bal.
Mn3	6.18	3.46	0.09	0.14	0.69	0.30	0.26	Bal.
Mn4	6.02	3.52	0.09	0.17	0.66	0.41	0.24	Bal.

4.3 Results and Discussion

4.3.1 Precipitation of Fe-rich Intermetallics in experimental alloys

The typical microstructure of the experimental alloys consists of α-Al dendrites, eutectic Si, θ-Al_2Cu intermetallic, as well as various Fe-rich intermetallics with different morphologies. The typical Fe-rich intermetallics in this study are shown in Fig. 4.1 (indicated

by white arrows), and they can be first differentiated by two morphologies: a platelet morphology and a Chinese script shape. The Fe-rich intermetallics in Alloys H0 and L0 (Fig. 4.1a and Fig. 4.1b) have the platelet morphology, whereas they display the Chinese script shape in Alloy Mn1, LM2 and Mn3(Fig. 4.1c–Fig. 4.1e). The SEM-EDS analysis was applied to further distinguish these intermetallics (EDS results shows the average from values of at least ten similar intermetallics in the same alloy). It can be found the platelet Fe-rich intermetallics ("A" in Alloy H0 and "B" in Alloy L0) have the similar Si: Fe ratio, which is close to 1. Therefore, they are identified as β-Al_5FeSi (β-Fe) according to their platelet morphology and EDS results, which is in good agreement with the literature [31]. On the other hand, the Chinese script intermetallics ("C", "D" and "E") contain less Si and Fe but more Mn or/and Mo depending on the alloys. However, their (Fe + X (Mn, Mo)): Si ratio is similar to 1.5:1 (Table 2), indicating the similarity to the $Al_{15}(Fe,X)_3Si_2$ intermetallic, which is reported as α-Fe in literature [5].

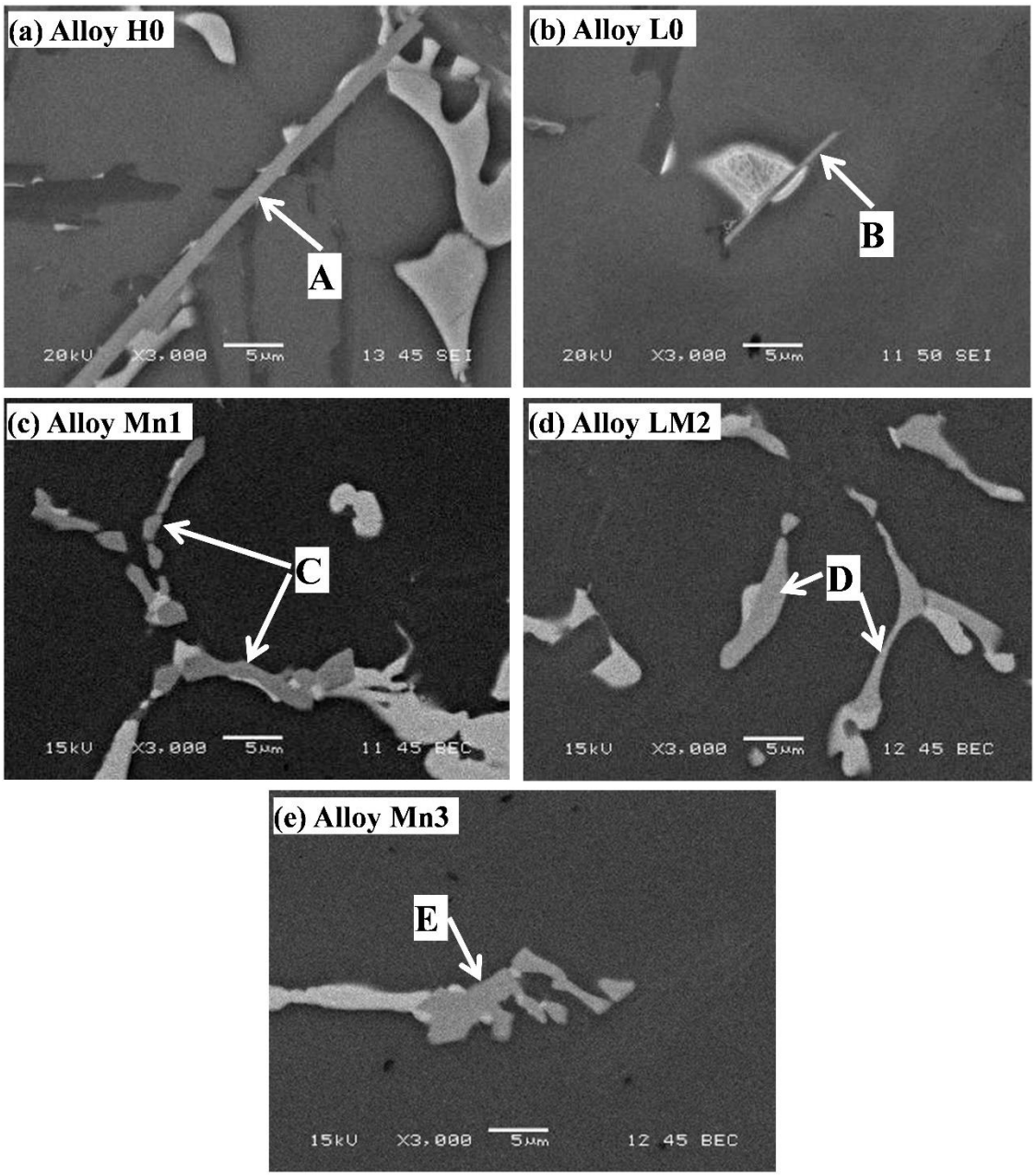

Fig. 4.1 Typical Fe-rich intermetallics (indicated by arrows) in: (a) Alloy H0, (b) Alloy L0, (c) Alloy Mn1, (d) Alloy LM2, and (e) Alloy Mn3.

Table 4.2 SEM-EDS results of the Fe-rich intermetallics shown in Fig. 4.1

Morphology	Phase	Elements (at. pct.)				
		Al	Si	Fe	Mn	Mo
Platelet	A	68.8±3.9	17.7±2.4	13.5±2.1	N/A	N/A
	B	67.0±2.6	17.7±1.4	15.0±0.9	N/A	N/A
Chinese Script	C	68.4±1.0	12.4±1.0	10.8±0.9	8.4±1.3	N/A
	D	69.1±3.1	12.9±1.7	10.2±1.4	N/A	7.8±1.3
	E	68.2±4.8	12.4±5.1	10.5±1.5	4.2±1.0	5.1±1.0

As shown in Fig. 4.1a and Fig. 4.1b, even with a similar platelet morphology, the disparities in size of platelet β-Fe are great; in particular, the length, which can reach 100 μm in Fig. 4.1a for Alloy H0 with high Fe content (0.7%), whereas it generally exhibits less than 30 μm in Fig. 4.1b for Alloy L0 with low Fe content (0.3%). The large difference in the size regarding β-Al_5FeSi in Alloys L0 and H0 suggests that they might be precipitated at different stages of the solidification process. Therefore, a TA was conducted for Alloys L0 and H0 and the results are shown in Fig. 4.2 together with the corresponding microstructure from the interrupted water quench test at 570 °C and 540°C. As shown in Fig. 4.2a and Fig. 4.2b, Peaks 1, 2, and 3 stand for the precipitations of α-Al dendrite, eutectic Si, and θ-Al_2Cu intermetallic, respectively, while Peaks 4 and 5 represent the precipitation of Fe-rich intermetallics [31]. In order to determine the corresponding phases of Peaks 4 and 5, interrupted water quench tests were performed at two distinctive temperatures: 570 °C (after Peak 4; dotted line I) and 540 °C (after Peak 5; dotted line II). The corresponding microstructures are shown in Fig. 4.2c–Fig. 4.2f. Evidently, no Fe-rich phase can be observed in Alloy L0 at 570 °C (Fig. 4.2c), whereas several long platelet β-Al_5FeSi phases appear in

Alloy H0 (indicated by black arrow in Fig. 4.2d), which implies that Peak 4 corresponds to the precipitation of the long platelet β-Al_5FeSi phase. Since the formation temperature of this kind β-Al_5FeSi is at approximately 580 °C, which is higher than that for eutectic Si (Peak 2 in Fig. 4.2b), these long platelet β-Al_5FeSi were then designated as P-β-Fe (pre-eutectic β-Al_5FeSi) in this study. For 540 °C (dotted line II), short and thin β-Al_5FeSi phases appear in the quenched microstructure in both L0 and H0 alloys (as indicated by white arrows in Fig. 4.2e and Fig. 4.2f) and they were designated as E-β-Fe (eutectic β-Al_5FeSi) due to their lower formation temperature. Obviously, the size of the P-β-Fe phase is much bigger than that of E-β-Fe. The smaller size of the E-β-Fe phase in Alloy L0 can be attributed to its phase precipitation at the lower temperature (approximately 560 °C). It should also be noted that, only a minor peak can be observed for E-β-Fe in Alloy H0, which can be attributed to the lower volume fraction of E-β-Fe compared to that of E-β-Fe in Alloy L0.

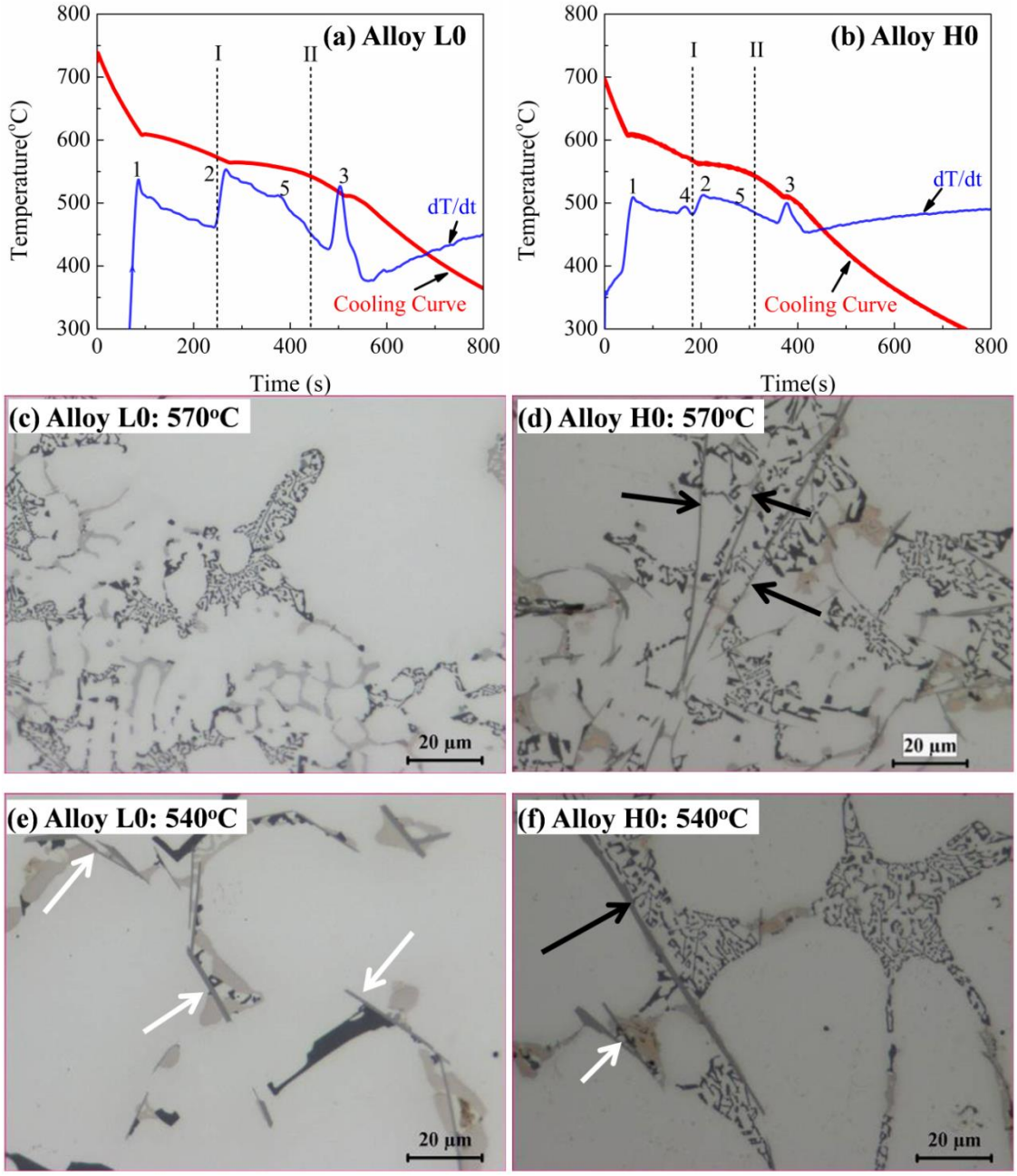

Fig. 4.2 TA curves of (a) Alloy L0 and (b) Alloy H0 as well as microstructure after interrupted water quench at: (c) 570 °C and (e) 540 °C of Alloy L0; (d) 570 °C and (f) 540 °C of Alloy H0

As shown in Table 4.2, the Chinese script Fe-rich intermetallics in Fig. 4.1c-1e are indicated as α-Fe in alloys with Mn and Mo additions based on their chemical compositions. However, different Chinese script α-Fe with similar chemical composition were reported in Al–Si–Cu alloys yet with different crystal structures, e.g., monoclinic Al_9Fe_2Si [32] and cubic

$Al_{15}(Mn,Fe)_3Si_2$ [33]. Therefore, for more accurate phase identification, EBSD was applied to further investigate these Chinese script intermetallics by comparing simulated EBSD pattern of individual Chinese script Fe-rich intermetallics with standard EBSD patterns of corresponding phases and their mean angular deviation (MAD) value. As an example, Fig. Fig. 4.3 shows the EBSD pattern and simulated results of the Chinese script phase "E" containing Mn and Mo in Alloy Mn3 (Table 4.2, Fig. 4.1 and Fig. 1e). It can be found that the pattern matches well with the standard pattern of the $Al_{15}(Fe,X)_3Si_2$-type crystal structure with the mean angular deviation (MAD) of 0.556, which is lower than the acceptable MAD value of 0.7 for the accurate phase identification [34]. Meanwhile, the average MAD value for the Chinese script phase in Fig. 4.1c and Fig. 4.1d are both lower than 0.7 (0.340 for "C" and 0.531 for "D"). The different MAD values of Chinese script phase in different alloys can be attributed to the lattice distortion due to the replacement between Fe, Mn and Mo atoms. Hence, all the Chinese script Fe-rich intermetallics in the present work were identified as cubic $Al_{15}(Fe,X)_3Si_2$ from combined results of EDS and EBSD. These Chinese script Fe-rich intermetallics were all designated indiscriminately as α-Fe though they might have slight variation in their chemical compositions due to the different Mn and Mo additions in experimental alloys.

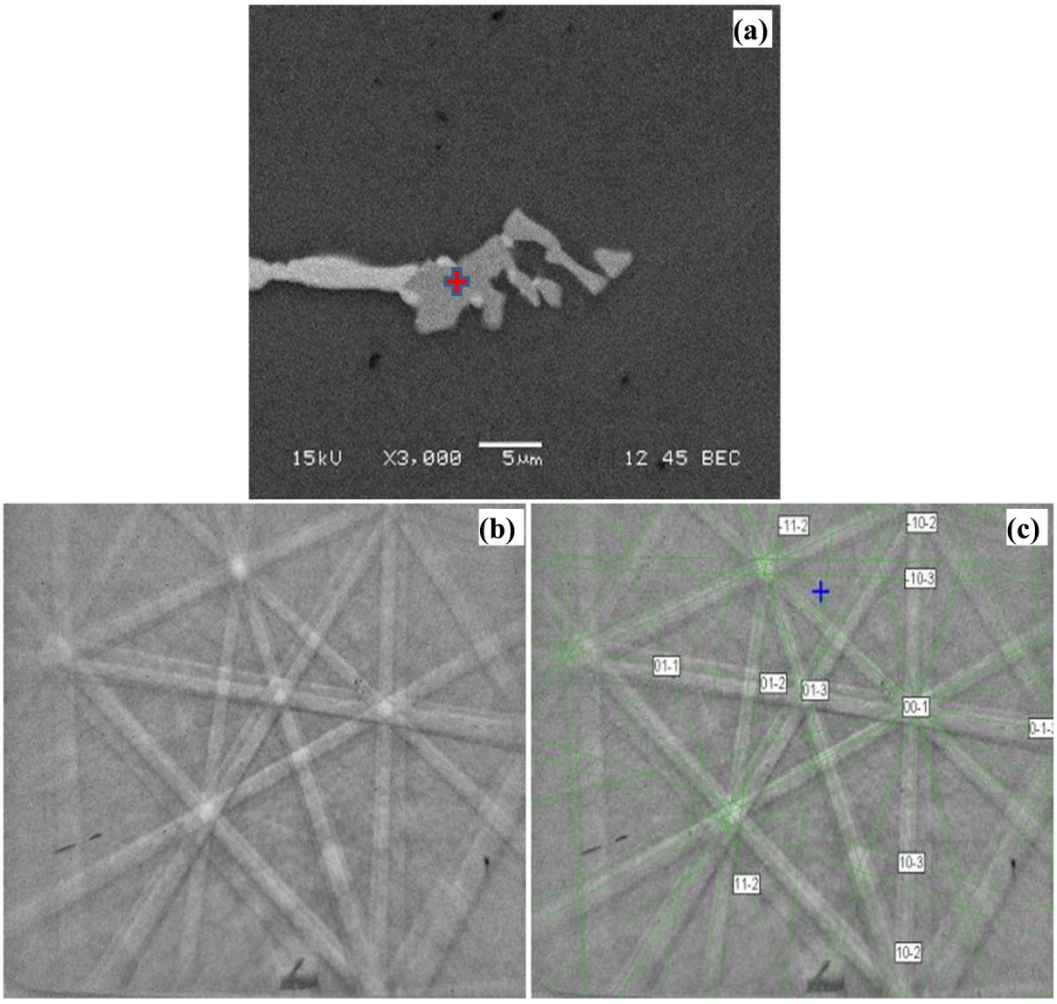

Fig. 4.3 Chinese Script Fe-rich intermetallic in Alloy Mn3 (a) and its EBSD pattern (b) as well as the simulation results (c)

Fig. 4.4 shows the TA curves of Alloys LM3 and HM3 together with the corresponding microstructure from the interrupted water quench test at 580 °C. Compared with H0 in Fig. 4.3, a new peak occurs (Peak 6) at 590 °C for Alloy LM3 (Fig. 4.4a) and Alloy HM3 (Fig. 4.4b). Fig. 4.4c and Fig. 4.4d present the microstructures from the interrupted water quench test after Peak 6 for 580 °C (indicated by dotted line). Chinese script α-Fe (indicated by black arrows) are the dominant Fe-rich intermetallics in both Alloy LM3 (Fig. 4.4c) and Alloy HM3 (Fig. 4.4d), thereby confirming the precipitation of α-Fe at Peak 6. It should also be noted that the peak intensity of Alloy LM3 is lower than that of Alloy HM3, which can be derived from their lower volume fraction in Alloy LM3.

Based on the metallographic observations and results obtained from TA in our work together with some previous studies [35, 36], Table 4.3 summarizes the various Fe-rich intermetallics formed in the investigated alloys. It can be found that the type of Fe-rich intermetallic strongly dependent on the alloy compositions. For instance, E-β-Fe is present in all alloys except LM3 and Mn4 while P-β-Fe can only exist for alloys with higher Fe contents (0.7%), whereas α-Fe is almost ubiquitous except for Alloy H0.

Table 4.3 Formation of Fe-rich intermetallics in experimental alloys

Peak	Phases	Alloys
4	P-β-Fe	H0, HM1, HM2, Mn1, Mn2, Mn3
5	E-β-Fe	All alloys except LM3, Mn4
6	α-Fe	All alloys except H0

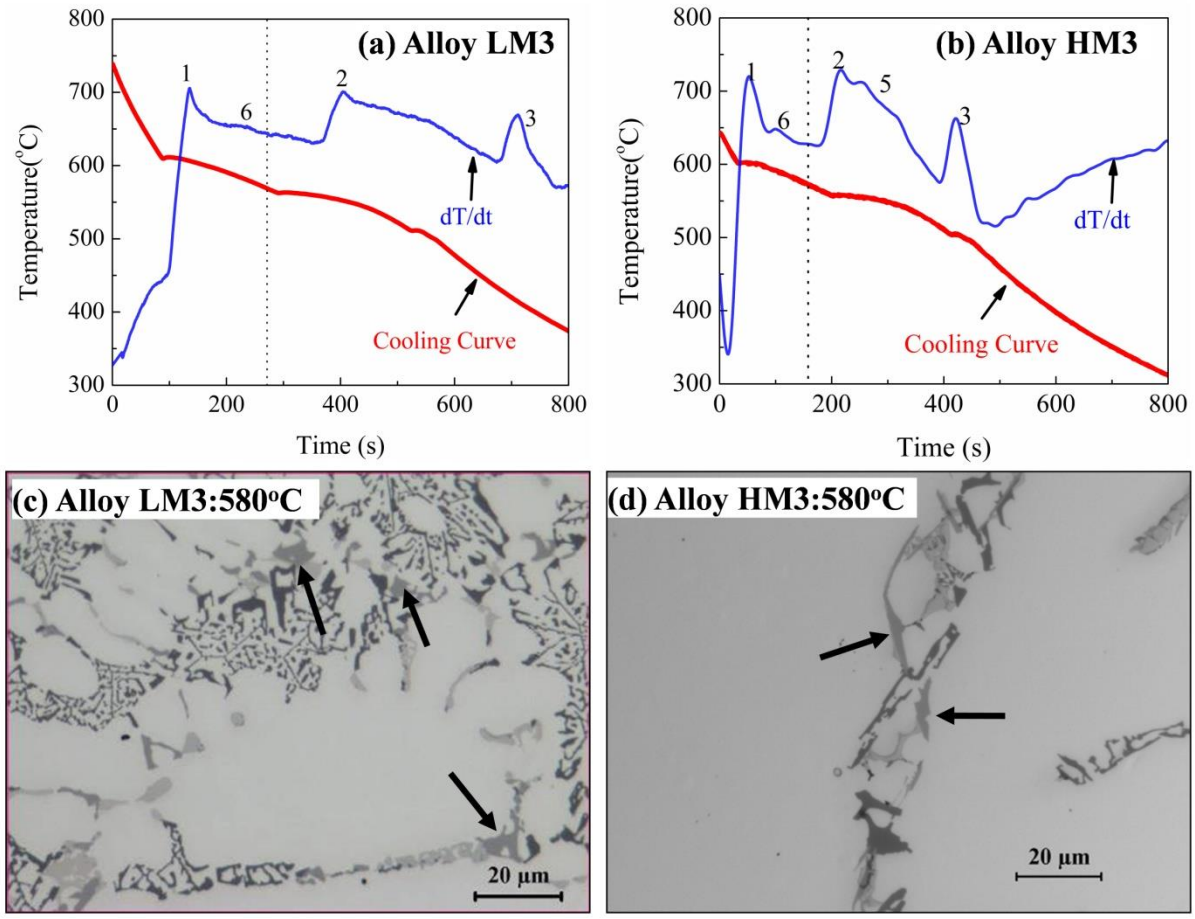

Fig. 4.4 TA curves of alloys: (a) LM3 and (b) HM3 and microstructure after interrupted water quench at 580 ºC of (c) LM3 and (d) HM3 alloys (black arrows indicate α-Fe)

4.3.2 Evolution of Fe-rich intermetallics with Mo and Mn additions

As shown in Table 4.3, various Fe-rich intermetallics exist in the different alloys with various combinations of Fe, Mo, and Mn contents. Even for same Fe content, the existing Fe-rich intermetallics can change depending on the Mo contents, thereby indicating a possible preferential phase selection and competition of Fe-rich intermetallics under different chemical compositions. Therefore, alloys with various Mo and Fe contents were examined and the microstructures are presented in Fig. 4.5.

Regarding the alloys with low Fe content (0.3%), Alloy L0 without Mo (Fig. 4.5a), considerable numbers of E-β-Fe phases (indicated by white arrow) dominate the

microstructure. After only 0.15% Mo addition (Fig. 4.5b), the E-β-Fe phases partially disappear, as reflected by their smaller sizes and decreasing volumes. It is noteworthy that some α-Fe phases (indicated by thick black arrow) start to form in Alloy LM1 compared to negligible amounts of α-Fe phases in Alloy L0 in Fig. 4.5a and their volume fraction increases with increasing Mo content. After the addition of 0.37% Mo in Alloy LM3 (Fig. 4.5c), the amount of the E-β-Fe phase significantly decreases to an almost unnoticeable amount, whereas the amount of the α-Fe phases increases significantly until α-Fe becomes the sole Fe-rich intermetallic in Alloy LM3.

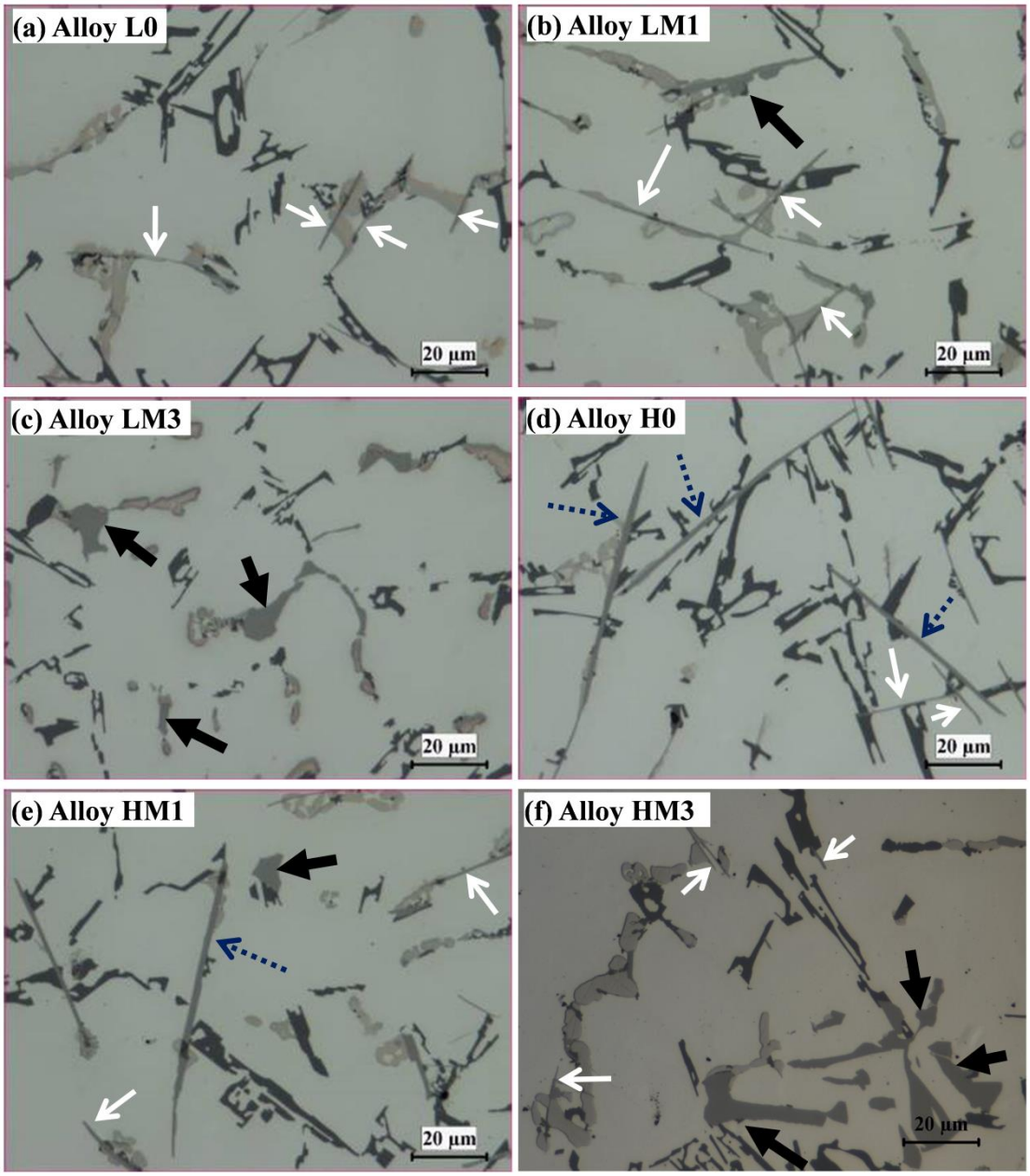

Fig. 4.5 Optical micrographs showing effect of Mo on microstructure for low-Fe (0.3%) alloys: (a) L0, (b) LM1, and (c) LM3; for high-Fe (0.7%) alloys: (d) H0, (e) HM1, and (f) HM3 (white, blue dotted and black arrows indicate E-β-Fe, P-β-Fe, and α-Fe, respectively)

In Alloy H0 (high Fe content but free of Mo; Fig. 4.5d), a considerable number of P-β-Fe (indicated by blue dotted arrow) and E-β-Fe phases (indicated by white arrow) coexist. After the addition of 0.15% Mo in Alloy HM1 (Fig. 4.5e), P-β-Fe was partially suppressed

but a relatively high volume of E-β-Fe can still be observed. Further, for the addition of up to 0.41% Mo (Alloy HM3; Fig. 4.5f), the volume of the P-β-Fe phase significantly decreases to an approximately unnoticeable volume, whereas E-β-Fe phases are still visible in the microstructure. Besides, α-Fe phase begins to form for an addition of 0.15% Mo (indicated by white arrow) in Fig. 4.5e and its amount also increases with increasing Mo content (Fig. 4.5e–Fig. 4.5f). Apparently, approximately all E-β-Fe phases are suppressed and microstructure with dominant α-Fe is obtained with a sufficient Mo addition in alloys with lower Fe content (0.3%), such as LM3 in Fig. 4.5c. For alloys with high Fe content (0.7%), although Mo addition also promotes the formation of Chinese Script α-Fe phases. However, even with 0.41% Mo addition, the E-β-Fe is not completely suppressed, this is likely due to the high-Fe content consume more Mo to suppress the formation of P-β-Fe, leaving limited amount of Mo to further suppress the formation of E-β-Fe. The possible reasons for the phase suppression and selection will be discussed later in this section.

Fig. 4.6 shows the quantified analysis results of area fractions of various Fe-rich intermetallics. Generally, the total area fractions of the Fe-rich intermetallics are similar in alloys with same Fe content while the total area fractions increase with increasing Fe content. As shown in Fig. 4.6a and Fig. 4.6b, the total area fractions of Fe-rich intermetallics in alloys with low Fe content (0.3%) remain at approximately 1.15% (Fig. 4.6a) and increase to approximately 2.05% in alloys with high Fe content (0.7%) (Fig. 4.6b). For the individual Fe-rich intermetallics, the area fraction of α-Fe increases with increasing Mo addition while the evolutions of P-β-Fe and E-β-Fe are different in both low Fe and high Fe alloys. As in low Fe alloy (Fig. 4.6a), the proportion of α-Fe in the total intermetallic fraction increases from 0 in Alloy L0 to 20.7% and 41.9% in alloys LM1 and LM2, respectively, until it reaches 100% in Alloy LM3 without E-β-Fe. Regarding the alloys with high Fe content (Fig. 4.6b), the proportion of α-Fe in the total intermetallic fraction increases from 0 (Alloy H0) to 15.8% (Alloy HM1), 57.9% (Alloy HM2), and 78.9% (Alloy HM3) with increasing Mo additions. However, a moderate amount of E-β-Fe remains. By contrast, the P-β-Fe phase completely disappears for the maximum Mo addition of 0.41% (Fig. 4.6b).

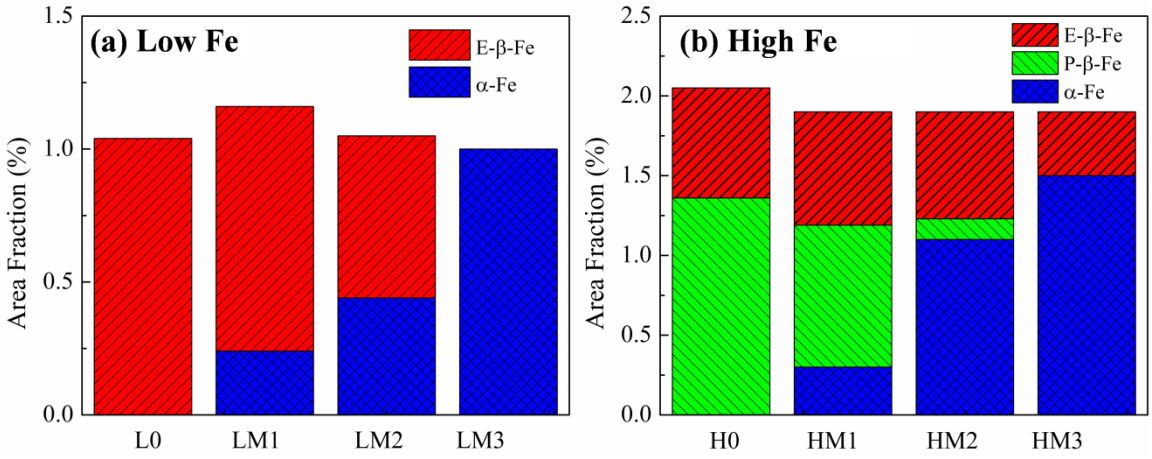

Fig. 4.6 Area fractions of α-Fe, P-β-Fe, and E-β-Fe for different Mo additions in (a) Low Fe alloy, (b) High Fe alloy.

As shown in Fig. 4.5 and Fig. 4.6, the Mo addition can significantly promote the formation of Chinese script α-Fe while inhibit the precipitation of E-β-Fe at low Fe content (0.3%) and P-β-Fe at high Fe content (0.7%). It is reported that the Mn addition can increase the formation temperature of α-Fe but decrease that of β-Fe in Al-Cu 206 cast alloys [37], explaining the promoting effect of Mn on Chinese script Fe-rich intermetallics. Therefore, it is also to be expected that Mo addition can have similar influence on the formation temperature of various Fe-rich intermetallics in our study, leading to evolution of Fe-rich intermetallics shown in Fig. 4.5 and Fig. 4.6. Therefore, the DSC was employed in present work in order to investigate the effect of the Mo addition on the evolution of various Fe-rich intermetallics and results are shown in Fig. 4.7. Regarding the alloys with low Fe content (0.3%) in Fig. 4.7a, Peak 5 (corresponding to E-β-Fe) significantly decreases with increasing Mo addition and it nearly disappears for 0.37% Mo addition in Alloy LM3. This is in a good agreement with the area fraction results (Fig. 4.6a) and study [13]. Fig. 4.7c presents the enlarged zone of Peak 5 in Fig. 4.7a. The decreasing peak area with increasing Mo content confirms the decreasing volume fraction of E-β-Fe. Moreover, the formation temperature of E-β-Fe shifts to lower temperature with increasing Mo addition, thereby indicating the

suppression of E-β-Fe formation via Mo addition.

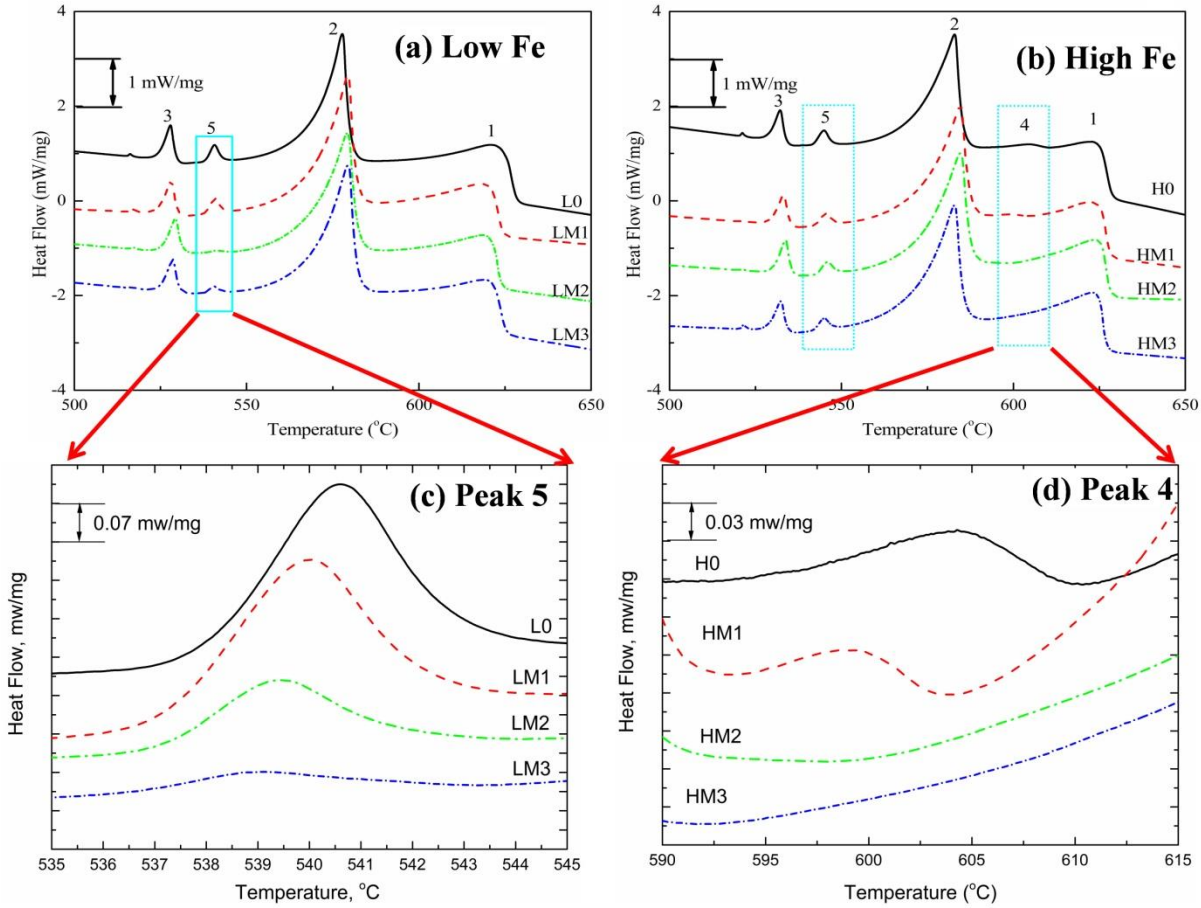

Fig. 4.7 DSC heating curves of (a) low-Fe alloys, (b) high-Fe alloys and (c) enlarged zone 5 in (a) while (d) enlarged zone 4 in (b)

For alloys with high Fe content (0.7%) in Fig. 4.7b, Peak 4 (corresponding to P-β-Fe) decreases with increasing Mo additions, confirming the hindering effect of Mo on the formation of P-β-Fe intermetallics, whereas Peak 5 (corresponding to E-β-Fe) displays no significant changes even for 0.41% Mo addition in Alloy HM3. Fig. 4.7d shows the enlarged Peak 4 (P-β-Fe) in high Fe content (0.7%) alloys, it is evident that the peak intensity and precipitation temperature of the P-β-Fe phases decrease with increasing Mo contents, confirming that the P-β-Fe precipitation is also suppressed by the Mo addition. Thus, the peak intensity and formation temperature of both E-β-Fe in low Fe content and P-β-Fe in high Fe content decrease with increasing Mo addition, confirming the hindering effect of Mo on the

formation of β-Fe phase. The disappearance of the platelet E-β-Fe/P-β-Fe phases with increasing Mo addition can be attributed to their different formation temperatures during solidification. As shown in Fig. 4.3 and Fig. 4.4, the formation temperature increases from E-β-Fe, P-β-Fe, to α-Fe. When Mo is added, Mo first interacts with Al, Fe, and Si to precipitate α-Fe before the precipitation of P-β-Fe and E-β-Fe, leaving less Fe available for the formation of P-β-Fe/E-β-Fe and thus decreasing their volume fractions.

Owing to the limited solubility of Mo in Al alloys [37], a further increase in the Mo addition results in the formation of a primary Al-Mo intermetallic component during solidification and limited its further influence on the Fe-rich intermetallics [38]. On the other hand, Mn was reported to be effective in neutralizing the platelet β-Fe, especially the eutectic β-Fe [13]. Hence, the combined addition of Mn and Mo was also investigated for the alloys with high Fe content (0.7%) to completely suppress the formation of platelet β-Fe phases and the evolutions of the microstructures are presented in Fig. 4.8.

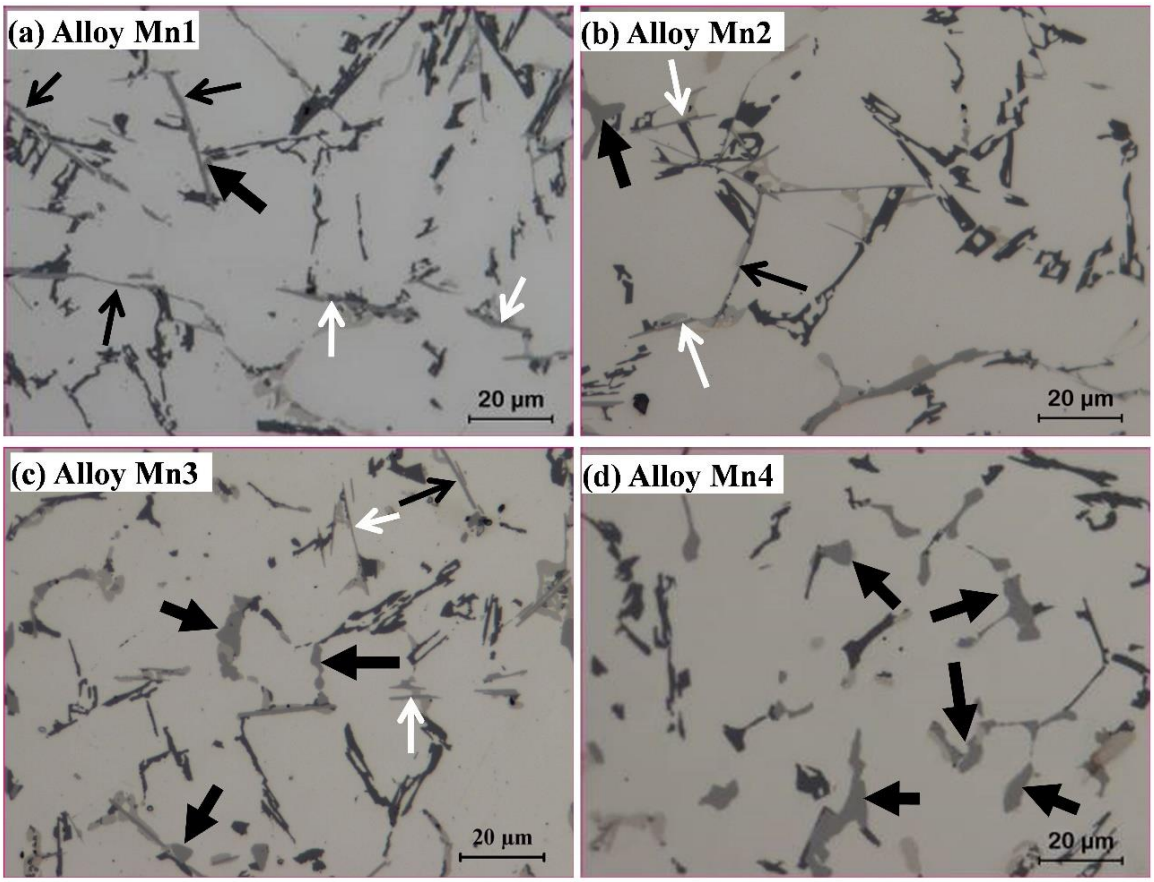

Fig. 4.8 Optical images of alloys: (a) Mn1, (b) Mn2, (c) Mn3, and (d) Mn4 (white, black, and thick black arrows indicate E-β-Fe, P-β-Fe, and α-Fe, respectively)

In Alloy Mn1 (Fig. 4.8a), a small amount of α-Fe (indicated by thick black arrows) co-exist with P-β-Fe (thin black arrows) and E-β-Fe (white arrows), indicating the positive effect of Mn on α-Fe intermetallics compared with Alloy H0 with only P-β-Fe and E-β-Fe (Fig. 4.5d). For the combined addition of Mn and Mo (Fig. 4.8b and Fig. 4.8c), the area fraction of both P-β-Fe and E-β-Fe decreases while that of α-Fe increases; In particular, in Alloy Mn4 with 0.41% Mo and 0.24% Mn, both P-β-Fe and E-β-Fe disappear completely, leaving α-Fe as the sole Fe-rich intermetallic (Fig. 4.8d), indicating the complete suppression of β-Fe due to the combined Mn and Mo additions.

The evolutions of the area fractions of α-Fe, P-β-Fe, and E-β-Fe intermetallics in the alloys containing Mn and Mo are presented in Fig. 4.9. With increasing Mo addition in the

presence of Mn, area fraction of both P-β-Fe and E-β-Fe decreases, while that of α-Fe increases significantly. For the combined addition of 0.24% Mn and 0.41% Mo (Alloy Mn4), β-Fe is completely suppressed, and a unique α-Fe dominated microstructure is achieved in the high Fe content alloys.

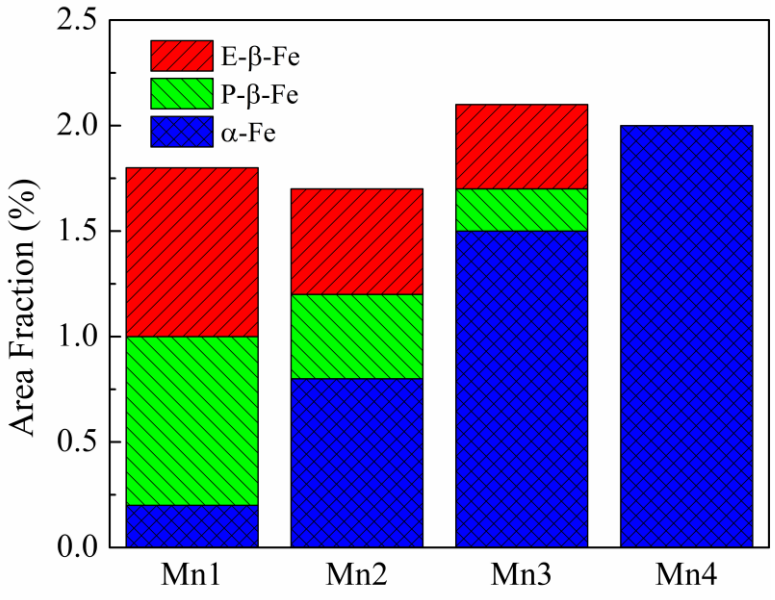

Fig. 4.9 Area fractions of α-Fe, P-β-Fe, and E-β-Fe in experimental alloys

According to the evolution of Fe-rich intermetallics with equal Fe contents presented in Fig. 4.9 and Fig. 4.6b, it can be inferred that Mo exhibits a stronger effect than Mn on the promotion of α-Fe precipitation. For instance, there is an 0.2% area fraction of α-Fe in Alloy Mn1 (0.25% Mn), whereas the area fraction of α-Fe reaches 1.1% in Alloy HM2 (0.3% Mo). Al-Si-Cu 319 cast alloy is generally secondary alloy with higher Fe content, the necessity to efficiently reduce Fe content is often prioritized in industrial practice. Thus, the effect of Mn and Mo in suppressing P-β-Fe and promoting α–Fe is compared, and the correlation of Mo/Mn contents and area fractions of the P-β-Fe/α-Fe phases was established on the calculated area fractions from Fig. 4.6 and Fig. 4.9 in high Fe content (0.7%) alloys and presented in Fig. 4.10.

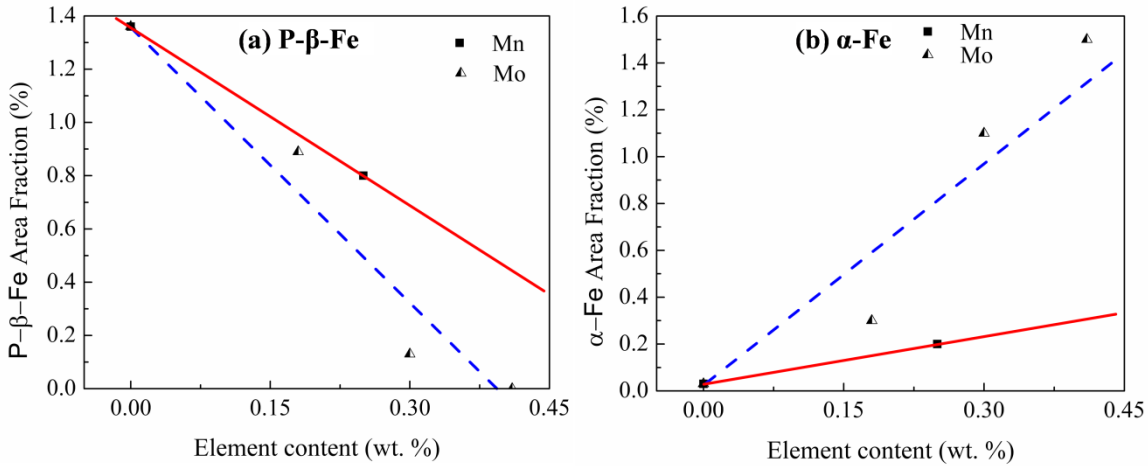

Fig. 4.10 Correlation between Mo and Mn contents with area fractions of (a) P-β-Fe and (b) α-Fe in alloys with high Fe contents (0.7%)

As shown in Fig. 4.10a, the relative area fraction of the P-β-Fe phase decreases with increasing Mo and Mn additions. However, the decreasing rate due to the Mo addition is much larger than that caused by Mn, thereby indicating a stronger suppressing influence of Mo on P-β-Fe. Similarly, as presented in Fig. 4.10b, α-Fe generally increases with increasing Mo and Mn contents but the slope due to the Mo addition is much larger than that due to Mn, confirming the stronger effect of Mo on the promotion of α-Fe formation. Therefore, Mo can be more efficient than Mn on suppressing platelet β-Fe and promoting α-Fe from this point of view. However, the solubility of Mo in Al is relatively lower compared with Mn [38]. Thus, combined addition of Mo and Mn is recommended in order to obtain the complete suppression of platelet Fe-rich intermetallics in Al-Si-Cu 319 cast alloys, especially for high Fe contents in industrial applications.

4.4 Conclusions

The formation of Fe-rich intermetallics in Al–Si–Cu 319 cast alloys with various Fe, Mo, and Mn contents was studied in the present work with the following conclusions:

(1) Two types of platelet Fe-rich intermetallics, defined as eutectic and pre-eutectic β-Fe, and one type of α-Fe can precipitate depending on the Fe, Mo, and Mn contents. Without the

Mn/Mo additions, only eutectic β-Fe form in the low-Fe alloys (0.3%), whereas pre-eutectic and eutectic β-Fe coexist in the high-Fe alloys (0.7%).

(2) The addition of Mo can strongly promote the formation of α-Fe and suppress the precipitation of β-Fe in both low-Fe and high-Fe alloy. However, the effect of Mo on the suppression of β-Fe is greatly related to the Fe contents. In low-Fe alloys, the addition of 0.37% Mo can completely suppress eutectic β-Fe. While, only pre-eutectic β-Fe can be reduced with increasing Mo content, leaving the eutectic β-Fe intermetallics almost unchanged in high-Fe alloys.

(3) Both pre-eutectic β-Fe and eutectic β-Fe can be completely suppressed, and a unique α-Fe microstructure can be achieved with a combined addition of Mn (0.24%) and Mo (0.41%) in high-Fe alloys.

(4) Compared with Mn, Mo exhibits a stronger effect in promoting α-Fe precipitation. The combined addition of Mn and Mo can achieve a better modification of both pre-eutectic β-Fe and eutectic β-Fe intermetallics in industrial 319 cast alloys.

References

[1] F.J. Tavitas-Medrano, A.M.A. Mohamed, J.E. Gruzleski, F.H. Samuel, H.W. Doty, Precipitation-hardening in cast AL-Si-Cu-Mg alloys, Journal of Materials Science 45(3) (2010) 641-651.

[2] M. Javidani, D. Larouche, Application of cast Al-Si alloys in internal combustion engine components, International Materials Reviews 59(3) (2014) 132-158.

[3] B.P. Bhardwaj, The Complete Book on Production of Automobile Components & Allied Products, 2014.

[4] P. Crepeau, Effect of Iron in Al-Si Casting Alloys: A Critical Review (95-110), Transactions of the American Foundrymen's Society 103 (1995) 361-366.

[5] N.A. Belov, A.A. Aksenov, D.G. Eskin, Iron in Aluminium Alloys: Impurity and Alloying Element, Taylor & Francis2002.

[6] M.V. Glazoff, V.S. Zolotorevsky, N.A. Belov, Casting Aluminum Alloys, Elsevier Science2010.

[7] V. Rivlin, G. Raynor, 4: Critical evaluation of constitution of aluminium-iran-silicon system, International Metals Reviews 26(1) (1981) 133-152.

[8] S.P. Gupta, Intermetallic compound formation in Fe–Al–Si ternary system: Part I, Materials Characterization 49(4) (2002) 269-291.

[9] T. Maitra, S.P. Gupta, Intermetallic compound formation in Fe–Al–Si ternary system: Part II, Materials Characterization 49(4) (2002) 293-311.

[10] N. Krendelsberger, F. Weitzer, J.C. Schuster, On the reaction scheme and liquidus surface in the ternary system Al-Fe-Si, Metallurgical and Materials Transactions A 38(8) (2007) 1681-1691.

[11] K. Liu, X. Cao, X.-G. Chen, Formation and Phase Selection of Iron-Rich Intermetallics in Al-4.6Cu-0.5Fe Cast Alloys, Metallurgical and Materials Transactions A 44(2) (2013) 682-695.

[12] K. Liu, X. Cao, X.-G. Chen, Solidification of Iron-Rich Intermetallic Phases in

Al-4.5Cu-0.3Fe Cast Alloy, Metallurgical and Materials Transactions A 42(7) (2011) 2004-2016.

[13] N.A. Belov, D.G. Eskin, A.A. Aksenov, Multicomponent phase diagrams: applications for commercial aluminum alloys, Elsevier2005.

[14] J.Y. Hwang, H.W. Doty, M.J. Kaufman, The effects of Mn additions on the microstructure and mechanical properties of Al–Si–Cu casting alloys, Materials Science and Engineering: A 488(1–2) (2008) 496-504.

[15] J.A. Taylor, G.B. Schaffer, D.H. StJohn, The role of iron in the formation of porosity in Al-Si-Cu-based casting alloys: Part III. A microstructural model, Metallurgical and Materials Transactions A 30(6) (1999) 1657-1662.

[16] J.A. Taylor, The effect of iron in Al-Si casting alloys, 35th Australian Foundry Institute National Conference, Australian Foundry Institute (AFI), 2004, pp. 148-157.

[17] K. Liu, X. Cao, X.-G. Chen, Tensile Properties of Al-Cu 206 Cast Alloys with Various Iron Contents, Metallurgical and Materials Transactions A 45(5) (2014) 2498-2507.

[18] J. Iglessis, C. Frantz, M. Gantois, Conditions de formation des phases de fer dans les alliages Al-Si de pureté commerciale, Mémoires scientifiques de la revue de métallurgie 73(4) (1977) 237-242.

[19] S. Belmares-Perales, M. Castro-Román, M. Herrera-Trejo, L.E. Ramírez-Vidaurri, Effect of cooling rate and Fe/Mn weight ratio on volume fractions of α-AlFeSi and β-AlFeSi phases in Al-7.3Si-3.5Cu alloy, Metals and Materials International 14(3) (2008) 307-314.

[20] Y. Awano, Y. Shimizu, Non-equilibrium crystallization of alfesi compound in melt-superheated Al-Si alloy castings, AFS Transactions 98 (1990) 889-895.

[21] H.Y. Kim, S.W. Han, H.M. Lee, The influence of Mn and Cr on the tensile properties of A356–0.20Fe alloy, Materials Letters 60(15) (2006) 1880-1883.

[22] M. Mahta, M. Emamy, A. Daman, A. Keyvani, J. Campbell, Precipitation of Fe rich intermetallics in Cr-and Co-modified A413 alloy, International Journal of Cast Metals Research (2013).

[23] S.S. Kumari, R. Pillai, B. Pai, A study on the structural, age hardening and mechanical

characteristics of Mn and Ca added Al–7Si–0.3 Mg–0.6 Fe alloy, Journal of Alloys and Compounds 453(1) (2008) 167-173.

[24] F. Samuel, A. Samuel, H. Doty, Factors Controlling the Type and Morphology of Cu-Containing Phases in 319 Al Alloy (96-30), Transactions of the American Foundrymen's Society 104 (1996) 893-902.

[25] S. Seifeddine, S. Johansson, I.L. Svensson, The influence of cooling rate and manganese content on the β-Al_5FeSi phase formation and mechanical properties of Al–Si-based alloys, Materials Science and Engineering: A 490(1–2) (2008) 385-390.

[26] M. Javidani, D. Larouche, X. Grant Chen, Assessment of Post-eutectic Reactions in Multicomponent Al-Si Foundry Alloys Containing Cu, Mg, and Fe, Metallurgical and Materials Transactions A 46(7) (2015) 2933-2946.

[27] A.M. Samuel, J. Gauthier, F.H. Samuel, Microstructural aspects of the dissolution and melting of Al_2Cu phase in Al-Si alloys during solution heat treatment, Metallurgical and Materials Transactions A 27(7) (1996) 1785-1798.

[28] C.G. McKamey, J.A. Horton, The effect of molybdenum addition on properties of iron aluminides, Metallurgical Transactions A 20(4) (1989) 751-757.

[29] A.R. Farkoosh, X.G. Chen, M. Pekguleryuz, Dispersoid strengthening of a high temperature Al-Si-Cu-Mg alloy via Mo addition, Materials Science and Engineering: A 620 (2015) 181-189.

[30] A.R. Farkoosh, X. Grant Chen, M. Pekguleryuz, Interaction between molybdenum and manganese to form effective dispersoids in an Al-Si-Cu-Mg alloy and their influence on creep resistance, Materials Science and Engineering: A 627 (2015) 127-138.

[31] L.A. Narayanan, F.H. Samuel, J.E. Gruzleski, Crystallization behavior of iron-containing intermetallic compounds in 319 aluminum alloy, Metallurgical and Materials Transactions A 25(8) (1994) 1761-1773.

[32] J.M. Sanchez, I. Vicario, J. Albizuri, T. Guraya, N.E. Koval, J.C. Garcia, Compound Formation and Microstructure of As-Cast High Entropy Aluminums, Metals 8(3) (2018) 167.

[33] A. Couture, Iron in Aluminum Casting Alloys - a Literature Survey, International Cast

Metals Journal 6(4) (1981) 9-17.

[34] M.V. Kral, H.R. McIntyre, M.J. Smillie, Identification of intermetallic phases in a eutectic Al–Si casting alloy using electron backscatter diffraction pattern analysis, Scripta Materialia 51(3) (2004) 215-219.

[35] E.A. Elsharkawi, E. Samuel, A.M. Samuel, F.H. Samuel, Effects of Mg, Fe, Be additions and solution heat treatment on the π-AlMgFeSi iron intermetallic phase in Al-7Si-Mg alloys, Journal of Materials Science 45(6) (2010) 1528-1539.

[36] V.S. Zolotorevsky, N.A. Belov, M.V. Glazoff, Casting Aluminum Alloys, Elsevier Science2010.

[37] K. Liu, X. Cao, X.-G. Chen, Effect of Mn, Si, and cooling rate on the formation of Iron-rich intermetallics in 206 Al-Cu cast alloys, Metallurgical and Materials Transactions B 43(5) (2012) 1231-1240.

[38] K. Liu, H. Ma, X.G. Chen, Enhanced elevated-temperature properties via Mo addition in Al-Mn-Mg 3004 alloy, Journal of Alloys and Compounds 694 (2017) 354-365.

Chapter 5 Evolution of dispersoids and their effect on elevated-temperature mechanical properties and creep resistance in Al–Si–Cu 319 cast alloys with Mo and Mn additions

Abstract

In the present work, the effects of Mo and Mn additions on the evolution of dispersoids during various heat treatment conditions were investigated in Al-Si-Cu-Mg 319 cast alloys. Besides, their effects on yield strength and creep resistance at elevated temperature (300 ^{o}C) were also studied. The results showed that Mo or/and Mn can greatly improve the precipitation of the dispersoids during proper heat treatment while 500°C /8h was found to be the optimal heat treatment condition characterized with the largest quantity and the finest α-dispersoids, leading to the remarkable improved YS at both room temperature and 300 ^{o}C. Meanwhile, the creep resistance at 300 °C was also greatly enhanced due to the Mn and Mo additions, with doubled higher threshold stress (from 10.6 to 22.8 MPa) and 50 times lower minimum creep rate (from 5.5E-7 s^{-1} to 1.1E-8 s^{-1}). Though the properties are worsened during the service time at 300 °C, the decreasing extent of properties is much slower in alloys with Mn or/and Mo additions due to the presence of dispersoids, which is 10% on YS and 5% on the maximum creep strain in alloys with combined additions of Mn and Mo compared with 47% and 24% in alloys free of Mn or Mo, respectively, showing the superior thermal stability of Al-Si-Cu 319 alloys with Mn and Mo additions and thus widening their application at elevated temperature.

5.1 Introduction

Heat-treatable Al-Si cast alloys have been widely industrial used, especially in auto industries, such as engine blocks and cylinder heads, because of their good

castability and relatively moderate strength [1-3]. During the service of these parts, their temperature could easily reach to elevated temperature (ET) range of 250-350^{o}C. However, the nano-scale precipitates formed during heat treatment can be rapidly coarsened at ET, leading to the sharply decrease of the mechanical properties [4]. Therefore, dispersoid strengthening has been employed to improve the elevated-temperature properties in both cast aluminum alloys [5-7] and wrought aluminum alloys [8-11], by modifying the alloying elements to promote the precipitation of thermally stable dispersoids after proper precipitation treatments, which can act as the effective hinder points for the movement of dislocation.

According to literature [12], low diffusivity and low solid solubility in Al are two important criteria in selecting alloying elements to form the effective thermally stable dispersoids. Numerous studies [6, 13-15] have been performed to study the effect of different alloying elements on inducing thermally stable dispersoids to improve their elevated-temperature strength. Among these elements, Mn has attracted more attention. During heat treatment, the supersaturated solid solution of Mn decomposes, leading to the precipitation of high volume of thermal stable α-Al(Mn,Fe)Si dispersoids during the precipitation treatment [16, 17]. Liu *et al.* [17] focused on effect of heat treatment on the evolution of dispersoids and claimed that precipitation of α-Al(Mn,Fe)Si dispersoids starts at approximately 340 °C and maximum volume fraction can reach at 3% after 375 °C /48h in 3xxx alloy while the dispersoids start to coarsen even dissolve into matrix with further increasing temperatures. The α-Al(Mn,Fe)Si dispersoids are confirmed to be partially coherent with the matrix and have a cubic crystal structure [18]. Besides, α-Al(Mn,Fe)Si dispersoids are proven to be thermally stable at 300 °C, resulting in the excellent mechanical properties and creep resistance at elevated temperatures [17].

As another transition element, Mo is one of the most often alloyed elements to improve the elevated-temperature properties due to its low diffusivity (2.3×10^{-26} m^2s^{-1} at 300 °C) and limited solid solubility in Al (~0.25 wt.% at peritectic temperature, 660

°C) [5]. Farkoosh *et al.* [5] found that Mo can promote α-Al(Mo,Fe)Si dispersoids upon 540 °C solution treatment in Al-Si 356 cast alloy, leading to the improved YS and creep resistance. On the other hand, Liu *et al.* [19] claimed that with 0.3 wt.% Mo, 3004 alloy precipitates a large volume fraction of fine α-Al(Mn,Mo,Fe)Si dispersoids upon heat treated at 350-420 °C, and remarkable improved in yield strength and creep resistance was also obtained.

From the above-mentioned literatures [5, 19], it can be found that precipitation behavior of dispersoids with Mo additions varies with alloys and necessitates more systematic studies, such as the optimized precipitation temperature and the role of combined addition of Mn and Mo compared with the individual addition of Mn or Mo on the evolution of mechanical properties. On the other hand, limited research has been performed regarding the effect of Mo and Mn additions on elevated-temperature properties in Al-Si-Cu-Mg 319 cast alloys, especially the creep resistance. Therefore, the effects of Mn and Mo in 319 cast alloys on the microstructure and elevated-temperature mechanical properties were investigated systematically in the present study. The evolution of dispersoids during various heat treatments was investigated while the YS and creep resistance at 300 °C were analyzed systematically. In addition, the evolution of properties during the service time at 300 °C was also evaluated in alloys with different additions of Mn or/and Mo.

5.2 Materials and Methods

Four 319-type alloys with different Mo and Mn contents were designed in present work, in which Alloy A is the base alloy free of Mn or Mo while Alloys B and C are individual addition of Mn, Mo and Alloy D is with combined Mn and Mo additions. The chemical compositions analyzed with optical emission spectrometer were presented in Table 5.1. All the alloy compositions in present work are in wt. % unless otherwise indicated.

Table 5.1 Chemical compositions of the experimental alloys (wt.%).

Alloy	Si	Cu	Mg	Ti	Fe	Mo	Mn	Al
A(Base)	5.99	3.19	0.08	0.10	0.28	0	0	Bal.
B	6.03	3.42	0.08	0.10	0.22	0	0.24	Bal.
C	6.02	3.42	0.09	0.14	0.31	0.32	0	Bal.
D	6.07	3.45	0.09	0.08	0.32	0.29	0.25	Bal.

The experimental alloys were prepared in an electric resistance furnace. The temperature of the melt was maintained at 750 °C for 30 minutes followed by the degassing process for 15 minutes. Then, the melt was poured and solidified in a permanent mould preheated at 250 °C to obtain the ingots with the size of 30mm×40mm×80mm.

In order to study the evolution of dispersoids during heat treatments, the ingots were heat treated at 400 °C, 450 °C and 500 °C with a heating rate of 5 °C /min for various holding time up to 72 h, followed by water quenching to room temperature (RT). Then the quenched samples were polished and machined for microstructure observation and mechanical tests.

For the microstructure evolution, Optical microscopy (OM) was employed to check the distribution of the dispersoid zone and dispersoid free zone (DFZ). To reveal the dispersoids, the samples were etched by 0.25% HF for 90s. The image analysis equipped on OM was used to quantify the area fraction of dispersoid zone and DFZ. A transmission electron microscope (TEM) operated at 20 KV was used to observe the morphology and the size of dispersoids.

Microhardness was evaluated with a load of 10g and 20 seconds dwelling time.

The test was performed on polished samples for at least 15 measurements and the indentations were guaranteed in the center of dendrite cell in order to precisely evaluate the contribution of dispersoids. Electrical conductivity (EC) was measured on the samples with grinded surface at RT with an average value of 5 measurements for each sample.

The compressive tests were conducted at 25 °C and 300 °C by a Gleeble 3800 thermo-mechanical simulator unit to evaluate the YS. The total strain of the deformed samples was 0.2 and the applied strain rate was $0.001s^{-1}$. The samples were machined in a cylindrical form with a 15mm length and 10mm diameter. Specific heat treatment conditions were selected for the compression strength test depending on its objectives and the results were obtained from the average value of three tests.

In addition, creep tests were also performed at 300 °C in this study on selected conditions. The dimension of samples for creep test is the same with compressive yield strength test. Finally, the evolution of properties during thermal exposure up to 1000h at 300 °C after proper heat treatments was further evaluated from YS and creep resistance.

5.3 Results and discussion

5.3.1 As-cast microstructure and properties

It is reported that Mn or/and Mo addition can modify the Fe-rich intermetallics in Al-Si 356 alloy [5], which is also observed in the present work. As an example, Fig. 5.1 shows the as-cast microstructure of Alloy A and Alloy D, in which it can be found that the platelet β-Fe in Alloy A has been modified into Chinese script α-Fe in Alloy D due to the modification from Mn and Mo additions. However, the majority of Mn or Mo addition is remaining in the solid solution of matrix due to the low volume of Fe-rich intermetallics (~ 2 vol. %) and lower content of Mn/Mo in α-Fe (~5 %). This can also be indicated by the decreasing EC and increasing HV in Fig. 5.1c due to the

solid solution effect from Mn or/and Mo additions in Alloys B, C and D.

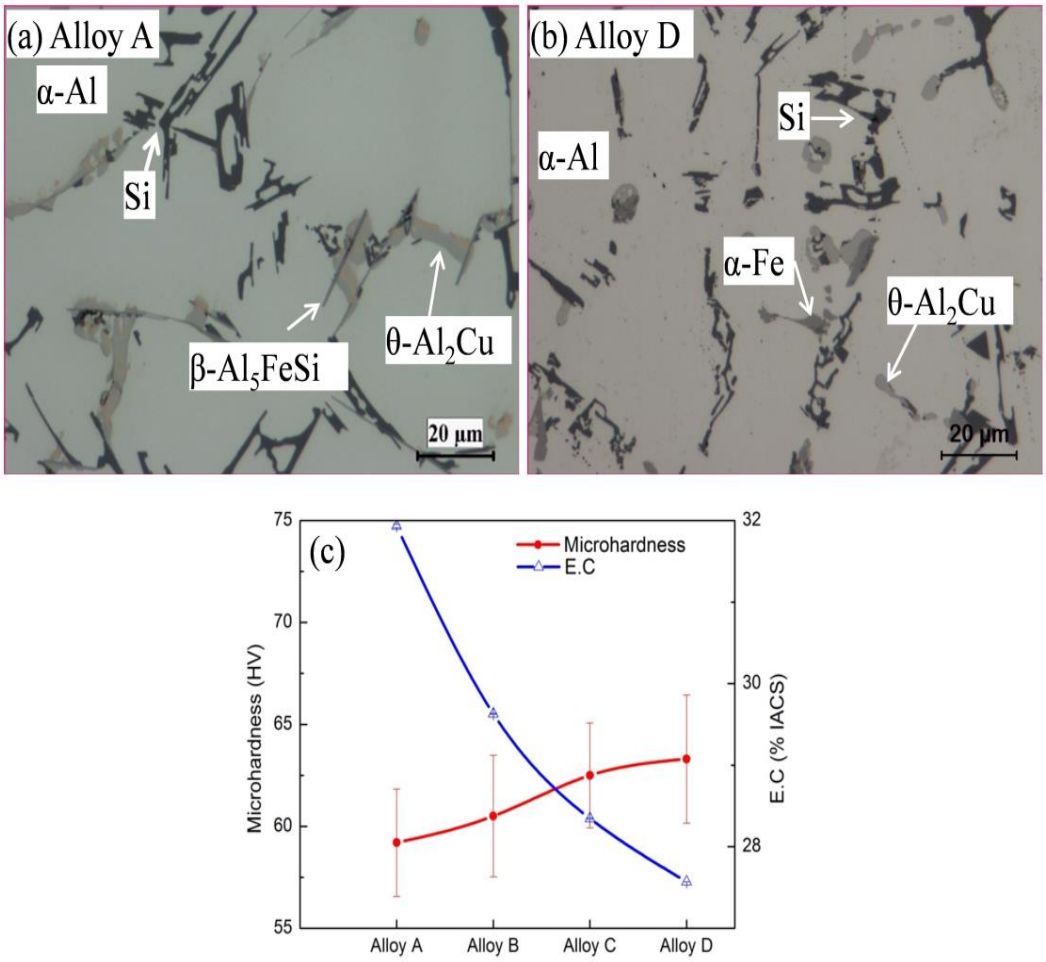

Fig. 5.1 Typical as-cast microstructure of experimental alloys (a) Alloy A, (b) Alloy D, (c) Microhardness and EC of as-cast experimental alloys.

5.3.2 Evolution of Dispersoids during heat treatment

Due to the relative lower incipient melting temperature of Al-Si-Cu 319 cast alloy (~520 °C [3]), the heat treatments at up to 500 °C for different holding time were performed on experimental alloys to investigate the formation and evolution dispersoids in present work. Firstly, the etched microstructure of Alloys A and D after treated at 400 °C, 450 °C and 500 °C for longest holding time were shown in Fig. 5.2 for general observation of dispersoids since the Alloys B, C and D shows similar tendency on the formation behaviour of dispersoids. The dispersoid zone is an area

rich in high number density of dispersoids, while the DFZ is the area where few dispersoids precipitates. Ideally, when a number of α-dispersoids precipitated in the aluminum matrix, the dispersoid zone and DFZ will show different contrast after etching and thus become visible under microscopy.

As shown in Fig. 5.2, no signs of dispersoids can be observed in Alloy A free of Mn and Mo addition when treated from 400 °C/72h (Fig. 5.2a), 450 °C/72h (Fig. 5.2b) up to 500 °C/24h (Fig. 5.2c). On the other hand, Alloy D shows similar microstructure with Alloy A after 400 °C/72h (Fig. 5.2d) but differences can be observed after 450 °C/72h (Fig. 5.2e), in which some very fine dispersoids formed in the cell of dendrites. With increasing temperature (500 °C/24h in Fig. 5.2f), the formation of dispersoids is more obvious in Alloy D with much bigger size and even the DFZ is also observed. Therefore, it can be expected that the formation of dispersoids in Alloy D occurs between 450 °C to 500 °C.

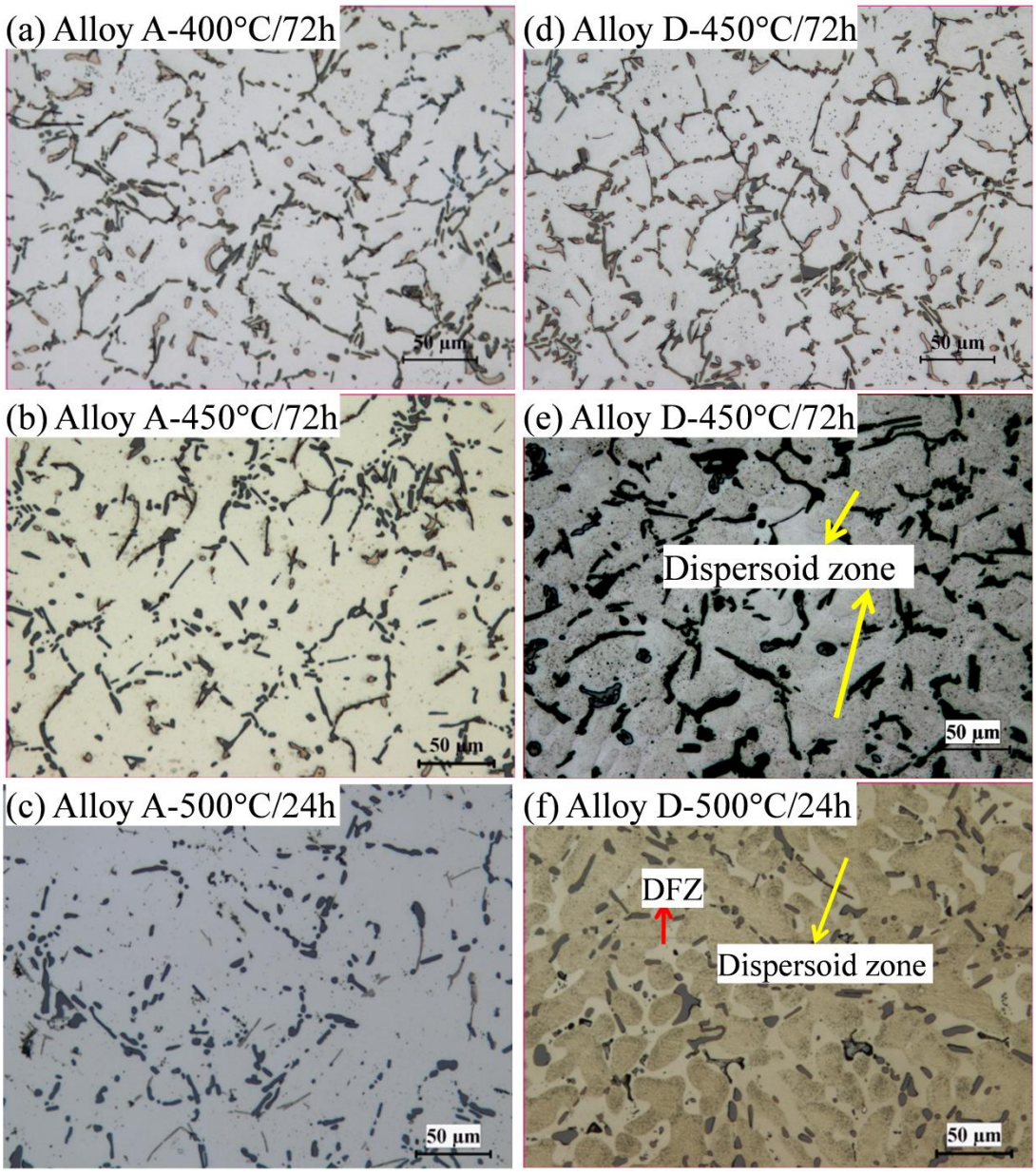

Fig. 5.2 Distribution of dispersoid zone and DFZ in experimental alloys heat treated at 400°C and 450°C.

As shown in Fig. 5.2, the dispersoids started to precipitate after 450 °C/72h and they are clearly distributed in the matrix after 500 °C/24h in Alloy D. Therefore, the evolution of dispersoids during the various holding time treated at 500 °C in Alloys B, C and D are shown in Fig. 5.3. Alloy A is excluded since no dispersoids can be observed even after 500 °C/24h (Fig. 5.2c). General tendency on the dispersoids can be observed in three alloys that the dispersoids begins to form after 2 h (Fig. 5.3 a-c)

and the volume increases with increasing time until to 8 h (Fig. 5.3 d-f) even after 24 h (Fig. 5.3 e-i) with darker color on dispersoids zone due to the coarsening of dispersoids. This is also confirmed by the area fraction of dispersoid zone and DFZ in Fig. 5.4, in which it increases from 2 h to 8 h followed by a plateau until 24 h.

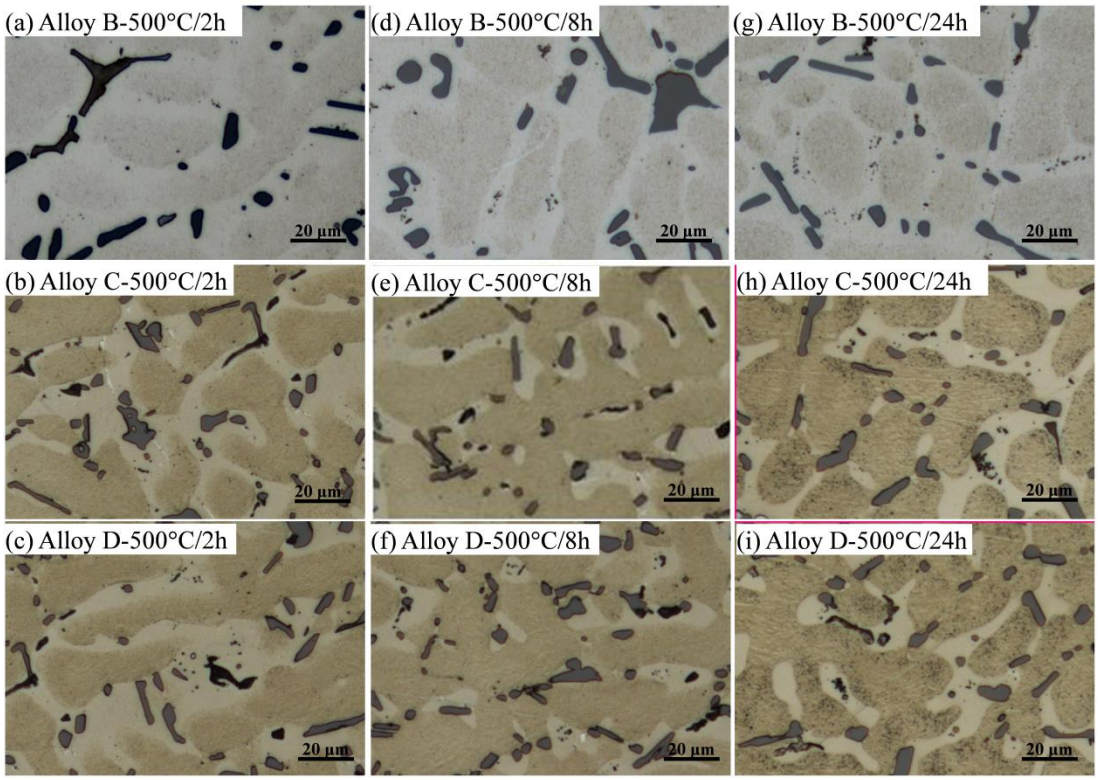

Fig. 5.3 Distribution of dispersoid in Alloys B, C and D heat treated at 500ºC.

However, there are still differences on the evolution of dispersoids between Alloys B, C and D. As shown in Fig. 5.3a, only a slight contrast can be observed between dispersoid zone and DFZ in Alloy B after 500°C/2h but it is already clear enough in Alloys C and D, confirming by the lower area percentage of dispersoid zone in Alloy B (43%) compared with Alloy C (65%) and Alloy D (67%). And the differences on the area fraction of dispersoids increases with holding time. After 500°C/8h-24h, the area fraction of dispersoids in Alloy D can reach as high as 84% compared with 73% in Alloy C and even 53% in Alloy B. Therefore, it seems that Mo is more positive on promoting the formation of dispersoids than Mn, but the combined additions of Mn and Mo can reach the best condition.

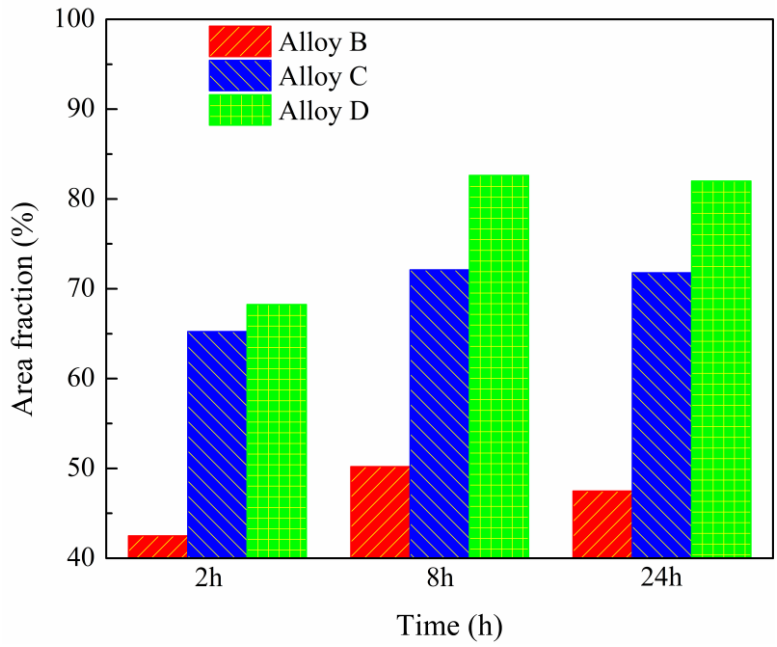

Fig. 5.4 Area fraction of the dispersoid zone in experimental alloys after 500 °C treatment

In order to thoroughly study the evolution of dispersoids, TEM was applied on selected conditions and results are shown in Fig. 5.5. Fig. 5.5 a-c shows the distribution of dispersoids in Alloy D treated at 500 °C for 2, 8 and 24 hours. It can be found that the size of dispersoids is similar after 2h and 8h but the area volume sharply increases after 8 h (Fig. 5.5b). After 24 hours in Fig. 5.5c, the size of dispersoids is bigger with decreasing area volume, indicating the coarsening process of dispersoids. Therefore, the proper heat treatment can be suggested as 500 °C/8h after considering the characters of dispersoids and industrial practice.

Fig. 5.5d and Fig. 5.5e shows the dispersoids after 500°C/8h in Alloy B and Alloy C, respectively. Compared with Alloy D (Fig. 5.5b), the size of dispersoids is much bigger in Alloy B while Alloy C is similar to Alloy D, confirming the more positive effect on dispersoids promotion from Mo than Mn. This can be attributed to the lower diffusion rate of Mo than Mn, causing the lower growth rate of dispersoids. It is reported that diffusivity of Mn is $6.24 \times 10^{-19} m^2 s^{-1}$ at 400 °C, whereas diffusivity of Mo is $5.52 \times 10^{-23} m^2 s^{-1}$ at the same temperature [12, 20]. Therefore,

the size of dispersoids in Alloy C and D is much smaller than Alloy B.

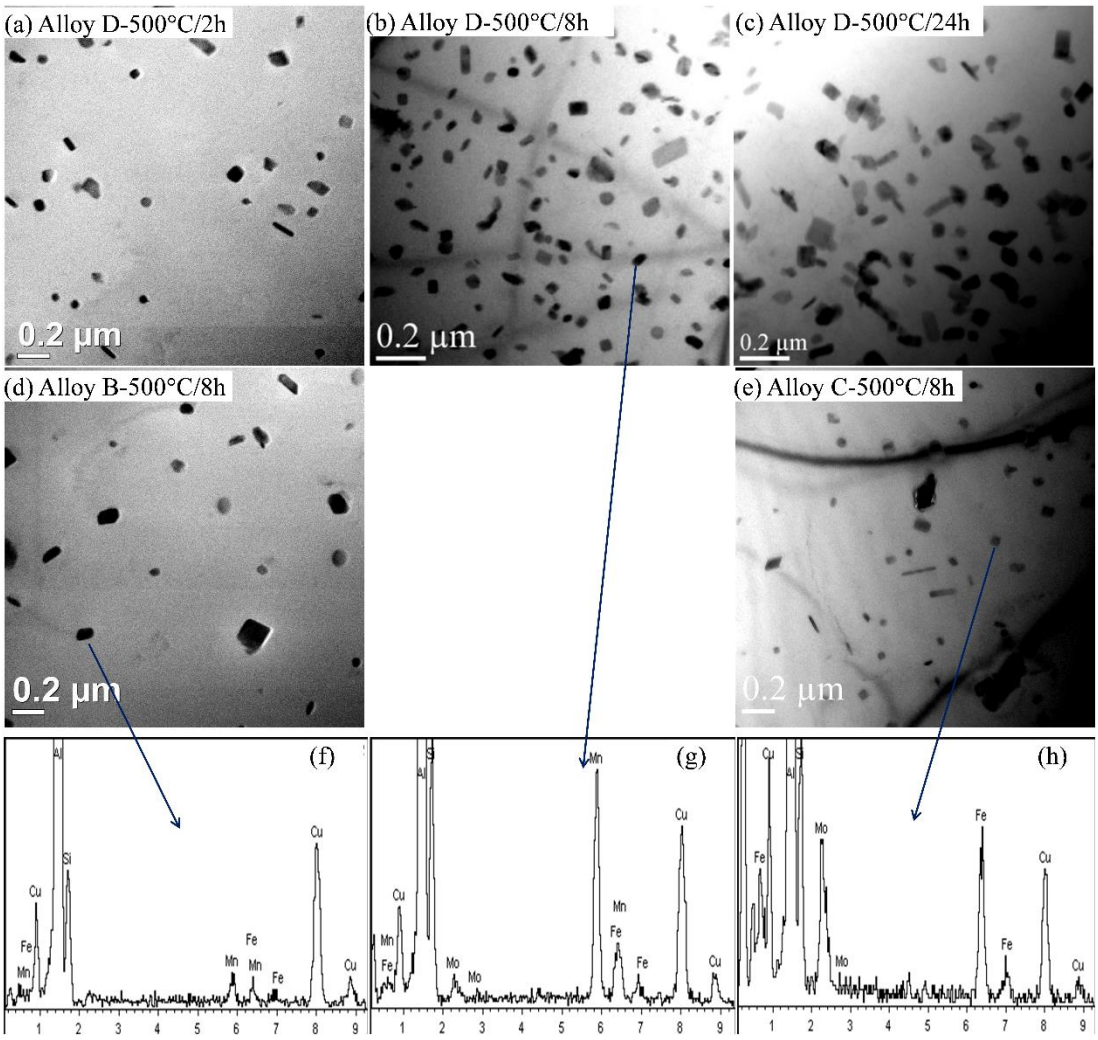

Fig. 5.5 TEM bright filed images showing dispersoids evolution in experimental alloys(heat treated at 500ºC) and their corresponding TEM-EDS analysis results

The TEM-EDS results are also presented in Fig. 5.5f to Fig. 5.5h. Though there is slightly difference in composition depending on Mo or Mn additions, they generally display similar morphology and according to literatures [5, 6, 19], they are indiscriminately named as α-dispersoids in present study.

However, the number density of α-dispersoids in Alloys B and C is much lower than Alloy D, which can be resulted from the combined addition of Mn and Mo in Alloy D. As proposed by Farkoosh *et al.* [6], Mo segregates in the Al dendrite core,

while Mn segregates in the interdendrite region due to the opposite portioning of the Mo and Mn solute atoms during solidification. Therefore, combined Mn and Mo additions favourably contribute to a uniform distribution of α dispersoids as well as the significantly increased volume fraction of dispersoids.

5.3.3 Role of dispersoids on YS at RT and elevated temperature

As shown in Fig. 5.3-Fig. 5.5, it is expected that the dispersoids can quickly precipitate at 500°C and reach to highest volume fraction after 500 °C/8h. Fig. 5.6 presents the compression YS at RT when treated at 500 °C, which also confirms the precipitation behavior of dispersoids with Mn or/and Mo additions. As shown in Fig. 5.6, YS increases with prolonged holding time (2h-8h) but the strengthening mechanism is different within different alloys. Since YS is measured at RT and no artificial aging treatment is applied, therefore, the increasing YS in Alloy A can be attributed to the solid solution strengthening due to gradual dissolution of Al_2Cu into matrix, while the dispersoids are also playing the significant role in Alloys B, C and D besides solid solution strengthening. As shown in Fig. 5.1, the volume of Al_2Cu is similar in four experimental alloys and the volume of Fe-rich intermetallics is low though their morphology changed from platelet to Chinese script. Thus, in present work, we assume that the contribution to mechanical properties from the dissolution of Al_2Cu and Fe-rich intermetallics is similar among four experimental alloys. Therefore, the difference between YS can be principally attributed to the contribution of dispersoids. At 500°C/2h, the differences of YS is smaller due to the lower volume of dispersoids (Fig. 5.3 and Fig. 5.5), which is about 6.5, 11.4 and 14.6 MPa between Alloys B, C, D and Alloy A. However, it rapidly increases with holding time and reaches to 11.4, 17.2 and 22.2 MPa after 500 °C/8h due to the high volume of dispersoids precipitated in Alloys B, C and D (Fig. 5.5), which is a maximum 22% improvement on YS (121.7 MPa in Alloy D compared with 99.5 MPa in Alloy A), indicating the remarkable improvement on mechanical properties from dispersoids at RT. The slight decrease in YS after 500 °C/24h can be attributed to the coarsening of

dispersoids (Fig. 5.5). Besides, comparison among YS in four experimental alloys also confirms the improvement from individual addition of Mo (Alloy C) is higher than individual Mn addition (Alloy B).

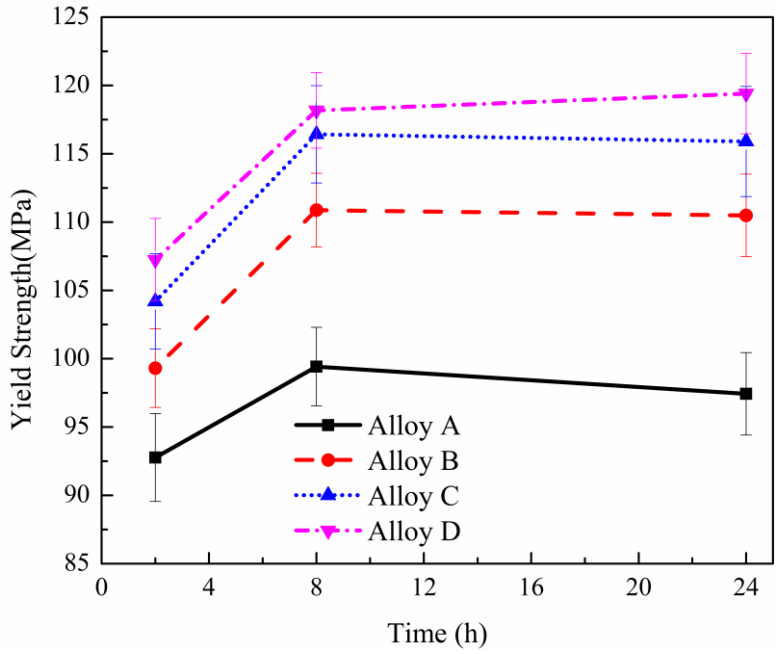

Fig. 5.6 Evolution of YS at RT (alloys solution treated at 500 °C, tested at RT)

Since Al-Si-Cu 319 cast alloys are generally artificial aged in industrial practice to obtain maximum strength. Thus, in present work, experimental alloys were also aged at 155 °C for 5h after optimum solution treatment for dispersoids (500 °C/8h) to reach T6 condition and YS is measured at RT ("T6-RT"). Besides, the elevated-temperature (ET) YS at 300 °C is performed on "T6A" condition ("T6A-ET"), when alloys were further exposed at 300°C for 100h to stabilize Al_2Cu precipitates ("T6A").

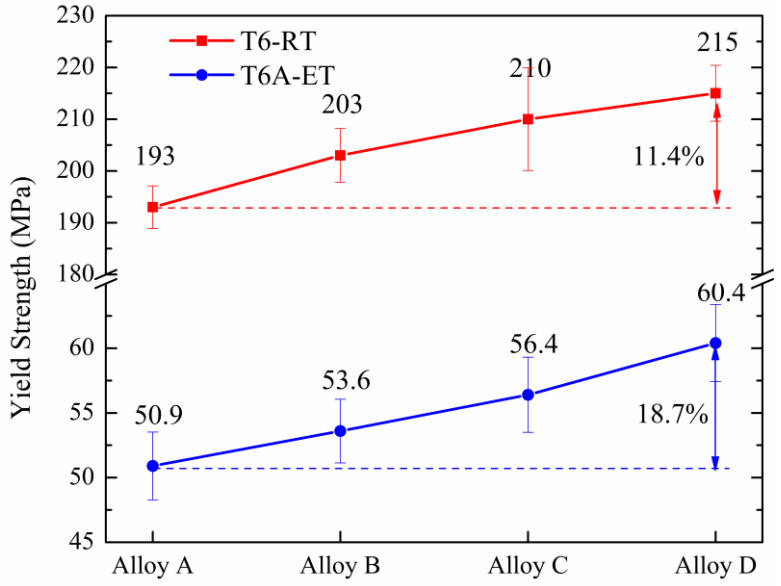

Fig. 5.7 Evolution of Yield Strength for experimental alloys tested at RT after T6(red line), tested at ET after T6+thermal exposure at 300ºC/100h(blue line)

As shown in Fig. 5.7, the YS after "T6-RT" is always higher than the corresponding value shown in Fig. 5.6. This is due to the strengthening of Al_2Cu precipitations during aging treatment. As is shown in Fig. 5.8 a and Fig. 5.8b, The precipitates after T6 were perpendicular to the $(100)_{\alpha\text{-}Al}$ planes. The thickness of the precipitates is only 2-3 nm, and the diameter is approximately 20 nm, which are consistent with θ" precipitates in other studies [21, 22]. Considering the low ageing temperature (155 ºC) and short treatment time (5h), the precipitates after T6 treatment were confirmed as θ" precipitates. These θ" precipitates were coherent with the Al-matrix, contributing to the universally increased YS in all experimental alloys. However, compared with base alloy A, the additional enhancement in YS in Alloy B, C and D is presented. For instance, YS at RT in Alloy D (215MPa) is 11.4% higher than in Alloy A (193MPa), which can be attributed principally to the formation of dispersoids in Alloy D, confirming the additional contribution of dispersoids on RT mechanical properties in addition to the precipitation strengthening from θ" precipitates. Meanwhile, the YS after T6A-ET is always significantly lower after 100h soaking at 300 ºC, as is shown in Fig. 5.7 The deterioration is likely due to the

coarsening of θ" precipitates during thermal exposure at 300 ^{o}C [23]. The coarsening behaviour in present study corresponds with other studies [23, 24] after thermal exposure at temperatures significantly higher than proceeding ageing temperature.

As is indicated by red arrows in Fig. 5.8c and Fig. 5.8d. the previously fine and oriented precipitates coarsened into coarse equilibrium Al_2Cu phases, which are non-coherent with the Al matrix. The size of the precipitates also increases from 20nm to around 0.2 μm after 300 ^{o}C/100h holding, confirming the coarsening of precipitates. Consequently, they can only provide very limited strengthening, leading to the universal deterioration of YS in four experimental alloys after thermal exposure at 300^{o}C/100h. Albeit, the enhancement in YS even after 300 °C/100h thermal exposure can be observed in alloys B, C and D compared with alloy A, as is shown in Fig. 5.7, YS increases from 50.9MPa in Alloy A to 60.4MPa in Alloy D, exhibiting 18.7% enhancement in YS. This can be attributed to the presence of α-dispersoids, as indicated in blue arrows in Fig. 5.8d, their size remains in the range of 70-100 nm even after 300 ^{o}C/100h thermal exposure, confirming their perfect thermally stability. In addition, the increasing tendency in YS at both RT and ET from Alloy A to B, C and D also confirms the contribution from the addition is in the order of Mn, Mo and (Mn+ Mo).

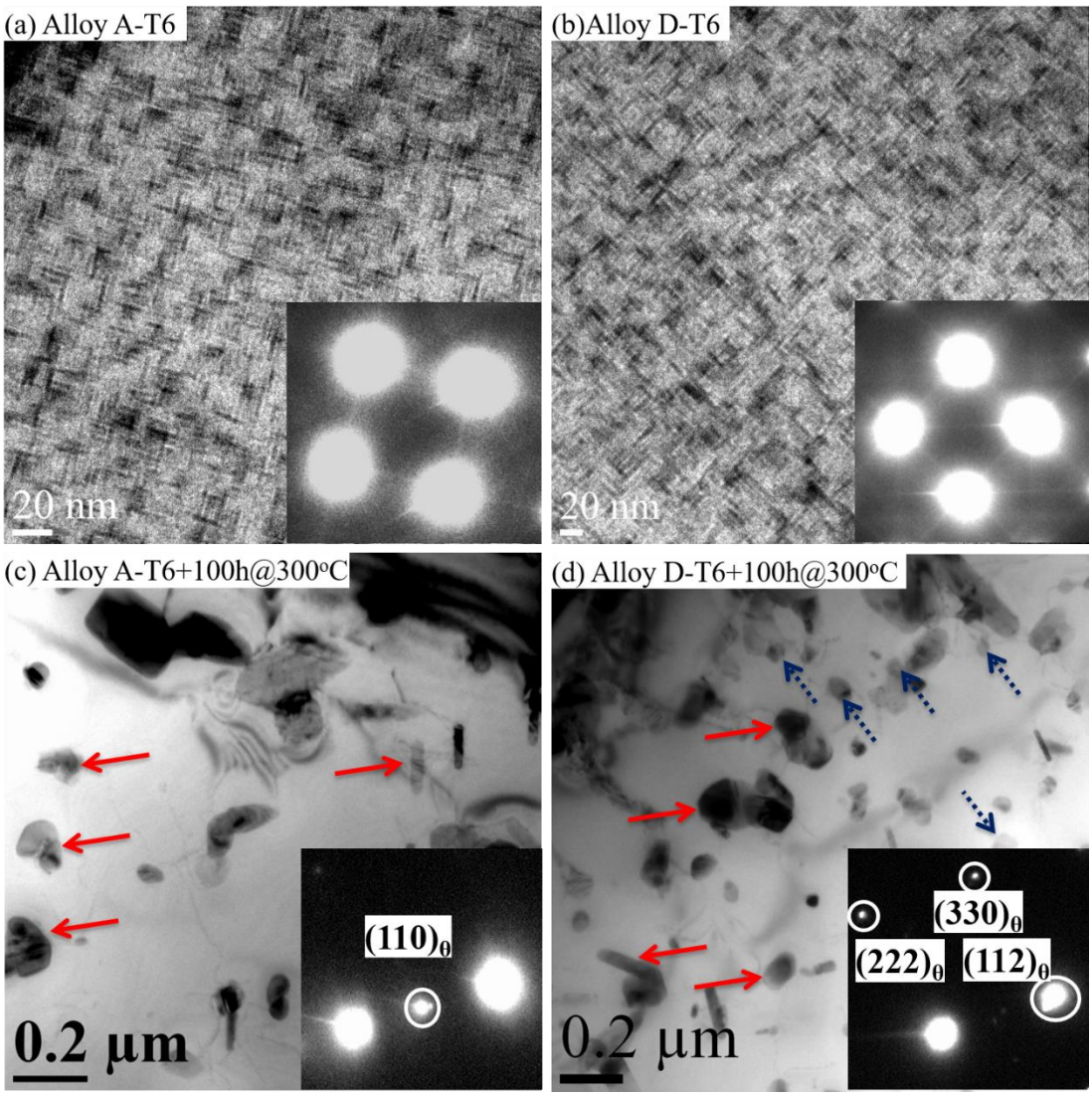

Fig. 5.8 TEM micrographs of Alloy A (a) T6, (b) T6+300°C/100 and Alloy D (c) T6, (d) T6+300°C/100h, red arrows indicate the Cu precipitates; blue arrows indicate the α-dispersoids

5.3.4 Evolution of creep resistance with Mn or/and Mo additions

Creep resistance is considered as one of the most important criteria for high temperature applications. In the present work, compressive creep tests were conducted at 300 °C to investigate the effect of Mn, Mo additions on the creep resistance of experimental alloys. As discussed in Section 3.2, 500 °C/8h is found to be the optimum condition for the dispersoids based on the microstructure observation

(Fig. 5.3 and Fig. 5.5) as well as the mechanical properties (Fig. 5.6 and Fig. 5.7). Therefore, all the samples for the creep tests are solution treated at 500 °C/8h and then aged at 155 °C/5h followed by soaking 300 °C/100h ("T6A") in order to simulate the real situation of parts during services. The typical creep curves of experimental alloys under the constant load of 30 MPa are shown in Fig. 5.9. Generally, the creep strain increases rapidly in the first few hours during the initial stage, then the creep deformation turns into a quasi-steady state, in which the creep rate becomes more or less constant with the progress of the creep deformation and then the minimum creep rate ($\dot{\varepsilon}$) can be calculated during this stage. However, large difference can be observed between alloys, especially the maximum strain reached after 96 hours. As shown in Fig. 5.9, the maximum strain of Alloy A already reached to 0.17 while it is only 0.04 in Alloy B and it is further decreased to 0.015 in Alloy C and 0.006 in Alloy D, confirming the positive effect on the creep resistance from the addition of Mn and Mo. The measured maximum strain and calculated minimum creep rate under this condition is summarized in Table 5.2. It can be found that the $\dot{\varepsilon}$ also greatly varied with Mo and/or Mn addition. As shown in Table 5.2, $\dot{\varepsilon}$ is 5.5E-07 s^{-1} in Alloy A but it decreased to 1.0E-07 s^{-1} in Alloy B and 3.1E-08 s^{-1} in Alloy C and further to 1.1E-08 s^{-1} in Alloy D, which is 50 times lower than that in Alloy A. Meanwhile, it can also be found that Alloy C has lower maximum strain and $\dot{\varepsilon}$ than Alloy B, confirming the stronger influence on creep resistance from individual addition of Mo than Mn.

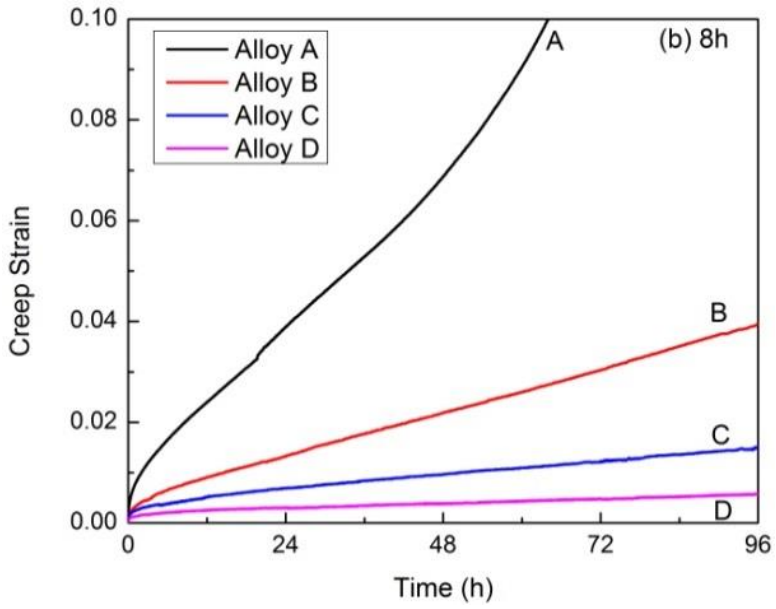

Fig. 5.9 Typical creep curve under a constant load of 30 MPa (alloys treated at 500 °C for 8h, then 155 °C/5h aged followed by 300 °C/100h soaking.)

Table 5.2 Creep properties of experimental alloys

Properties	A	B	C	D
Total Strain	0.17	0.040	0.015	0.0057
Minimum creep rate(s-1)	5.5E-07	1.0E-07	3.1E-08	1.1E-08

In order to detailed investigate the evolution of creep resistance with Mn and Mo additions, the creep tests were further performed at different loads (25, 30, 35 and 40 MPa) in present work to obtain the threshold stress (σ_{th}) and true stress exponent *n*. For the threshold stress σ_{th}, it is calculated to be the stress at the creep rate of 10^{-10} s^{-1} below which the creep is experimentally not measurable, by extrapolating the linear fitted double-logarithmic curves of $\dot{\varepsilon}$ vs applied stress σ (Fig. 5.10). Then the true stress exponent *n* was determined according to the following the slope of the double-logarithmic curve of $\dot{\varepsilon}$ vs (σ-σ_{th}) after determining the threshold stress σ_{th}

according to the following equation:

$$\dot{\varepsilon}_m = A' \left(\frac{\sigma - \sigma_{th}}{G}\right)^n \exp\left(-\frac{Q}{RT}\right) \qquad \text{Eq. 5.1}$$

Where, $\dot{\varepsilon}_m$ is the minimum creep rate, σ_{th} is calculated threshold stress, Q is the activation energy, G is the shear modulus, n is the true stress exponent, A' is a constant, R is the universal gas constant and T is the absolute temperature. The calculated threshold stress σ_{th} and true stress exponent *n* are listed in Table 5.3.

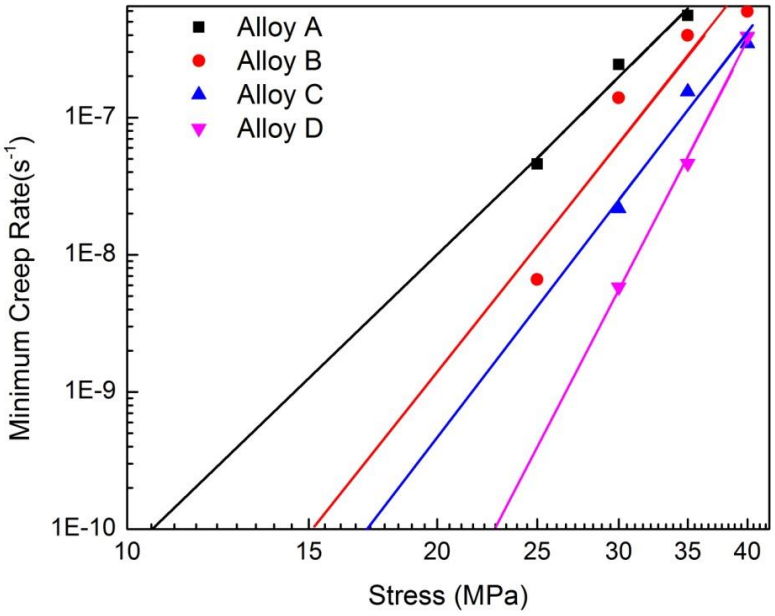

Fig. 5.10 Logarithmic plots of the minimum creep rate ε_m vs. applied stress σ for alloys tested at 300 °C

As shown in Table 5.3, the calculated true stress exponent *n* is around 3-4 for four experimental alloys, which is in the range of dislocation glide (n=3) and dislocation climb (n=5). Thus, the governing creep deformation mechanism is assumed to be combined dislocation glide and dislocation climb in the present work [25-27]. Consequently, the factors that can affect the movement of dislocations will have influence on the creep resistance, which are the solid solution atoms, precipitates and dispersoids in present work. As discussed in last section, the solid solution level as well as the precipitation condition should be similar in four experiment alloys, thus

the biggest contributor is reasonably considered as the dispersoids, as displayed in Fig. 5.4 and Fig. 5.6.

Table 5.3 Summary of creep properties of experimental alloys

Creep Value for alloys	Alloy A	Alloy B	Alloy C	Alloy D
Threshold Stress (MPa)	10.6	15.2	17.2	22.8
True Stress Exponent (n_t)	3.93	3.83	3.84	3.37

Threshold stress σ_{th} is normally considered to be the stress required to detach a dislocation from an obstacle or the additional stress required for climbing over an obstacle [28, 29].As shown in Table 5.3, σ_{th} increases from 10.6 MPa in Alloy A to 15.2 in Alloy Band 17.2 in Alloy C and further to 22.8 MPa in Alloy D. It is also reported that an increase of 3 MPa in threshold stress translates into an order of magnitude decrease in the minimum creep rate [6][30]. In present work, the minimum creep rate has been decreased 50 times with an increase of threshold stress of 12.8 MPa from Alloy D to Alloy A, confirming an overall positive influence from the addition of Mn and/or Mo. The increasing threshold stress σ_{th} from Alloy A to D can also principally contributed to the increasing volume of dispersoids, further confirming the positive effect of dispersoids on the creep resistance besides their improvement on the mechanical properties (YS). Furthermore, the descending of interdendrite DFZs (where dislocations can move freely at low stresses) with Mo and Mn addition in studied alloys favours effective dislocation pinning and contributes to the increasing σ_{th} [31].

Finally, the activation energy Q was also evaluated under the load of 30 MPa with the compression test performed at 300 ^{o}C. Q can be calculated as the R (gas constant) times of slope of fitting curve of $\mathrm{Ln}\,\dot{\varepsilon}$ vs. $1/T$. In present work, Q is

calculated to be 64, 67, 63 and 70 kJ/mol for Alloys A, B, C and D, respectively as shown in Fig. 5.11. The activation energy obtained in present study is significantly less than results in study [25], which can be attributed to the coarsening of Cu precipitates during the soaking at 300 ^{o}C/100h. However, differences can also be observed among alloys. For instance, Q increases from 64 kJ/mol in Alloy A to 70 kJ/mol in Alloy D, demonstrating 10% improvement, which also confirms the positive effect of Mo/Mn dispersoids.

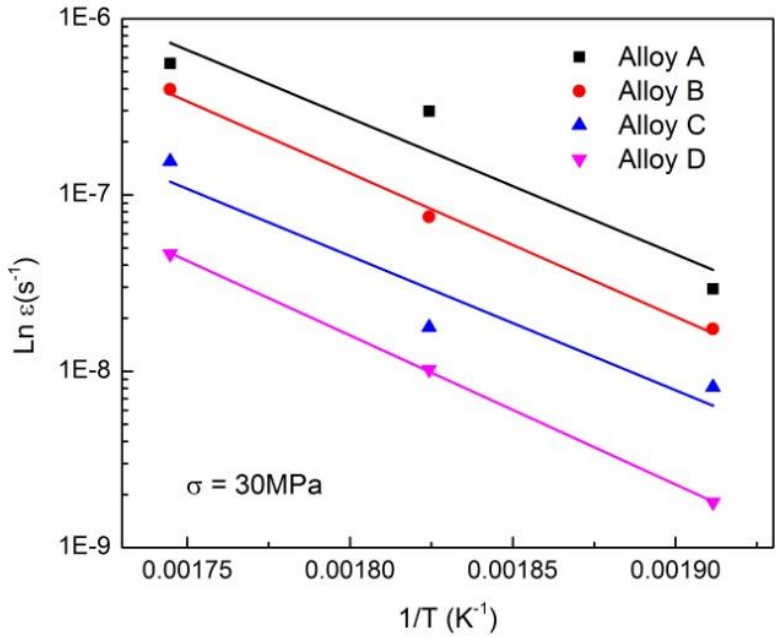

Fig. 5.11 Arrhenius plots-Logarithmic plots of the steady stage minimum creep rate Lnε vs. 1/T under an applied stress of 30 MPa.

5.3.5 Long-term thermal stability of elevated-temperature properties

The thermal stability of mechanical properties is an important consideration for the alloys utilized at elevated temperature. In present study, in order to investigate the thermal stability of elevated-temperature properties, a long-term thermal holding at 300 °C for up to 1000h was performed after T6A to evaluate the thermal stability of the mechanical properties.

Fig. 5.12 displays the evolution of YS during the long-term thermal holding of experimental alloys. Apparently, all four experimental alloys experience decrease in YS due to continuous coarsening of Al_2Cu precipitates. However, the degree of decline varies with alloys. For instance, YS of alloy A dropped from 51.0 MPa after 100h to 35.4 MPa after 1000h, which is 30.0% decrease. On the other hand, it is only 10.1% decrease for Alloy D from 60.4 MPa after 100h to 54.3 MPa after 1000h due to the dispersoids from the additions of Mn and Mo, indicating its better thermal stability. While the decline in Alloy B and C is moderate (18.9% in Alloy B and 16.1% in Alloy C), showing the similar tendency on the evolution of YS. Since α-dispersoids are relatively thermally stable at 300-350 ^{o}C [19]. Therefore, the promising thermal stable in Alloy D can still be obtained although the coarsening of precipitates is inevitable at 300 ^{o}C.

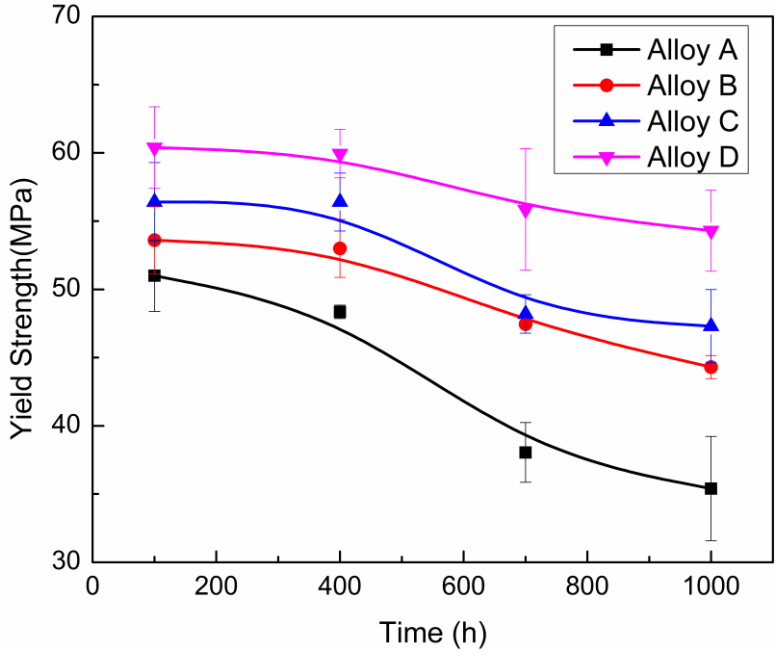

Fig. 5.12 Evolution of YS during a long-term thermal holding at 300 °C in experimental alloys.

Compressive creep tests were also performed after a long-term thermal exposure at 300 °C for up to 1000h after T6 treatment, and maximum strain and minimum creep rate of four experimental alloys after 100h and 1000 h are summarized in

Fig. 5.13.

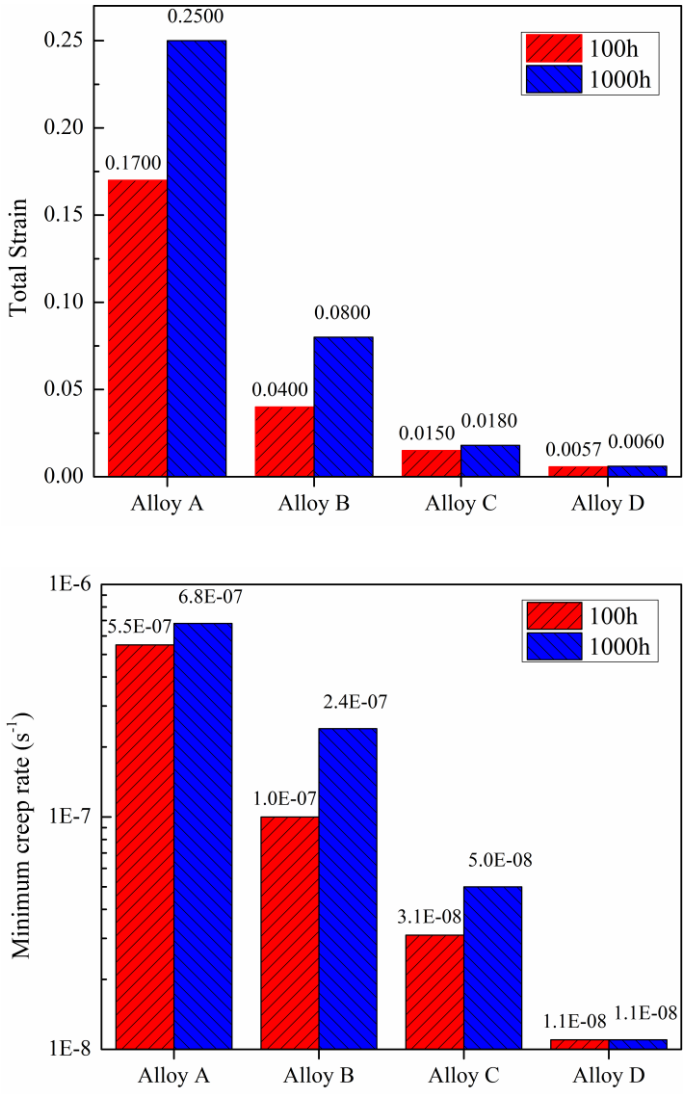

Fig. 5.13 Comparison of (a) Total strain and (b) minimum creep rate for four experimental alloys after long-time thermal holding at 300 °C for 100h and 1000h.

It is evident that the total creep strain and minimum creep rate of all four experimental alloys increases after 1000h holding compared with that after 100 h, which can be attributed to the coarsening of precipitates [32]. However, like the evolution of YS during thermal holding in Fig. 5.12, the increasing extent varies for different alloys. For instance, the total creep strain in Alloy A, increased from 0.17 to 0.25 which is 47% decrease, while the minimum creep rate also increases from

5.5E-07 s^{-1} to 6.8E-07 s^{-1}. Alloys B and C exhibits moderate increase in both total strain and minimum creep rate, indicating improved thermal stability. In contrast, total creep strain of Alloy D increase only from 0.0057 to 0.006 (only 5% increase), while minimum creep rate remains at 1.1E-08 s^{-1}even after 1000h soaking at 300 °C, which remains almost constant during prolonged 300 ºC holding, indicating the most desirable thermal stability.

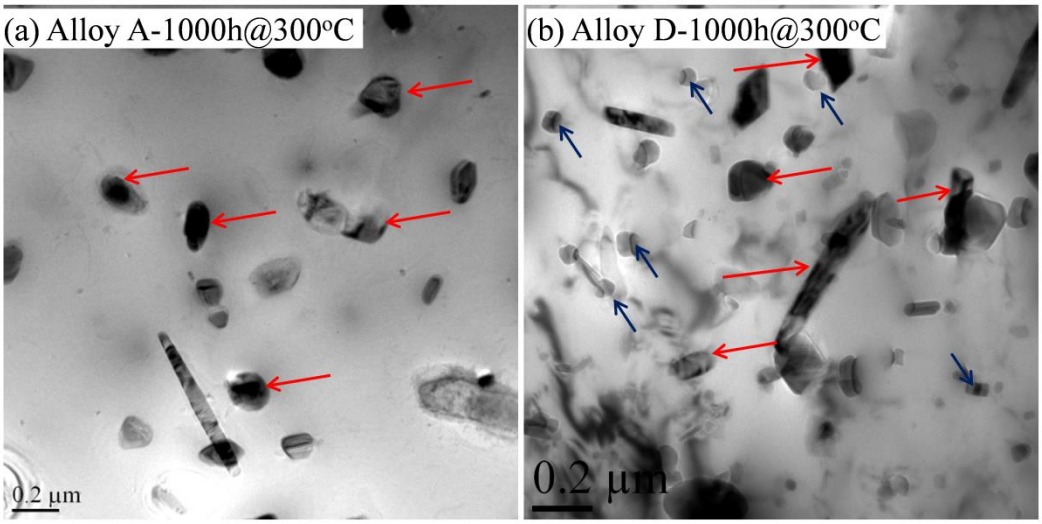

Fig. 5.14 TEM bright field images showing α-dispersoids and Cu precipitates in Alloy A and D after T6+thermal exposure at 300 ºC/1000h (red arrows indicate the Cu precipitates; blue arrows indicate the α-dispersoids)

Fig. 5.14 shows the TEM micrographs of α-dispersoids and precipitates in Alloy A and Alloy D after T6 and thermal exposure at 300ºC/1000h. In Alloy A, compared with 300 ºC/100h (Fig. 5.8a), after thermal exposure at 300 ºC/1000h (Fig. 5.14a), , almost all observant precipitates coarsened into equilibrium non-coherent θ-Al_2Cu phases (indicated by red arrows), the size of some Cu precipitates increases from 200 nm (Fig. 5.8c) to almost 1000 nm (Fig. 5.14a). The coarsening structure correlates to the structure of Al-Cu-Mg alloy after thermal exposure at 250 ºC/2000h [24]. The coarsening of precipitates thus leads to significantly deterioration in both YS and creep resistance, as shown in Fig. 5.12 and Fig. 5.13. In Alloy D, similar in Alloy A, Cu precipitates inevitably coarsened during prolonged thermal exposure at

300 °C/1000h. However, the size of α-dispersoids (indicated by blue arrows) remains around 60-80 nm, showing little signs of coarsening, confirming their perfect thermal stability even after thermal exposure at 300 ^{o}C/1000h (Fig. 5.14b). Thus, due to the formation of large number of thermally stable α-dispersoids, their impending effect on dislocation movements are partially compensated, leading to the least YS decrease (10%) and almost unchanged creep resistance. It can be expected that since Alloys B and C precipitate only modest amount of α-dispersoids during solution treatment at 500 °C/8h, thus their strengthening effect cannot compensate the coarsening of θ-Al_2Cu precipitates, leading to moderate thermal stability. Hence, introduction of thermally stable dispersoids can be an effective method to improve the thermal stability of alloys under elevated-temperature applications, providing wider temperature range for application of Al-Si-Cu 319 alloys.

5.4 Conclusions

In the present work, the effects of Mo and Mn additions alloys on the evolution of dispersoids during various heat treatment conditions were investigated in Al-Si-Cu 319 cast alloys. Besides, their effects on yield strength (YS) and creep resistance at elevated temperature (300^{o}C) were also studied. The following conclusions are drawn:

1) The dispersoids commence to form at 450 °C during heat treatment and the optimum condition for dispersoids with higher volume fraction and finer size can be reached after 500°C/8h treatment.
2) Both Mn and Mo can promote the precipitation of dispersoids. However, individual addition of Mo has stronger positive effect than individual Mn addition but weaker than the combined addition of Mn and Mo.
3) Complementary improvement on the yield strength at room temperature (~ 10%) while remarkable increase on that at 300 °C (~ 20%) can be obtained due to the fully precipitation of dispersoids.

4) The creep resistance is greatly improved with additions of Mn or/and Mo. Compared with alloys free of Mn and Mo, the minimum creep rate decreases from 5.5E-07s^{-1} to 1.1E-08s^{-1} while the threshold stress increases from 10.6 to 22.8 MPa in alloy with combined additions of Mn and Mo due to the formation of dispersoids.
5) YS and creep resistance in all experimental alloys decrease during thermal exposure at 300 °C due to the continuous coarsening of Cu precipitates. However, much lower decreasing extend is observed due to the addition of Mn or/and Mo. During thermal exposure at 300 °C up to 1000 hours, 10% decrease on yield strength and 5% increase on the maximum creep strain is reached in alloys with combined additions of Mn and Mo compared with 30% decrease and 47% increase in the base alloy free of Mn and Mo, respectively, showing the superior thermal stability of Al-Si-Cu 319 alloys with Mn and Mo additions.

References

[1] A. Lombardi, C. Ravindran, R. MacKay, Optimization of the solution heat treatment process to improve mechanical properties of 319 Al alloy engine blocks using the billet casting method, Materials Science and Engineering: A 633(0) (2015) 125-135.

[2] S. Alkahtani, Mechanical performance of heat treated 319 alloys as a function of alloying and aging parameters, Materials & Design 41 (2012) 358-369.

[3] M. Javidani, D. Larouche, Application of cast Al-Si alloys in internal combustion engine components, International Materials Reviews 59(3) (2014) 132-158.

[4] A. Mohamed, F. Samuel, A Review on the Heat Treatment of Al-Si-Cu/Mg Casting Alloys, Conventional and Novel Applications (2012) 229.

[5] A.R. Farkoosh, X.G. Chen, M. Pekguleryuz, Dispersoid strengthening of a high temperature Al-Si-Cu-Mg alloy via Mo addition, Materials Science and Engineering: A 620 (2015) 181-189.

[6] A.R. Farkoosh, X. Grant Chen, M. Pekguleryuz, Interaction between molybdenum and manganese to form effective dispersoids in an Al-Si-Cu-Mg alloy and their influence on creep resistance, Materials Science and Engineering: A 627 (2015) 127-138.

[7] M. Tocci, R. Donnini, G. Angella, A. Pola, Effect of Cr and Mn addition and heat treatment on AlSi3Mg casting alloy, Materials Characterization 123 (2017) 75-82.

[8] K. Liu, X.G. Chen, Development of Al–Mn–Mg 3004 alloy for applications at elevated temperature via dispersoid strengthening, Materials & Design 84 (2015) 340-350.

[9] D. Tsivoulas, P.B. Prangnell, The effect of Mn and Zr dispersoid-forming additions on recrystallization resistance in Al-Cu-Li AA2198 sheet, Acta Materialia 77 (2014) 1-16.

[10] A.M.F. Muggerud, E.A. Mortsell, Y.J. Li, R. Holmestad, Dispersoid strengthening in AA3xxx alloys with varying Mn and Si content during annealing at low temperatures, Materials Science and Engineering: A 567 (2013) 21-28.

[11] D. Tsivoulas, J.D. Robson, C. Sigli, P.B. Prangnell, Interactions between zirconium and manganese dispersoid-forming elements on their combined addition in Al-Cu-Li alloys, Acta Materialia 60(13-14) (2012) 5245-5259.

[12] K.E. Knipling, D.C. Dunand, D.N. Seidman, Criteria for developing castable, creep-resistant aluminum-based alloys–A review, Zeitschrift Fur Metallkunde 97(3) (2006) 246-265.

[13] K.E. Knipling, D.C. Dunand, D.N. Seidman, Precipitation evolution in Al-Zr and Al-Zr-Ti alloys during isothermal aging at 375-425 ^{o}C, Acta Materialia 56(1) (2008) 114-127.

[14] K.E. Knipling, D.C. Dunand, D.N. Seidman, Precipitation evolution in Al-Zr and Al-Zr-Ti alloys during aging at 450-600 ^{o}C, Acta Materialia 56(6) (2008) 1182-1195.

[15] F. Qian, S. Jin, G. Sha, Y. Li, Enhanced dispersoid precipitation and dispersion strengthening in an Al alloy by microalloying with Cd, Acta Materialia 157 (2018) 114-125.

[16] Y.J. Li, A.M.F. Muggerud, A. Olsen, T. Furu, Precipitation of partially coherent alpha-Al(Mn,Fe)Si dispersoids and their strengthening effect in AA 3003 alloy, Acta Materialia 60(3) (2012) 1004-1014.

[17] K. Liu, X.G. Chen, Development of Al-Mn-Mg 3004 alloy for applications at elevated temperature via dispersoid strengthening, Materials & Design 84 (2015) 340-350.

[18] Y.J. Li, L. Arnberg, Quantitative study on the precipitation behavior of dispersoids in DC-cast AA3003 alloy during heating and homogenization, Acta Materialia 51(12) (2003) 3415-3428.

[19] K. Liu, H. Ma, X.G. Chen, Enhanced elevated-temperature properties via Mo addition in Al-Mn-Mg 3004 alloy, Journal of Alloys and Compounds 694 (2017) 354-365.

[20] C.J. Kuehmann, P.W. Voorhees, Ostwald ripening in ternary alloys, Metallurgical and Materials Transactions A 27(4) (1996) 937-943.

[21] A. Wiengmoon, J.T.H. Pearce, T. Chairuangsri, S. Isoda, H. Saito, H. Kurata,

HRTEM and HAADF-STEM of precipitates at peak ageing of cast A319 aluminium alloy, Micron 45 (2013) 32-36.

[22] A. Biswas, D.J. Siegel, C. Wolverton, D.N. Seidman, Precipitates in Al–Cu alloys revisited: Atom-probe tomographic experiments and first-principles calculations of compositional evolution and interfacial segregation, Acta Materialia 59(15) (2011) 6187-6204.

[23] W.S. Tian, Q.L. Zhao, Q.Q. Zhang, F. Qiu, Q.C. Jiang, Superior creep resistance of 0.3 wt% nano-sized TiCp/Al-Cu composite, Materials Science and Engineering: A 700 (2017) 42-48.

[24] S.P. Ringer, W. Yeung, B.C. Muddle, I.J. Polmear, Precipitate stability in Al Cu Mg Ag alloys aged at high temperatures, Acta Metallurgica Et Materialia 42(5) (1994) 1715-1725.

[25] H.R. Erfanian-Naziftoosi, E.J. Rincón, H.F. López, Creep Properties of the As-Cast Al-A319 Alloy: T4 and T7 Heat Treatment Effects, Metallurgical and Materials Transactions A 47(8) (2016) 4258-4267.

[26] L. Shi, D.O. Northwood, Recent Progress in the Modeling of High-Temperature Creep and Its Application to Alloy Development, Journal of Materials Engineering and Performance 4(2) (1995) 196-211.

[27] L. Pan, F.A. Mirza, K. Liu, X.G. Chen, Effect of Fe-rich particles and solutes on the creep behaviour of 8xxx alloys, Materials Science and Technology (2016) 1-8.

[28] J. Rösler, E. Arzt, The kinetics of dislocation climb over hard particles—I. Climb without attractive particle-dislocation interaction, Acta Metallurgica 36(4) (1988) 1043-1051.

[29] L. Pan, K. Liu, F. Breton, X. -Grant Chen, Effect of Fe on Microstructure and Properties of 8xxx Aluminum Conductor Alloys, Journal of Materials Engineering and Performance 25(12) (2016) 5201-5208.

[30] A.R. Farkoosh, M. Pekguleryuz, The effects of manganese on the T-phase and creep resistance in Al–Si–Cu–Mg–Ni alloys, Materials Science and Engineering: A 582(0) (2013) 248-256.

[31] F. Carreno, O.A. Ruano, Threshold stresses in high temperature deformation of dispersion strengthened aluminum alloys, Materials Science and Engineering: A 214(1-2) (1996) 177-180.

[32] Y. Gao, C. Yang, J. Zhang, L. Cao, G. Liu, J. Sun, E. Ma, Stabilizing nanoprecipitates in Al-Cu alloys for creep resistance at 300° C, Materials Research Letters 7(1) (2019) 18-25.

Chapter 6 Improved elevated-temperature properties in Al-13%Si piston alloys by Mo addition

Abstract:

Eutectic Al-13%Si alloys are widely used in auto industry for manufacturing pistons and cylinder heads. To reduce greenhouse gas emission and enhance the engine efficiency, the deterioration of elevated-temperature mechanical properties and creep resistance of piston materials at relatively high service temperature (250~350 ^{o}C) has become one of key industrial concerns in engine design. In the present work, Mo was added to the Mn-containing Al-13%Si piston alloys aiming at strengthening the alloys at elevate temperature. Compared with the individual Mn-containing base alloy, Mo can further enhance the precipitation of α-dispersoids by expanding dispersoid zone and restricting the dispersoid free zone after the precipitation treatment at 520 ^{o}C for 12 h, resulting in a remarkable improvement of yield strength at both room temperature and 300 ^{o}C as well as the creep resistance at 300 ^{o}C. The beneficial effect of the Mo addition on the improved yield strength and creep resistance is especially prominent during the long-term thermal exposure at 300 ^{o}C due to the presence of thermally stable dispersoids and the retardation of the fragmentation and spheroidization of Si particles.

6.1 Introduction

Al-13%Si alloys are widely used for automotive components such as cylinder heads and pistons due to their high strength, excellent wear resistance and low thermal expansion [1, 2]. Typical working temperature for a diesel engine in the modern automotive industry can reach up to 300-400 ^{o}C due to the trend in engine design to reduce greenhouse gas emission and enhance the engine efficiency [3, 4], therefore

elevated-temperature strength, thermal fatigue and creep resistance are important considerations for the design of piston materials [5].

Until recently, the improvement of elevated-temperature properties in Al-13%Si piston alloys is predominately achieved from the addition of aluminide-forming elements, such as Fe [6, 7], Ni [8, 9] and Cu [9, 10], to form various intermetallics with a large volume fraction during solidification. These intermetallics are thermally stable compared with Si particles enabling the establishment of rigid networks with Si particles. For example, the improvement of elevated-temperature strength was achieved by Ni addition to form a highly interconnected 3-D structure with 20 vol.% of eutectic Si, Al9FeNi and Al15(Mn,Fe)3Si2 aluminides [10]. The Si network is one of the most striking features for eutectic Al-Si piston alloys [11, 12] and the fragmentation and spheroidization of eutectic Si at elevated temperature is almost inevitable [13, 14] due to its relatively high diffusion rate [15]. Although the spheroidization of eutectic Si is believed to have a beneficial effect on the elongation at room temperature [16, 17], the continuous spheroidization of Si particles would deteriorate the elevated temperature strength, thus needs to be restrained for elevated temperature applications [6].

The approach mentioned above focused mainly on utilizing alloying elements to form a large quantity of high melting point intermetallics during solidification to compensate the otherwise spheroidized and disconnected Si network during heat treatment and high temperature service to achieve the required strength at elevated temperature. However, the strengthening of α-Al matrix for Al-Si piston alloys is almost neglected. Dispersoid strengthening has long been an efficient way to improve elevated-temperature properties by precipitation of thermally stable dispersoids after appropriate heat treatment [18]. Many elements [19-23] have been confirmed to be able to precipitate a wide variety of dispersoids to improve elevated-temperature properties. Recently Liu. *et al.* [3] confirmed that Mn can promote the precipitation of α-Al(Mn,Fe)Si dispersoids to strengthening Al-13%Si alloys at elevated-temperature,

and a significant improvement in both strength and creep resistance was achieved. Mo has been reported to promote α-Al(Mo,Fe)Si dispersoids in hypoeutectic Al alloys and additional strengthening effect on yield strength has been obtained by forming large quantity of thermal stable α-Al(Mo,Fe)Si dispersoids [24]. However, Mo alloying in eutectic Al-13%Si alloys is not reported yet, much less its effect on elevated-temperature mechanical properties.

In the present work, the precipitation of dispersoids by different Mo additions in a Mn-containing Al-13%Si piston alloy was studied by characterization of the dispersoid zone and dispersoid free zone during heat treatment using optical, scanning electron and transmission electron microscopes. The influence of the Mo addition and its dispersoids on the yield strength and creep resistance at 300 ^{o}C was investigated. The evolution of microstructure, yield strength and creep resistance during prolonged thermal exposure at 300 ^{o}C up to 1000 h were also studied.

6.2 Materials and Methods

Four experimental Al-13%Si alloys with different Mo contents were designed in the present study with Mo content varying from 0 to 0.40 wt.%. The chemical compositions are analyzed with optical emission spectrometer and are given in Table 6.1.

In each test, approximately 3.2 Kg of materials were prepared in a clay-graphite crucible using an electric resistance furnace. The melt was maintained at around 750 ^{o}C for 30 min and then degassed for 15min before poured into a permanent mould preheated at 250 ^{o}C. The dimension of the cast ingots was 30*40*80 mm.

Table 6.1 Chemical composition of experimental alloys (wt.%)

Alloy	Si	Cu	Mg	Ni	Fe	Mn	P	Mo	Al
B0	12.72	1.06	1.05	1.09	0.41	0.35	0.001	**0**	Bal.
B1	13.27	1.07	1.01	1.11	0.40	0.3	0.001	**0.18**	Bal.
B2	13.65	1.04	1.07	1.06	0.49	0.32	0.001	**0.25**	Bal.
B3	13.13	1.06	1.01	1.11	0.50	0.32	0.001	**0.40**	Bal.

After casting, the heat treat was carried out at 520 ^{o}C with various holding time up to 24 h followed by water quenching. The effect of dispersoids was evaluated by Vickers microhardness and compression YS at room temperature (RT) as well as the compression YS and creep resistance at 300 ^{o}C. Microhardness tests were performed on the material matrix with a load of 10g and a dwell time of 20s on polished samples in order to determine the influence of dispersoids. Average value of 15 measurements was calculated for each sample. The YS at 300 ^{o}C was obtained from the compression tests with the strain rate of 10^{-3} s^{-1}. Besides, creep tests at 300 ^{o}C were performed under a constant compression load of 35MPa. For each condition, two tests were repeated to confirm the reliability of the results. All creep tests were performed after the samples were held at 300 ^{o}C for 100h to counteract the influence of the aging effect of experimental alloys.

Meanwhile, Long-term thermal exposure tests were performed at 300 °C for up to 1000 hours followed by the YS and creep resistance measurement at 300°C in order to evaluate the thermal stability of alloys during prolonged thermal exposure. Optical microscopy was used to observe the distribution of the dispersoid zone and dispersoid free zone (DFZ). To reveal the dispersoids, the samples were etched by 0.25 vol.% HF. In addition, the dark-field mode on the optical microscope was also used to better

present the dispersoids. A scanning electron microscope (SEM, JSM-6480LV) equipped with an energy dispersive X-ray spectrometer (EDS) and a transmission electron microscope (TEM, JEM-2100) operated at 200 KV was used to observe the morphology and the size of dispersoids.

6.3 Results and discussion

6.3.1 As-cast microstructure of experimental alloys

Fig. 6.1(a) shows the as-cast microstructure of the base Alloy B0, which is comprised of α-Al dendrite surrounded by fibrous eutectic silicon. Besides, dark primary Mg_2Si, gray Al-Fe-Ni, light gray Al-Cu-Ni intermetallics, can be observed in the interdendrite region. However, there are some differences with addition of Mo, especially for the alloys containing higher Mo content (Alloys B2 and B3). First of all, the primary blocky Al-Mo intermetallics (Fig. 6.1b) are observed in Mo-added alloys and its area fraction increases with Mo additions (Table 6.2), which can be attributed to the lower solubility of Mo in Al matrix [19, 27]. It is evident that the area fraction of Mo primary phases increases from 0 in the Alloy B1 to 0.17% in the Alloy B2 and to 0.78% in the Alloy B3. It should also be noted that the maximum Mo solution level in Alloys B2 and B3 was reached after the formation of Al-Mo primary phases.

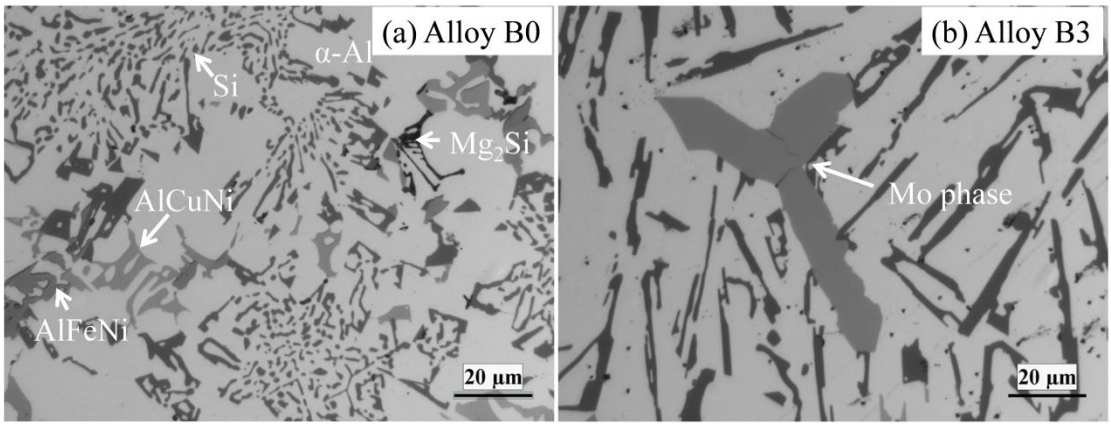

Fig. 6.1 Microstructure of experimental alloys, (a) B0 and (b) B3.

Table 6.2 Area fraction of blocky Al-Mo primary phases

Alloy	**B0**	**B1**	**B2**	**B3**
Area fraction (%)	0	0	0.17	0.78

In addition to the presence of Al-Mo primary phase, it can also be observed that the morphology of Si particles changes with the increasing addition of Mo. Fig. 6.2 shows the evolution of Si particles in experimental alloys, and corresponding aspect ratio and average length are listed in Table 6.3.

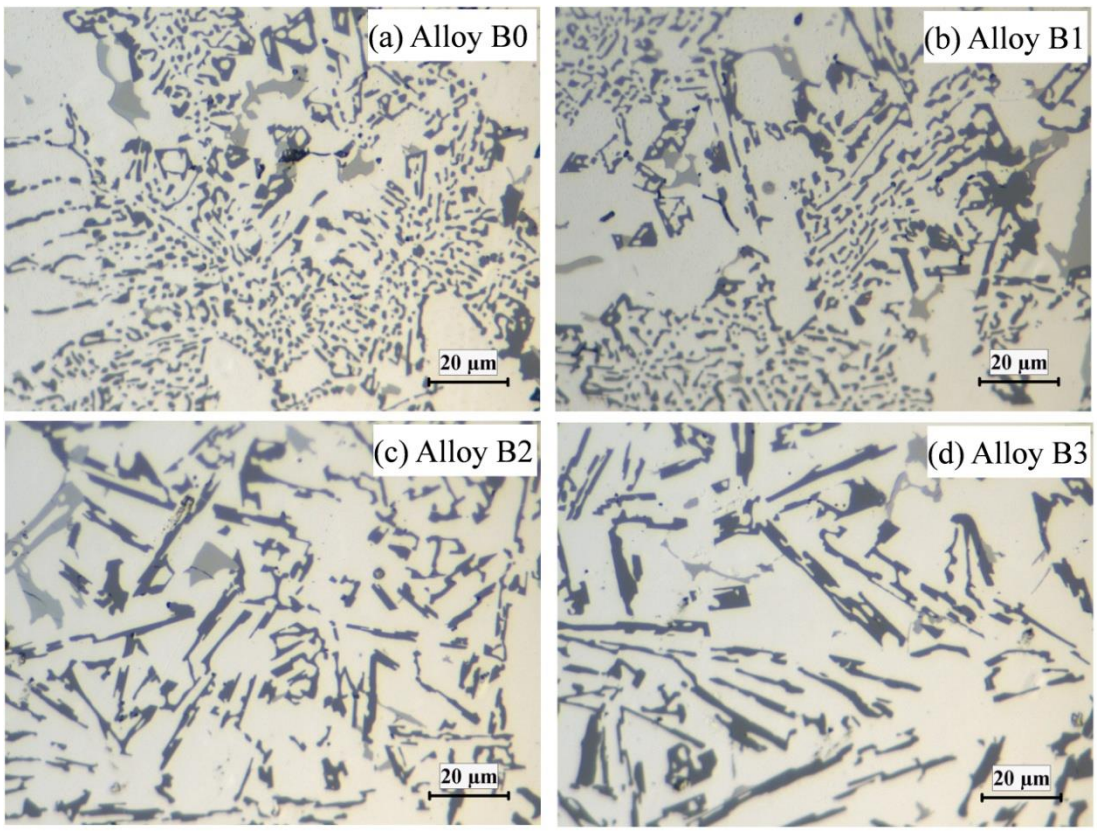

Fig. 6.2 Optical micrographs of (a) B0, (b) B1, (c) B2 and (d)B3 alloys showing the effects of Mo on Si eutectic dimensions and morphology.

The eutectic Si particles in the base Alloy B0 are mainly fine with occasional blocky plate-like Si particles (Fig. 6.2a), characterized with lower aspect ratio (2.3) and the minimum average length (3.6 μm). Alloy B1 (Fig. 6.2b) also contains clusters of fine fibrous eutectic Si. However, the plate-like coarse Si particles become more apparent. Further increasing Mo (0.25%) in Alloy B2 (Fig. 6.2c) shows little signs of fine Si particles with a greatly increased area of plate-like Si particles. For Alloy B3 with 0.4% Mo addition (Fig. 6.2d), nearly all Si particles change into plate-like morphologies. The results of measured average length and aspect ratio of Si particles also confirm that Mo addition changes the morphology of Si particles by increasing the aspect ratio and average length. As is shown, the aspect ratio of Si particles increases 3 times, and the average length increase 4.4 times from Alloy B0 to Alloy B3. So far, the phenomenon has not been reported yet by other researchers, the

possible reason for the influence introduced by Mo might related to the disruption of eutectic Si nucleus during solidification. However, the exact mechanism still needs to be further studied.

Table 6.3 Aspect ratio and average length of Si particles in experimental alloys

	Alloy B0	Alloy B1	Alloy B2	Alloy B3
Aspect ratio	2.3 ±0.5	3.4 ±0.7	6.7 ±2.3	7.0 ±2.1
Average length (μm)	3.6 ±1.0	4.4 ±1.3	15.4 ±4.6	16.0 ±4.0

6.3.2 Dispersoid evolution during heat treatment at 520 ºC

Al-13%Si piston alloys are generally heat treated at 500 ºC-560 ºC [25, 26]. Recently Liu. *et al.* [3] reported that the heat treatment at 500 ºC could largely promote the precipitation α-dispersoids. In this study, a slightly higher temperature 520 ºC is selected to perform the heat treatment to both comply with the industrial practice and possibly further enhance the dispersoids precipitation. The evolution of hardness during 520 ºC heat treatment for all four experimental alloys is plotted in Fig.6.3. Generally, the microhardness increases with time for all experimental alloys due to the precipitation of dispersoids [3]. It should be mentioned that the base alloy B0 contains a moderate amount Mn (0.35%), which enables to form dispersoids, explaining the increasing hardness with time [3]. However, the microhardness in the alloys with Mo addition is always higher than the base alloy B0 and the difference becomes increasingly larger until 12 h holding time, which can be considered a enhanced full precipitation of α-Al(Mn,Mo,Fe)Si dispersoids in the alloys with Mo additions [3].

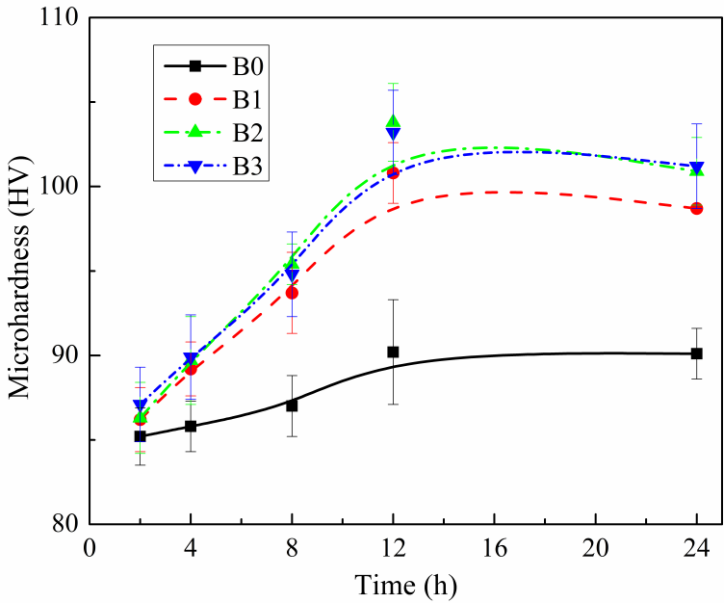

Fig.6.3 Evolution of microhardness during 520 ºC heat treatment

Since 520 ºC/12h heat treatment yields to the highest microhardness for four experimental alloys. Thus the alloys after heat treated at 520 ºC/12h etched with HF solution, and their dark-field OM micrographs are displayed in Fig. 6.4. It is evident that dispersoid zone and dispersoid free zone (DFZ) present in the aluminum matrix of Alloy B0 (Fig. 6.4a). The dispersoid zone is comprised of sparsely distributed small particles in the dendrite cells, these dispersoids are α-Al(Mn, Fe)Si dispersoids [3], leading to an increased microhardness value in Alloy B0 after 520 ºC/12 h treatment (Fig.6.3). In the Alloy B1 with 0.18% Mo addition, dispersoid zone seems to expand and DFZ are greatly confined to some limited areas. With increasing of Mo addition in Alloys B2 and B3 as showed in Fig. 6.4c and Fig. 6.4d, a large number of dispersoids are distributed in the dendrite cells with clearly defined dispersoid zone and narrow DFZ surrounding the dispersoid zone. Obviously, the precipitation of high volume and fine dispersoids at 500 ºC/12 h is highly related to the Mo content in the experimental alloys. The further improvement in microhardness (Fig.6.3) due to the Mo addition can be attributed to the enhanced precipitation of α-dispersoids characterized with increasingly expanded dispersoid zone and restricted DFZ.

Meanwhile, Alloy B2 and B3 exhibit almost identical microhardness evolution, this is likely due to the nearly identical and approximately maximum Mo solubility in the solid solution. Increasing Mo addition from 0.25 (Alloy B2) to 0.41% (Alloy B3) only leads to preferred Al-Mo primary phases (Table 6.2) instead of further increasing Mo in the solid solution of Al matrix.

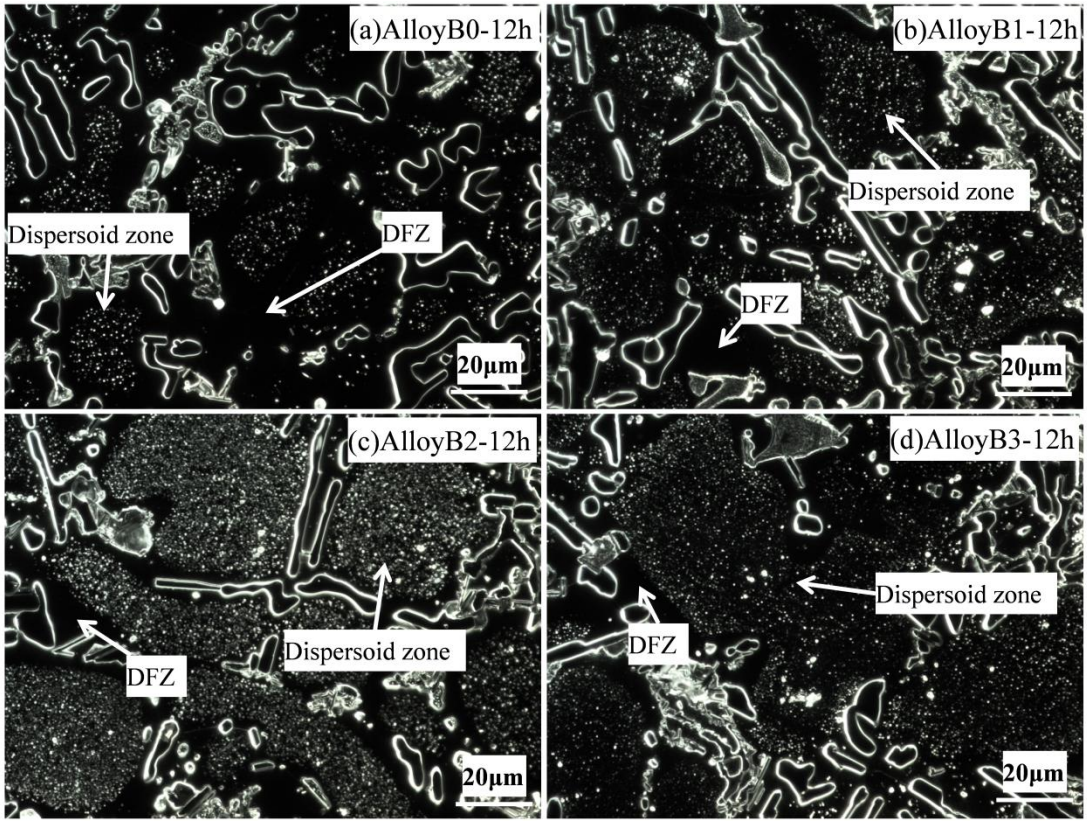

Fig. 6.4 Dark-field OM microstructures comparing the dispersoid zone and DFZ after treated at 520 ºC /12h in the alloys (a) B0, (b) B1, (c) B2 and (d) B3.

To characterize the dispersoids in details, TEM observation is performed on the dispersoid zone in alloys B0 and B2 and results are shown in Fig. 6.5. From the TEM-EDS results, the dispersoids in Alloy B0 are confirmed as α-Al(Mn,Fe)Si dispersoids while dispersoids are detected as α-Al(Mn,Mo,Fe)Si dispersoids in the alloys with Mo additions (B2). The dispersoids after heat treated at 520 ºC /12h are uniformly distributed in the matrix with the average diameter in the range of 70 nm-90nm, confirming their remarkable contribution to the microhardness in Fig.6.3. It

should also be noted that the quantity of α-dispersoids in Alloy B2 is larger than B0, whereas, the size of dispersoids in Alloy B2 is slightly smaller than B0, which both indicate that Mo addition can improve the precipitation of α-dispersoids. This is likely due to the reverse partition coefficient of Mn and Mo elements [28]. This also accounts for the expanded dispersoid zone and the increased microhardness in Alloy B2 compared with Alloy B0.

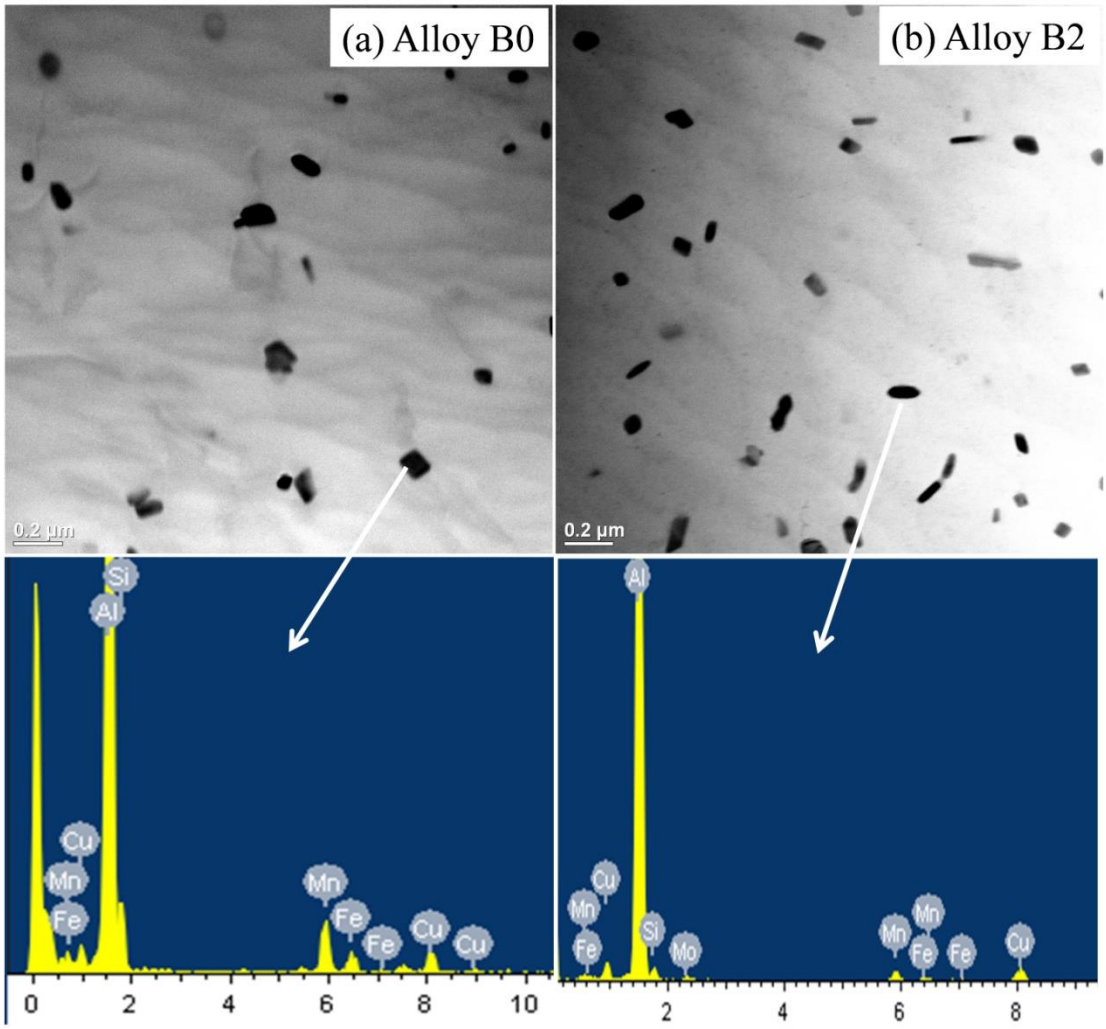

Fig. 6.5 TEM bright field images showing the distribution of dispersoids in Alloy B0 and Alloy B2 after 520 ºC/12h heat treatment

6.3.3 Yield Strength at room and elevated temperatures

Since Alloy B3 contains many Al-Mo primary phases yet exhibits nearly

identical microhardness with Alloy B2. Thus, in the present work, alloys B0 (the base) and B2 (with 0.25% Mo addition) were selected to conduct subsequent mechanical tests to investigate the effect of Mo addition. Compressive test was conducted to study the influence of dispersoids on Yield strength. Alloys were heat treated at 520 ºC/12h and aged at 200 ºC/5h (T7), then they were tested at 25 ºC and 300 ºC respectively, and the evolution of yield strength is presented in Fig. 6.6.

The YS value at RT increased from 329.3 MPa in Alloy B0 to 364.8 MPa in Alloy B2, which is 10.9% improvement for RT strength. For testing at 300 ºC, the YS value increased from 152.2 MPa in Alloy B0 to 167.9MPa in Alloy B2, which is 10.5 % enhancement and is quite like the trend at RT. The 10% enhancement of the YS at both RT and elevated temperatures represents the complementary strengthening effect of dispersoids in addition to the main strengthening Mg_2Si phase after T7 aging treatment.

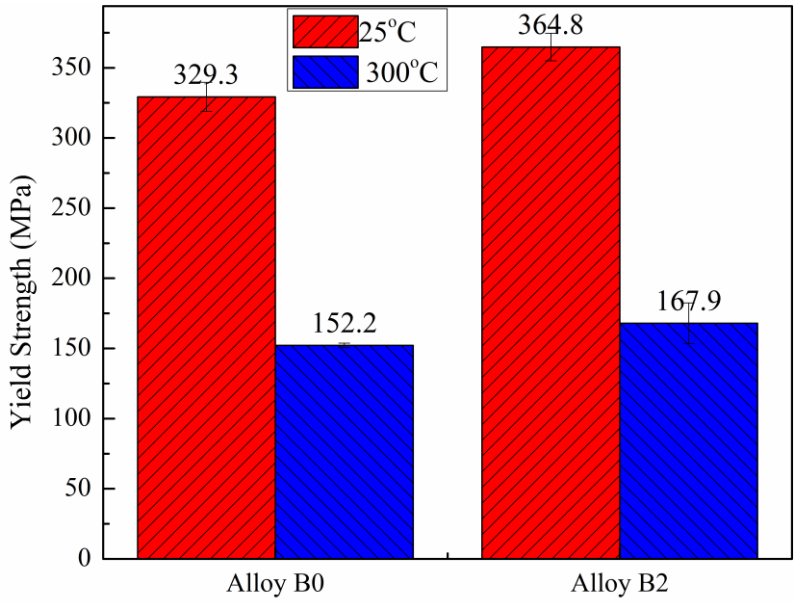

Fig. 6.6 Evolution of Yield Strength for Alloy B0 and B2 at 25 ºC and 300 ºC

6.3.4 Evolution of properties after thermal exposure at 300 ºC

The thermal stability of the mechanical properties is one of important

considerations for the alloys employed at elevated temperatures. In the present study, in order to investigate the thermal stability of elevated-temperature properties, alloys B0 and B2 after heat-treated at (520 ^{o}C/12h + 200 ^{o}C/5h), were selected and a long-term thermal exposure at 300 ^{o}C for up to 1000h was performed to evaluate the thermal stability of materials. The evolution of YS during a long-term thermal exposure for alloys B0 and B2 is shown in Fig. 6.7. The decrease of YS with holding time in both alloys B0 and B2 is evident. For example, YS of Alloy B0 dropped from 64.9 MPa to 45.4 MPa after 1000 h, indicates a 30% decrease. On the other hand, YS in Alloy B2 containing both Mo and Mn decreased from 69.5 MPa to 51.8 MPa after 1000 h and represented a 25% decrease which, indicating an improved thermal stability. For the industrial application, it would be quite interesting that the YS increment between Alloys B0 and B2 even after 1000 h holding was still around 6.4 MPa which represents a 14% improvement.

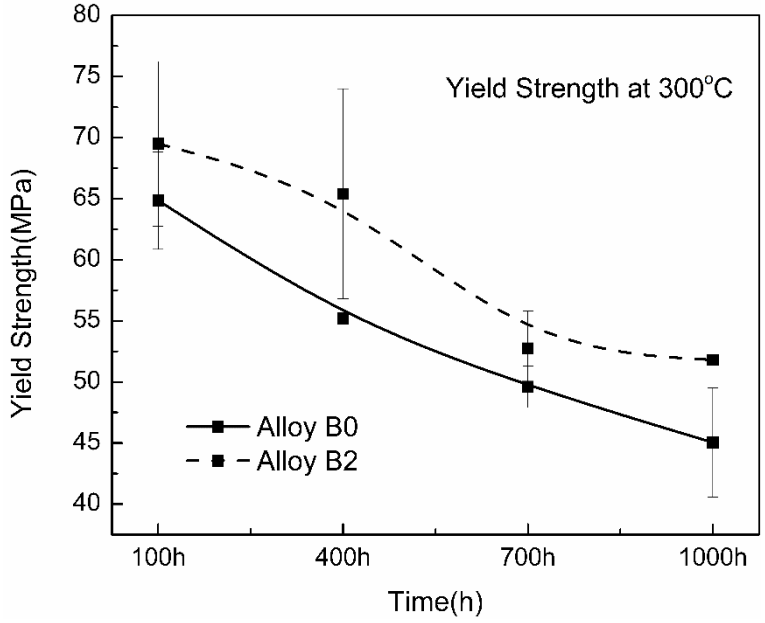

Fig. 6.7 Evolution of Yield strength for Alloy B0 and B2 during prolonged thermal exposure at 300 ^{o}C

Creep resistance is one of the most important criteria for high temperature applications. In the present work, compressive creep tests were conducted at 300 ^{o}C

under a constant load of 35 MPa to investigate the effect of Mo addition on the creep resistance of the studied alloys. Prior to the creep test, alloys were heat treated at 520 ^{o}C/12h and aged at 200 ^{o}C/5h and followed by soaking at 300 ^{o}C/100h. The corresponding creep curves are shown in Fig. 6.8.

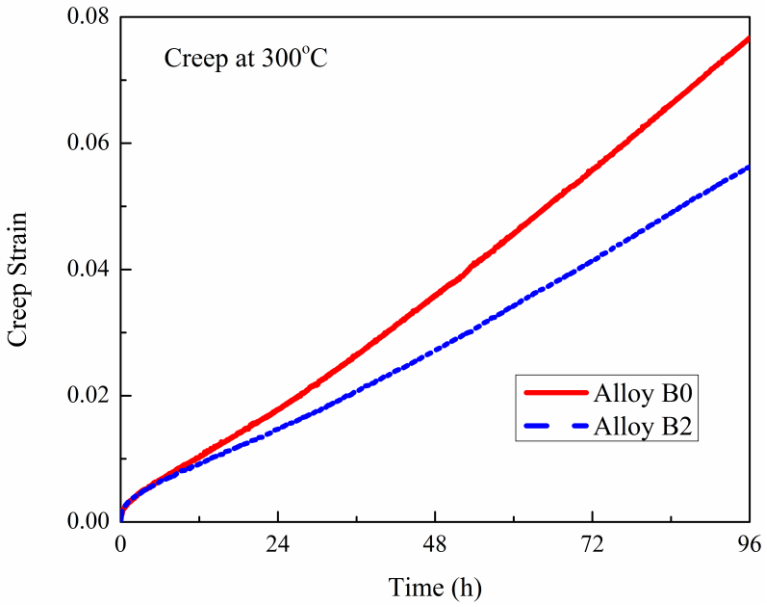

Fig. 6.8 Evolution of creep resistance for Alloys B0 and B2 tested at 300 ^{o}C under the constant load of 35 MPa

During compressive creep deformation, the creep strain of both Alloy B0 and B2 increases rapidly in the first few hours during this initial stage, then the creep deformation turns into a quasi-steady state, in which the creep rate becomes more or less constant with the progress of the creep deformation. The minimum creep rate can be calculated as the average creep rate in the quasi-steady state. The total creep strain for Alloy B0 and B2 are calculated to be 0.077 and 0.056 respectively. And the minimum creep rate for Alloy B0 and B2 is calculated to be 2.1E-7 s^{-1} and 1.5E-7 s^{-1} respectively. Generally, the smaller the total creep strain and minimum creep rate, the better the creep resistance is. Obviously, Alloy B2 displays an improved creep resistance at 300 ^{o}C. Since two alloys experienced the same heat treatment, thus the improved creep resistance in Alloy B2 is likely due to the enhanced precipitation

contribution of α-Al(Mn,Mo,Fe)Si dispersoids compared with Alloy B0 (Fig. 6.4 and Fig. 6.5). The creep strain and minimum creep rate of Alloy B0 in the present study are significantly lower than the similar alloy in the reference [3], this is most likely due to the smaller creep load (35 MPa) applied in the present work compared with 45 MPa utilised in the reference [3], which is very close to the YS of the materials.

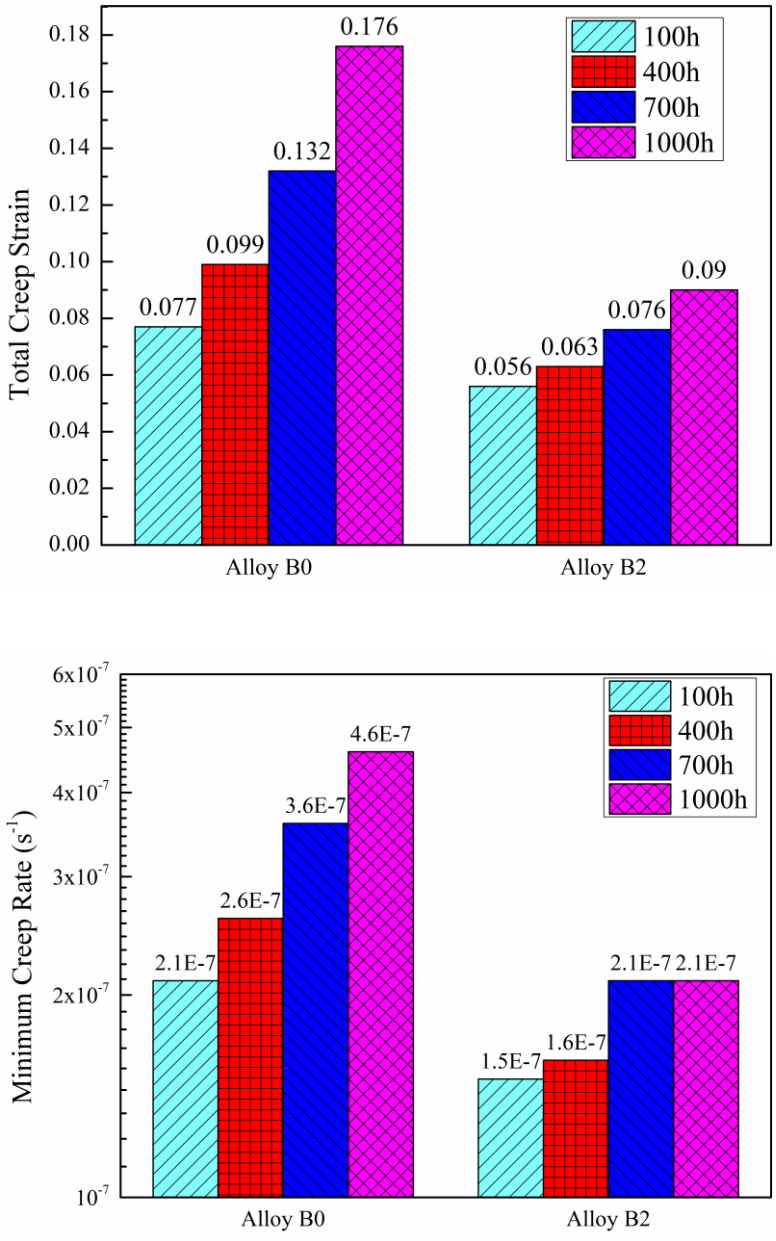

Fig. 6.9 Evolution of Creep resistance for Alloy B0 and B2 at 300 ºC.

In addition, the creep tests were also performed during the prolonged thermal

exposure at 300 ^{o}C for 400 h, 700 h and up to 1000 h and the results were summarized in Fig. 6.9. It is evident that, compared with 300 ^{o}C for 100 h, the total creep strain and minimum creep rate of both alloys increased with prolonged thermal exposure, indicating deterioration and general decrease tendency of the creep resistance. For instance, in Alloy B0, the total creep strain increased from 0.077 to 0.176 after 1000 h, while the minimum creep rate also increases from 2.1E-07 s^{-1} to 4.6E-07 s^{-1} after 1000 h, which amounts to 129% and 120% increase respectively. On the other hand, the total creep strain of Alloy B2 increased from 0.056 to 0.09 after 1000 h, while the minimum creep rate increases from 1.5E-07 s^{-1} to 2.1E-07 s^{-1} after 1000 h, showing a moderate increase of 61% and 40% respectively, indicating a great improvement of creep resistance and thermal stability of Alloy B2.

In order to find possible reasons for the decrease in mechanical properties with increasing time at elevated temperature, the microstructure of two alloys (B0 and B2) at various heat treatment conditions were studied by TEM and SEM. Fig.6.10 shows TEM images comparing the precipitates after T7 treatment and after T7 plus thermal exposure at 300 ^{o}C/1000h in Alloy B2. After T7 heat treatment, a large number of fine needle-like precipitates can be observed in the matrix, their lengths are in the range of 80-120 nm. The SADP (Fig.6.10b) indicates that these fine needle-like precipitates are β"-Mg_2Si precipitates according to the reference [29]. After 300 ^{o}C/1000h thermal exposure, the precipitates clearly coarsened (as indicated by red arrows in Fig.6.10c), their size reaches over 2 μm, the corresponded SADP (Fig.6.10d) indicates that they are equilibrium Mg_2Si phases. Consequently, the coarsening of Mg_2Si precipitates accounts for the continuous decrease of mechanical properties with holding time, which was also reported in other studies [30, 31]. It is noteworthy that α-dispersoids in Alloy B2 (indicated by blue dotted arrows) were stable even after thermal exposure of 300^{o}C/1000h. Their size remained in the range of 70 nm-90 nm, which is completely compatible with the size of α-dispersoids after 520 ^{o}C (Fig. 6.5), indicating perfect thermal stability of dispersoids at such condition. It also indicates that the Mo-containing α-dispersoids can provide complementary strengthening even

after long-term thermal exposure, resulting in an improved strength and creep resistance.

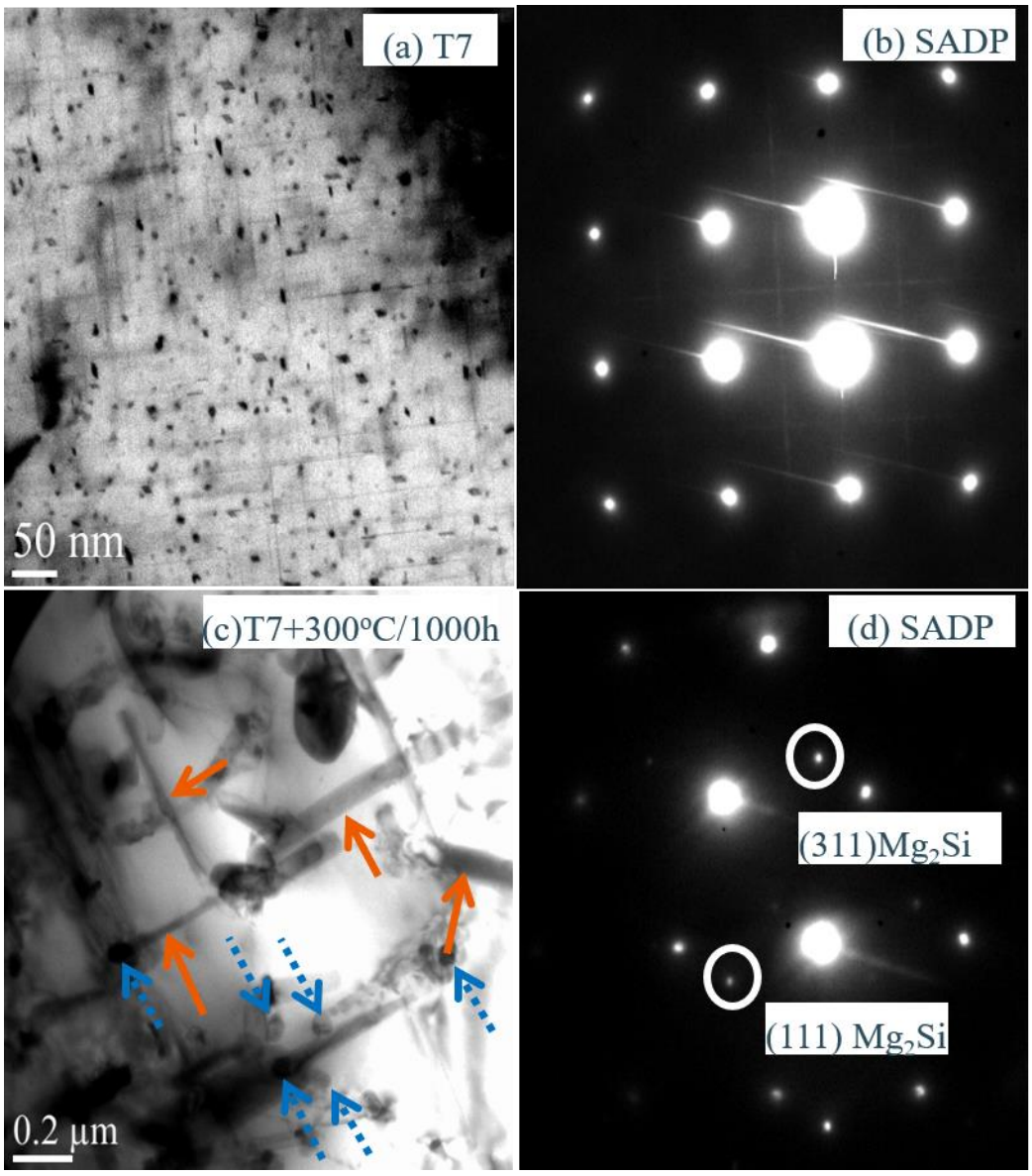

Fig.6.10 TEM bright field images showing the (a) β''-Mg_2Si precipitates and (b) their corresponding SADP; (c) α-dispersoids and precipitates after 300ºC/1000h (blue dotted arrows indicate the α-dispersoids, red arrows indicate the coarsened β precipitates) and (d) their corresponding SADP confirming equilibrium β-Mg_2Si precipitates.

In addition to coarsening of precipitates, it is also observed that the size and

morphology of eutectic Si would change with prolonged holding time. It is reported that interconnected Si particles can strengthen the Al-13%Si piston alloys by transferring extra load from the α-Al matrix to the 3D Si network [5, 20]. Fig. 6.11 shows the evolution of Si particles after various thermal treatment and the corresponding aspect ratios are listed in Table 6.4.

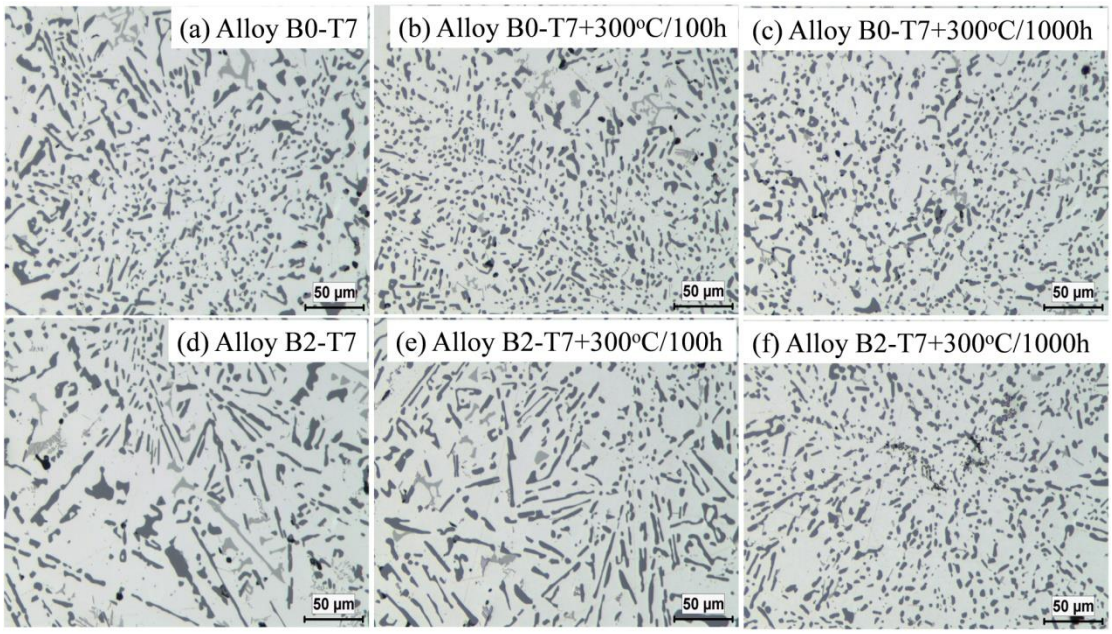

Fig. 6.11 Evolution of Si particles during thermal exposure in Alloy B0 and B2 at various heat treatment conditions.

It is apparent that the aspect ratios of Si particles in both Alloys B0 and B2 decreased after T7 treatment and further continued to decrease with holding time at 300 ºC. This indicates that the Si particles began to fragment and spheroidize during solution treatment in T7 and continued the process during thermal exposure at 300 ºC [24]. For example, the Si aspect ratio of Alloy B2 decreased from 6.7 at as-cast condition to 5.9 after T7 and further deceased to 4.8 after 300 ºC/100h, and 2.1 after 300 ºC/1000h.

Table 6.4 Evolution of aspect ratio of Si particles during thermal exposure

	T7	100h	1000h
B0	2.1±0.7	1.9±0.8	1.7±0.5
B2	5.9±2.1	4.8±1.9	2.1±0.6

Samples of Alloy B0 and B2 after various heat treatment conditions were deep-etched in 20 vol.% NaOH solution to reveal 3D morphology of eutectic Si particles and results were summarized in Fig. 6.12. One striking difference in the morphology of Si particles at as-cast condition for Alloy B0 and B2 can be observed; Si particles in Alloy B0 exhibited fine branched morphology (Fig. 6.12a), whereas they showed coarse plate-like morphology in Alloy B2 (Fig. 6.12b). After T7 treatment, a considerable portion of Si particles in Alloy B0 spheroidized and fragmented (indicated by white arrows in Fig. 6.12c). Whereas Si particles in Alloy B2 seems to retain its plate-like morphology with few partial neckings at certain spots (indicated by white arrows in Fig. 6.12d) without causing apparent fragmentation. After subsequent thermal exposure of 300^{o}C/1000h, both Alloy B0 and B2 underwent the process of fragmentation and spheroidization. The morphology of Si particles in Alloy B0 was mostly round shape. However, a reasonable part of Si particles in the Mo-containing Alloy B2 retained the plate-like morphology. Mo addition appears to decelerate the fragmentation and spheroidization process of Si particles, hence retarding the deterioration of Si networks in Al-13%Si alloys, which might partially contribute to the enhanced YS and creep resistance during thermal exposure.

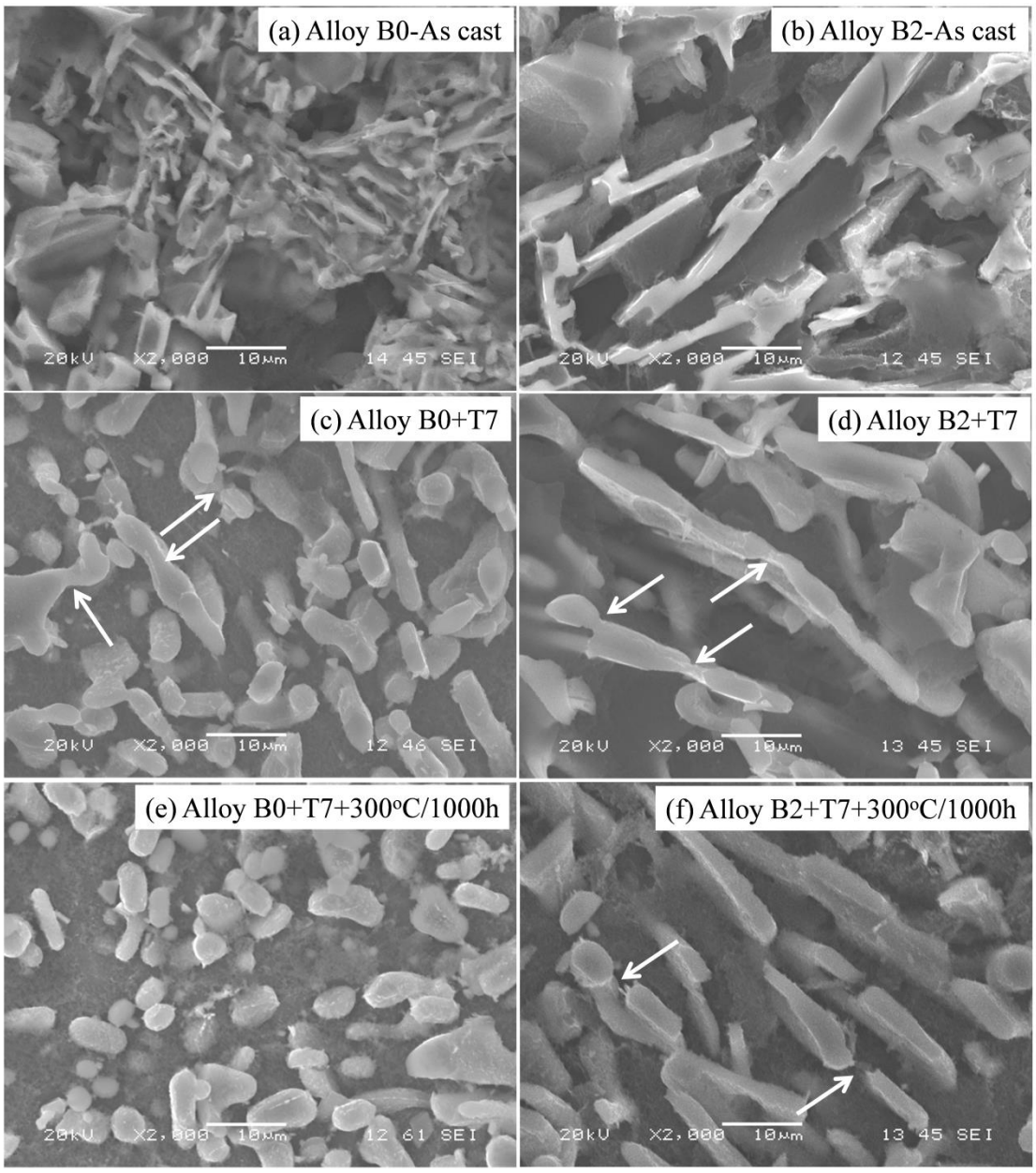

Fig. 6.12 SEM micrographs showing the morphology change of Si particles in deep etching alloys under different conditions

Traditionally heat treatable Al-13%Si piston alloys are subjected to the solution treatment at 500-520 ^{o}C followed by an T7 artificial ageing to improve the RT mechanical properties, owing to strengthening of large quantity of nanoscale Mg_2Si precipitates [3]. However, the coarsening of precipitates and deterioration of eutectic Si network at elevated temperature restricts their strengthening effects [6]. In the present work, Mo addition introduces two beneficial influences on Al-13%Si piston

alloys. First, Mo addition promotes the precipitation of thermally stable α-dispersoids during precipitation temperature (520 ^{o}C), which is compatible with the conventional solution treatment for Al-13%Si piston alloys. These α-Al(Mn,Mo,Fe)Si dispersoids partially compensate the detrimental effect imposed by coarsening of Mg_2Si precipitates during prolonged thermal exposure. Second, Mo addition changes the morphology of Si particles and retards the fragmentation and spheroidization of the Si particles. In brief, complementary strengthening of thermally stable dispersoids in Al matrix and retarding Si particle spheroidization due to Mo addition can provide synergistic strengthening effect in Al-13%Si piston alloys for elevated-temperature applications.

6.4 Conclusions

In this study, the effects of Mo on the microstructure (α-dispersoid and eutectic Si), mechanical properties and creep resistance in Al-13%Si piston alloys have been studied and following conclusions can be drawn:

1. The addition of Mo in Al-13% piston alloys improved the microhardness and yield strength due to the enhanced precipitation of α-dispersoids.

2. The coarsening of Mg_2Si precipitates and the fragmentation and spheroidization of Si particles account for the decrease of yield strength and creep resistance at elevate temperature with prolonged time. The presence of thermally stable of α-dispersoids in the aluminum matrix due to the combination addition of Mo and Mn can provide the complementary strengthening effect in addition to the main strengthening Mg_2Si and Si phases.

3. The addition of Mo can change the morphology of eutectic Si particles and retard Si fragmentation and spheroidization during solution treatment and prolonged thermal exposure.

4. The improved elevated-temperature strength and creep resistance due to Mo addition during prolonged thermal exposure at 300 ^{o}C can be ascribed to the synergistic effect of enhanced precipitation of α-dispersoids and retardation of the fragmentation and spheroidization of Si particles.

References

[1] M. Zeren, The effect of heat-treatment on aluminum-based piston alloys, Materials & Design 28(9) (2007) 2511-2517.

[2] Y. Wang, H. Liao, Y. Wu, J. Yang, Effect of Si content on microstructure and mechanical properties of Al–Si–Mg alloys, Materials & Design 53 (2014) 634-638.

[3] K. Liu, X.G. Chen, Improvement in elevated-temperature properties of Al-13% Si piston alloys by dispersoid strengthening via Mn addition, Journal of Materials Research 33(20) (2018) 3430-3438.

[4] Z. Qian, X.F. Liu, D.G. Zhao, G.H. Zhang, Effects of trace Mn addition on the elevated temperature tensile strength and microstructure of a low-iron Al-Si piston alloy, Materials Letters 62(14) (2008) 2146-2149.

[5] Z. Asghar, G. Requena, E. Boller, Three-dimensional rigid multiphase networks providing high-temperature strength to cast AlSi10Cu5Ni1-2 piston alloys, Acta Materialia 59(16) (2011) 6420-6432.

[6] Z. Asghar, G. Requena, F. Kubel, The role of Ni and Fe aluminides on the elevated temperature strength of an AlSi12 alloy, Materials Science and Engineering: A 527(21) (2010) 5691-5698.

[7] V. Abouei, H. Saghafian, S.G. Shabestari, M. Zarghami, Effect of Fe-rich intermetallics on the wear behavior of eutectic Al-Si piston alloy (LM13), Materials & Design 31(7) (2010) 3518-3524.

[8] J. Feng, B. Ye, L. Zuo, R. Qi, Q. Wang, H. Jiang, R. Huang, W. Ding, Effects of Ni content on low cycle fatigue and mechanical properties of Al-12Si-0.9Cu-0.8Mg-xNi at 350°C, Materials Science and Engineering: A 706 (2017) 27-37.

[9] Y. Yang, K.L. Yu, Y.G. Li, D.G. Zhao, X.F. Liu, Evolution of nickel-rich phases in Al-Si-Cu-Ni-Mg piston alloys with different Cu additions, Materials & Design 33 (2012) 220-225.

[10] Z. Asghar, G. Requena, G.H. Zahid, D. Rafi ud, Effect of thermally stable Cu- and Mg-rich aluminides on the high temperature strength of an AlSi12CuMgNi alloy,

Materials Characterization 88 (2014) 80-85.

[11] G. Requena, G. Garcés, M. Rodríguez, T. Pirling, P. Cloetens, 3D architecture and load partition in eutectic Al-Si alloys, Advanced Engineering Materials 11(12) (2009) 1007-1014.

[12] S.G. Shabestari, R. Gholizadeh, Assessment of intermetallic compound formation during solidification of Al-Si piston alloys through thermal analysis technique, Materials Science and Technology 28(2) (2012) 156-164.

[13] R. Fernandez-Gutierrez, G.C. Requena, The effect of spheroidisation heat treatment on the creep resistance of a cast AlSi12CuMgNi piston alloy, Materials Science and Engineering: A598 (2014) 147-153.

[14] V. Páramo, R. Colás, E. Velasco, S. Valtierra, Spheroidization of the Al-Si eutectic in a cast aluminum alloy, Journal of Materials Engineering and Performance 9(6) (2000) 616-622.

[15] R. Sharma, A. Kumar, D.K. Dwivedi, Influence of Solution Temperature on Microstructure and Mechanical Properties of Two Cast Al–Si Alloys, Materials and Manufacturing Processes 21(3) (2006) 309-314.

[16] Z. Jiaqing, L. Ya, P. Haoping, W. Jianhua, S. Xuping, Spheroidization of Si in Al–12.6wt.%Si at eutectic temperature and its tensile properties, Materials Research Express 4(10) (2017) 106505.

[17] J. Wang, J. Zhu, Y. Liu, H. Peng, X. Su, Effect of spheroidization of eutectic Si on mechanical properties of eutectic Al–Si alloys, Journal of Materials Research 33(12) (2018) 1773-1781.

[18] E. Arzt, E. Gohring, A model for dispersion strengthening of ordered intermetallics at high temperatures, Acta Materialia 46(18) (1998) 6575-6584.

[19] H. Liao, Y. Tang, X. Suo, G. Li, Y. Hu, U.S. Dixit, P. Petrov, Dispersoid particles precipitated during the solutionizing course of Al-12wt.%Si-4wt.%Cu-1.2wt.%Mn alloy and their influence on high temperature strength, Materials Science and Engineering: A 699 (2017) 201-209.

[20] G. Han, W.Z. Zhang, G.H. Zhang, Z.J. Peng, Y.J. Wang, High-temperature

mechanical properties and fracture mechanisms of Al-Si piston alloy reinforced with in situ TiB2 particles, Materials Science and Engineering: A 633 (2015) 161-168.

[21] A.R. Farkoosh, X.G. Chen, M. Pekguleryuz, Dispersoid strengthening of a high temperature Al-Si-Cu-Mg alloy via Mo addition, Materials Science and Engineering: A 620 (2015) 181-189.

[22] M. Tocci, R. Donnini, G. Angella, A. Pola, Effect of Cr and Mn addition and heat treatment on AlSi3Mg casting alloy, Materials Characterization 123 (2017) 75-82.

[23] R. Chen, Q. Xu, Z. Jia, B. Liu, Precipitation behavior and hardening effects of Si-containing dispersoids in Al–7Si–Mg alloy during solution treatment, Materials & Design 90 (2016) 1059-1068.

[24] A.R. Farkoosh, X. Grant Chen, M. Pekguleryuz, Dispersoid strengthening of a high temperature Al–Si–Cu–Mg alloy via Mo addition, Materials Science and Engineering: A 620 (2015) 181-189.

[25] K. Liu, H. Ma, X.G. Chen, Enhanced elevated-temperature properties via Mo addition in Al-Mn-Mg 3004 alloy, Journal of Alloys and Compounds 694 (2017) 354-365.

[26] A.R. Farkoosh, X. Grant Chen, M. Pekguleryuz, Interaction between molybdenum and manganese to form effective dispersoids in an Al–Si–Cu–Mg alloy and their influence on creep resistance, Materials Science and Engineering: A 627 (2015) 127-138.

[27] W. Yang, M. Wang, R. Zhang, Q. Zhang, X. Sheng, The diffraction patterns from β″ precipitates in 12 orientations in Al–Mg–Si alloy, Scripta Materialia 62(9) (2010) 705-708.

[28] F. Stadler, H. Antrekowitsch, W. Fragner, H. Kaufmann, P.J. Uggowitzer, Effect of main alloying elements on strength of Al–Si foundry alloys at elevated temperatures, International Journal of Cast Metals Research 25(4) (2012) 215-224.

[29] L. Tian, Y. Guo, J. Li, J. Wang, H. Duan, F. Xia, M. Liang, Elevated re-aging of a piston aluminium alloy and effect on the microstructure and mechanical properties, Materials Science and Engineering: A 738 (2018) 375-379.

Chapter 7 Conclusions and Recommendations

7.1 Conclusions

In the present work, the effect of Mo and Mn elements on the microstructure and mechanical properties of Al-Si alloys at both ambient and elevated temperatures were systematically investigated. In addition, the precipitation behavior of α-Al(Mn,Mo,Fe)Si dispersoids and their effects on elevated-temperature strength and creep resistance was also studied. From the experimental results obtained, the following conclusions can be drawn, which categorized in three parts corresponding to the different aspects that were studied.

Part I: Evolution of Fe-rich intermetallics in Al-Si-Cu 319 cast alloy with various Fe, Mo, and Mn contents

1. Two types of platelet Fe-rich intermetallics, defined as eutectic and pre-eutectic β-Fe, and one type of α-Fe can precipitate depending on the Fe, Mo, and Mn contents. Without the Mn/Mo additions, only eutectic β-Fe form in the low-Fe alloys (0.3%), whereas pre-eutectic and eutectic β-Fe coexist in the high-Fe alloys (0.7%).

2. The addition of Mo can strongly promote the formation of α-Fe and suppress the precipitation of β-Fe in both low-Fe and high-Fe alloy. However, the effect of Mo on the suppression of β-Fe is greatly related to the Fe contents. In low-Fe alloys, the addition of 0.37% Mo can completely suppress eutectic β-Fe. While, only pre-eutectic β-Fe can be reduced with increasing Mo content, leaving the eutectic β-Fe intermetallics almost unchanged in high-Fe alloys.

3. Both pre-eutectic β-Fe and eutectic β-Fe can be completely suppressed, and a unique α-Fe microstructure can be achieved with a combined addition of Mn (0.24%) and Mo (0.41%) in high-Fe alloys.

4. Compared with Mn, Mo exhibits a stronger effect in promoting α-Fe precipitation. The combined addition of Mn and Mo can achieve a better modification of both pre-eutectic β-Fe and eutectic β-Fe intermetallics in industrial 319 cast alloys.

Part II: Evolution of dispersoids and their effect on elevated-temperature mechanical properties and creep resistance in Al-Si-Cu 319 cast alloys with Mo and Mn additions

5. The dispersoids commence to form at 450^{o}C during heat treatment and the optimum condition for dispersoids with higher volume fraction and finer size can be reached after 500 ^{o}C/8h treatment.

6. Both Mn and Mo can promote the precipitation of dispersoids. However, individual addition of Mo has stronger positive effect than individual Mn addition but weaker than the combined addition of Mn and Mo.

7. Complementary improvement on the yield strength at room temperature (~ 10%) while remarkable increase on that at 300 ^{o}C (~ 20%) can be obtained due to the fully precipitation of dispersoids.

8. The creep resistance is greatly improved with additions of Mn or/and Mo. Compared with alloys free of Mn and Mo, the minimum creep rate decreases from 5.5E-07 s^{-1} to 1.1E-08 s^{-1} while the threshold stress increases from 10.6 to 22.8 MPa in alloy with combined additions of Mn and Mo due to the formation of dispersoids.

9. YS and creep resistance in all experimental alloys decrease during thermal exposure at 300 ^{o}C due to the continuous coarsening of Cu precipitates. However, much lower decreasing extend is observed due to the addition of Mn or/and Mo. During thermal exposure at 300 ^{o}C up to 1000 hours, 10% decrease on yield strength and 5% increase on the maximum creep strain is reached in alloys with combined additions of Mn and Mo compared with 30% decrease and 47% increase in alloy free of Mn or Mo, respectively, showing the superior thermal

stability of Al–Si–Cu 319 alloys with Mn and Mo additions and then widening their application at elevated temperature.

Part III: Improved elevated-temperature properties in Al-13%Si piston alloys by Mo addition

10. The addition of Mo in Al-13% piston alloys improved the microhardness and yield strength due to the enhanced precipitation of α-dispersoids.

11. The coarsening of Mg_2Si precipitates and the fragmentation and spheroidization of Si particles account for the decrease of yield strength and creep resistance at elevate temperature with prolonged time. The presence of thermally stable of α-dispersoids in the aluminum matrix due to the combination addition of Mo and Mn can provide the complementary strengthening effect in addition to the main strengthening Mg_2Si and Si phases.

12. The addition of Mo can change the morphology of eutectic Si particles and retard Si fragmentation and spheroidization during solution treatment and prolonged thermal exposure.

13. The improved elevated-temperature strength and creep resistance due to Mo addition during prolonged thermal exposure at 300 ^{o}C can be ascribed to the synergistic effect of enhanced precipitation of α-dispersoids and retardation of the fragmentation and spheroidization of Si particles.

7.2 Recommendations

In the present study, the effect of Mo and Mn elements on the microstructure and mechanical properties of Al-Si alloys at both room temperature and elevated temperatures were systematically investigated and some significant progress have been obtained. However, some questions still need to be further investigated. The following points are recommended for the future work:

1. Only one-step heat treatment was applied to precipitate dispersoids in the present work. However, it is advisable to investigate two-step or even multi-step thermal treatment to maximize the number density and volume fraction of α-dispersoids.

2. Fe was confirmed to be a crucial element for α-Al(Mn,Mo,Fe)Si dispersoids in the present work, hence, its effect on α-dispersoids formation, DFZ and number density should also be investigated. Besides, the Fe contents in Al–Si alloys should be optimized without precipitating needle-like β-Al_5FeSi.

3. In the present work, α-dispersoids were investigated to precipitate at temperatures (over 450^{o}C). However, the precipitation temperature is significantly higher than that in Al-Mn-Mg (3xxx) alloys. Thus, the mechanisms for nucleation of α-dispersoids need to be further investigated.

4. The deterioration of mechanical properties after long time thermal exposure was confirmed partially due to the coarsening of Cu and Mg precipitates in the present work. Thus, novel approaches to minimize the coarsening of Cu and Mg precipitations would have a significant impact on alloys for elevate-temperature applications.